THE CYCLIC MECHANICAL AND FATIGUE PROPERTIES OF FERROANELASTIC BETA PRIME GOLD CADMIUM

BY

ROBERT STEPHEN KARZ

B.S., Massachusetts Institute of Technology, 1967
M.S., University of Illinois, 1968

THESIS

Submitted in partial fulfillment of the requirements
for the degree of Doctor of Philosophy in Metallurgical Engineering
in the Graduate College of the
University of Illinois at Urbana-Champaign, 1972

Urbana, Illinois

THE CYCLIC MECHANICAL AND FATIGUE PROPERTIES OF FERROANELASTIC BETA PRIME GOLD CADMIUM

Robert Stephen Karz, Ph.D.
Department of Metallurgy and Mining Engineering
University of Illinois at Urbana-Champaign, 1972

Beta prime $Au_{1.05}Cd_{0.95}$ deforms up to strains of 0.076 at low stress levels by the reversible motion of twin boundaries (either present in lamellar twins introduced by a martensitic transformation or nucleated in response to stress) as opposed to deformation by slip in most other metals. In addition, this alloy exhibits the remarkable "rubber-like" behavior due to a volume restoring force which returns twin boundaries displaced by stress to their original positions when stress is removed. The fatigue behavior of this alloy was investigated and found to be exceptional for certain orientations with lives of 10^5 to 10^6 cycles at total strain amplitudes ($\Delta\varepsilon$) above 0.05 not uncommon. Fatigue lives were influenced principally by the stress level which controlled the amount of plastic deformation, and stress fatigue resistance was low compared with most metals. Failure always exhibited brittle characteristics. An algorithm was devised to predict mechanical behavior from the twin system orientations and was found in good agreement with experiment for longitudinal strains above 0.04. The cyclic mechanical properties were examined, and a model for the behavior was proposed utilizing previous theories of the restoring force and the Peierls-Nabarro stress for twinning and new concepts. Gold-cadmium was found to have certain strain fatigue resistant applications, particularly in electronics where the alloy's high electrical conductivity is utilized, and the understanding of the deformation gained by studying the cyclic mechanical properties indicates promise for similar studies in other "memory" systems.

Page intentionally left blank

ACKNOWLEDGMENTS

The author gratefully acknowledges the continuous guidance and stimulating discussions of Professor David S. Lieberman throughout his graduate study. The author also wishes to acknowledge the helpful suggestions and advice of Professor Frederick V. Lawrence, Jr., during his research.

Thanks are owed to Dr. Daniel R. Hennessy for assistance in operating the MTS equipment and to his colleagues, Dr. Bijoy K. Das and Dr. Michael A. Schmerling, for their aid and useful conversations through the duration of the author's graduate education.

The author wishes to thank his wife, Myrna, for her patience and understanding and for her help in preparing the manuscript. He is grateful to his parents for their encouragement throughout his education.

The author is thankful for the use of the Materials Research Laboratory facilities. This research was supported by the Department of Metallurgy and Mining Engineering, the College of Engineering Experiment Station, the United States Atomic Energy Commission Contract AT 11-1 (1198), the United States Air Force Office of Scientific Research Contract AF 68-1599, and the National Aeronautics and Space Administration Contract NGR-005-14-162.

TABLE OF CONTENTS

I. INTRODUCTION

The alloy 47.5 atomic percent cadmium in gold is but one of a growing list of alloys including TiNi,[1] CuAlNi,[2] InTl,[3,4] CuZn,[5] and CuZnSn[6,7] exhibiting a reversible first order martensitic phase change on cooling and the extraordinary shape memory:[1] If specimens of these alloys are deformed in the martensitic phase, they will return to the original configuration possessed by the high temperature phase when heated up through the transformation temperature. A prevalent mode of deformation in these martensitic alloys is by the reversible motion of transformation twin boundaries. The term "ferroanelastic" was chosen to describe the behavior to emphasize the close analogy between it and ferromagnetism where stress, twin boundaries and a particular direction in the crystal are analogous to the magnetic field, domain boundaries and the direction of magnetization.[8] The last part of the term is associated with the stress-strain hysteresis discussed later. At least two of these, AuCd and InTl, in addition exhibit the even more remarkable and unusual "ferroelastic"[9] or rubber-like behavior in which specimens may be deformed to strains greater than 0.05 in the martensite phase by the motion of the transformation twin boundaries but will return to their original shapes on the removal of stress. This "ferroelastic" behavior is now believed to be caused by volume forces associated with shuffled atom positions[8] which cause the boundaries to return to their original positions to reduce the free energy when stress is removed.

Since deformation in AuCd is by twin boundary motion and not by the conventional slip dislocations responsible for plastic deformation in normal metals, it was anticipated that cyclic deformation could be continued

for long periods without accumulation of the same structural damage usually associated with fatigue, and this was indeed found to be the case. Although specimens of this material have been bent and stressed many times to illustrate "ferroelastic" behavior, no quantitative study has been made heretofore to determine the fatigue behavior under repeated cyclic stresses. The purpose of this dissertation was to study fatigue in $Au_{1.05}Cd_{0.95}$ martensite, and, in particular, to investigate the role of twin boundary motion in the mechanical and fatigue properties. The results are believed generally applicable to InTl and any other system deforming by twin boundary motion.

Gold-cadmium has been studied in considerable detail[9] and is now perhaps the best understood of the "memory" alloys. This is partially due to the relative ease of obtaining high quality single crystals which greatly simplifies the study of mechanical properties. It is an ordered alloy with CsCl β structure which transforms martensitically and reversibly at ~57°C on cooling to the twinned orthorhombic β' phase; the reverse transformation occurs at ~74°C. The crystal geometry of the transformation was treated by Lieberman, Wechsler and Read;[10,11] the W-L-R theory of such transformations was first developed and applied to this system. The transformation proceeds by the motion of interface(s) separating the high temperature parent from the low temperature product phase.

When a single crystal parent transforms by a <u>single planar interface</u>, the product is called a single region specimen and consists of one set of alternating twin lamellae (Figure 1). Such specimens deform to high strains (up to 0.076) at low stresses (~4 Kg/mm^2) ferroelastically, or by the nucleation and growth of mechanical twin spikes twin related to the transformation twins at higher stresses (~14 Kg/mm^2), or plastically to

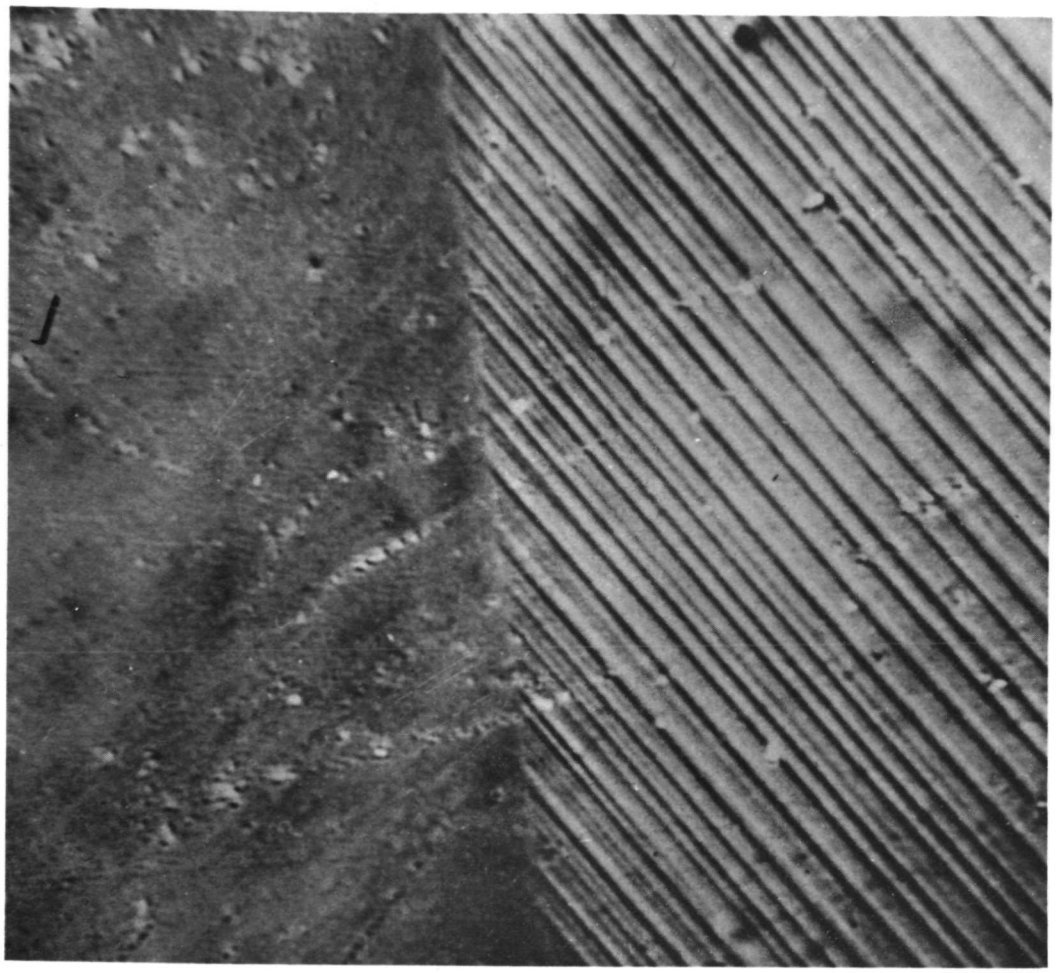

Figure 1. The β→β' transition in AuCd in a partially transformed specimen. A single planar interface separating the single crystal high temperature β phase (left) from the lamellar twinned orthorhombic β' product phase moves from left to right during cooling. From Reference 10. (~300x)

small strains (~0.01) at still higher stresses. Which deformation mode will be operative under an arbitrary stress system can be predicted as a function of orientation as will be shown; the maximum allowable strain can also be calculated for the first two deformation modes. More commonly, a single crystal parent transforms by multiple interfaces resulting in many regions of lamellar twinned structure (Figure 2). Because they originated from the same single crystal parent, the twinned regions in such specimens are crystallographically related across their boundaries. Birnbaum and Read[12] reported that the regional boundaries, as well as the twin boundaries, move in response to low stresses. Occasionally a single crystal cubic specimen will transform by crossed interfaces to a single crystal orthorhombic product;[13] apparently the second interface de-twins the twinned product resulting from the passage of the first interface (see above). Whether twin lamellae which appear to grow in such specimens when they are stressed originate in twin nuclei present prior to loading or are introduced as mechanical twins is uncertain.

Part of the impetus for this research resulted from the improvement of a wire casting process originally employed in the preparation of x-ray specimens.[14] Using this technique (described in Appendix A), wires 0.05 mm in diameter and over 40 cm long were cast. If wires of this alloy exhibit the strain fatigue resistance strongly suggested by the deformation mechanism and past qualitative observations on rod shaped specimens, they would have potential applications in high strain fatigue situations, in particular those that also exploit the alloy's high electrical conductivity (1.2 x 10^5mho-cm) such as relay armature connections and pacemaker electrodes. Therefore, the fatigue properties of this alloy are of considerable theoretical and practical interest.

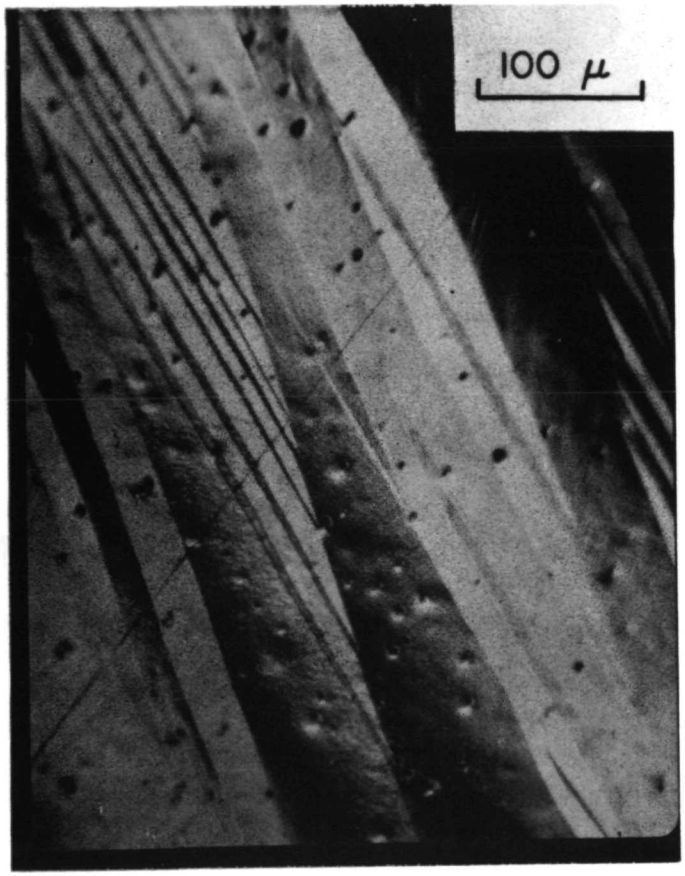

Figure 2. The surface of Specimen 60 after a multiple interface transformation showing several regions of lamellar twinned material. The region boundaries, like the twin boundaries, can move in response to stress.[12] Note that some non-adjacent regions exhibit parallel twin markings implying that they have the same orientation.

However, such wires are unsuitable for fatigue tests because of their shape and grain boundaries since a common feature of all the deformation modes described above (except plasticity) is that they can only be studied in detail on specimens transformed from single crystals of the parent β phase because grain boundaries prevent twin boundary and region boundary movement. This complicates fabrication since conventional procedures like machining must be replaced by less damaging ones such as casting and electropolishing in the production of single crystal test specimens. In addition, a propensity towards buckling due to the low effective modulus (as low as ~5Kg/mm^2) for twin boundary motion observed here and reported earlier[15] dictates an "hourglass" specimen shape which in turn complicates longitudinal strain determination.

II. EXPERIMENTAL PROCEDURES AND CRYSTALLOGRAPHIC ANALYSIS

A. Specimen Preparation

All specimens were prepared from 99.999 percent pure cadmium obtained from American Smelting and Refining Company (cleaned in dilute nitric acid), and 99.999 percent pure gold obtained from the Sigmund Cohen Company (cleaned in aqua regia). These materials were weighed out to a composition 47.50 ± 0.01 atomic percent cadmium, sealed in 5 mm quartz tubing (cleaned in glass cleaning solution and methanol) in an atmosphere of 10^{-3} Torr argon, and homogenized at ~700°C. The resulting ingots were weighed and resealed in capsules whose lower sections were constricted in the "hourglass" shape* and pointed to facilitate single crystal growth in an atmosphere of either 100 Torr or 10^{-3} Torr argon (at room temperature pressure) for reasons discussed below. The ingots were cast into the "hourglass" sections at ~700°C, and small bubbles were removed by tapping on a rod used to support the capsule in the vertical tubular furnace. High quality single crystals (with sharp Laue spots) were obtained by a modified Bridgman technique[15] at a growth rate of 10 inches per hour. Polycrystals with ~1 mm grain size were obtained by a water quench. After growth, the specimens were reweighed to determine weight loss.

The two argon pressures reported above correspond to two techniques used to control bubble formation which is presumed to be due mainly

---

* A small number of tensile specimen capsules were prepared with a 1-1/4 inch gage length 0.079 inches in diameter.

to cadmium vapor.** The first technique employed relatively high argon pressure (~300 Torr at 700°C) to suppress cadmium bubble formation and was employed early in the research. The second used low argon pressure and allowed the cadmium vapor to equilibrate before final bubble removal by leaving the molten ingot in the furnace hot zone approximately 1-1/2 hours. This technique was very effective. Even with the high Cd vapor pressure, the small free volume (~1 cm^3) limited the calculated cadmium loss to ~10^{-3} grams which was the same order of magnitude as the total weight loss observed. The weight loss after homogenization and growth and the resulting composition, conservatively assuming it all to be due to cadmium vapor, are listed for each specimen in Appendix B, the worst case being a final composition of 47.45 percent Cd.

Certain batches of quartz tubing had a pronounced tendency to adhere to the ingot on solidification causing capsule fracture and ingot oxidation. This was prevented by depositing a thin carbon film inside the capsule. The procedure involved rinsing the capsule in acetone and immediately heating it over a low flame, thus burning the residual acetone onto the capsule wall. Loose carbon was removed by a methanol rinse.

Torsion specimens were tested as cast while tension-compression specimens were first electropolished to reduce the specimen diameters approximately 0.035 inches to facilitate gripping. This was also observed to improve crystal quality through removal of the surface layers and thus to aid in achieving the single interface transformations discussed earlier.

** At 700°C the partial pressure of cadmium is 400 Torr while that for gold is negligible (<< 1 Torr).[16]

The electropolishing solution consisted of 100 gm KCN, 100 gm sucrose, 60 gm K_2CO_3 and 375 cc H_2O[12] heated to approximately 95°C so that the specimens were electropolished in the high temperature β phase. A 1200 ml stainless steel beaker used to contain the solution served as the cathode. The tips of the specimens were notched to allow gripping by an alligator clip, and all but the tips were immersed in the solution. It was found that a 12 volt automobile battery power source gave a good polish with no voltage or current controls. The average time required per specimen was approximately three minutes; a solution could only be used for two specimens since longer use caused pitting. After use, the solution was rendered harmless by adding ferrous sulfate to form an insoluble ferrous cyanide complex. Figure 3 shows the dimensions of typical torsion and tension-compression specimens.

Most of the specimens tested were transformed by a single interface as discussed earlier by heating to the high temperature β phase in an electrical heating device and cooling through the transformation temperature range in a temperature gradient. The transformation on cooling was observed by optical microscopy, and if more than one interface was observed, the procedure was repeated until a single interface transformation was achieved. Specimens were subsequently oriented by Laue technique (Section II, B), and these data were used to predict mechanical behavior (Section III). Specimens with undesirable predicted behavior were recycled through the transformation until a different (crystallographically equivalent) interface was observed and the specimens were oriented again. Some specimens were deliberately transformed by several interfaces, thus creating the multiple region specimens described earlier. Such specimens were prepared by quenching through the transformation temperature into cold water. All specimens were kept in

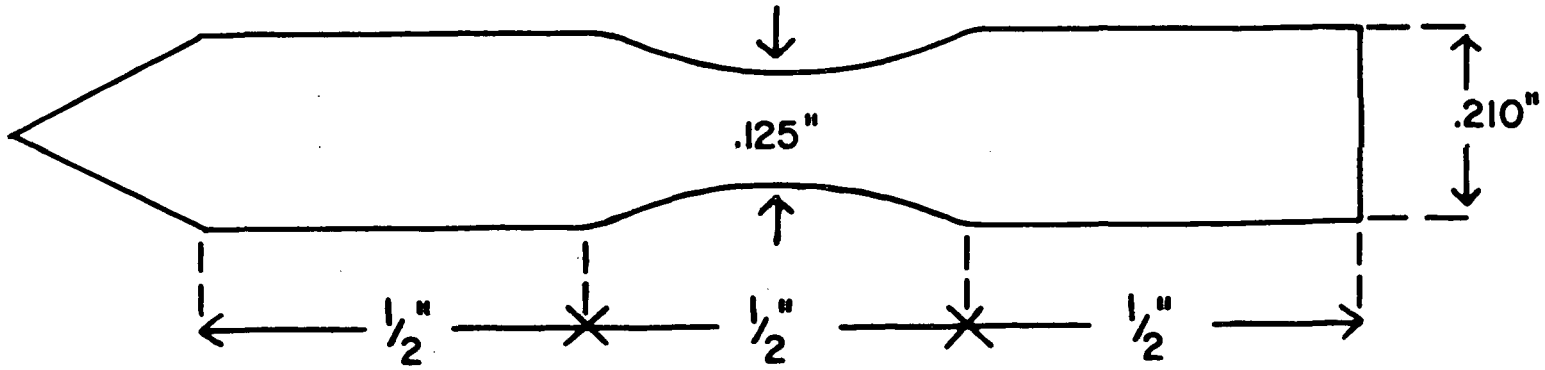

TYPICAL TENSION-COMPRESSION SPECIMEN

(a)

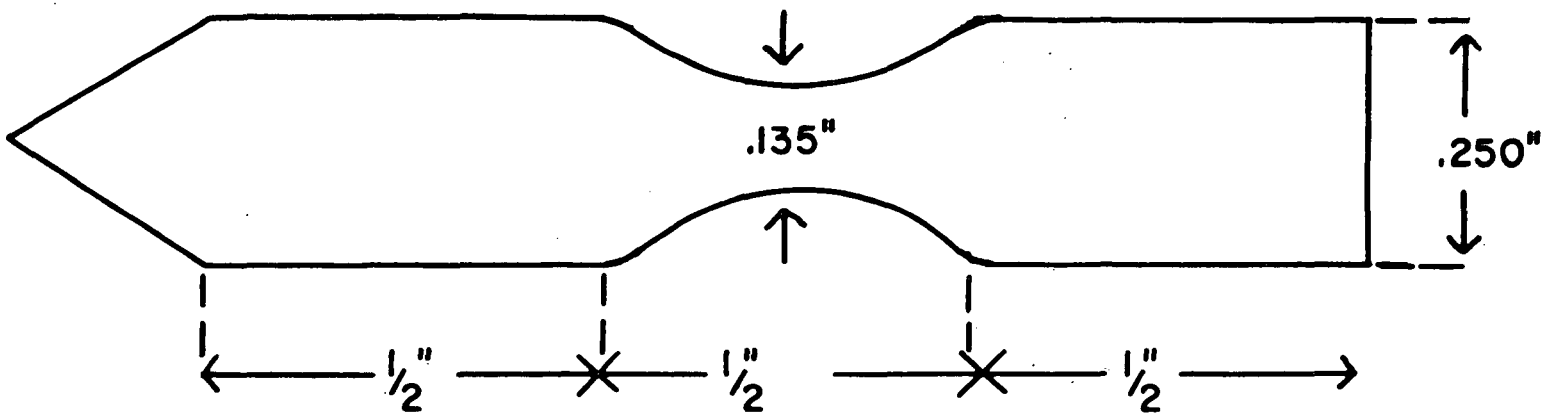

TYPICAL TORSION SPECIMEN

(b)

Figure 3. Typical cylindrical specimen dimensions.

the low temperature β' phase at least 25 hours following the β→β' transition prior to testing to assure complete stabilization of the twin boundaries.[12]

B. Twinning Geometry and Specimen Orientation

Orthorhombic AuCd exhibits twinning on the (111) plane in the irrational (-0.667, 0.377, 0.644) direction - type I twinning (Figure 4).[11] The n_1 twinning shear vector and the K_1 twin plane normal direction cosines relative to the specimen axis system orient the twin system;[17] this is the common way of expressing any homogeneous shear system. It is more convenient for x-ray orientation, however, to replace the n_1 direction with a rational low index vector directly identifiable on a Laue photograph such as the [001] chosen because it is the closest <100> to the (111) plane normal (42.81°) as shown in Figure 5. Since the [001] has a component in the (111) plane, this set of vectors, (111) [001], equivalently determines the twin system orientation.

Specimen orientation was aided by the fact that the twin composition plane, observable by microscopy, is the actual K_1 plane. A goniometer with the degrees of freedom shown in Figure 6 was employed to orient the specimen optically so the twin plane normal was approximately parallel to the incident x-ray beam.* The resulting Laue photographs, all centered on the twin plane normal, thus differed only by a rotation about the center of the film. Hence, identification of the Laue reflections in one photograph allowed rapid identification of the reflections in any other. The reflections from the (111) and (001) (parallel to the [001]) thus identified were rotated into the standard stereographic projection shown in Figure 7 with the east-west axis corresponding to the specimen axis and the north pole

---

* In practice the twin plane was oriented so its Laue reflection was just visible on the edge of the hole punched in the film and 10° from the incident x-ray beam.

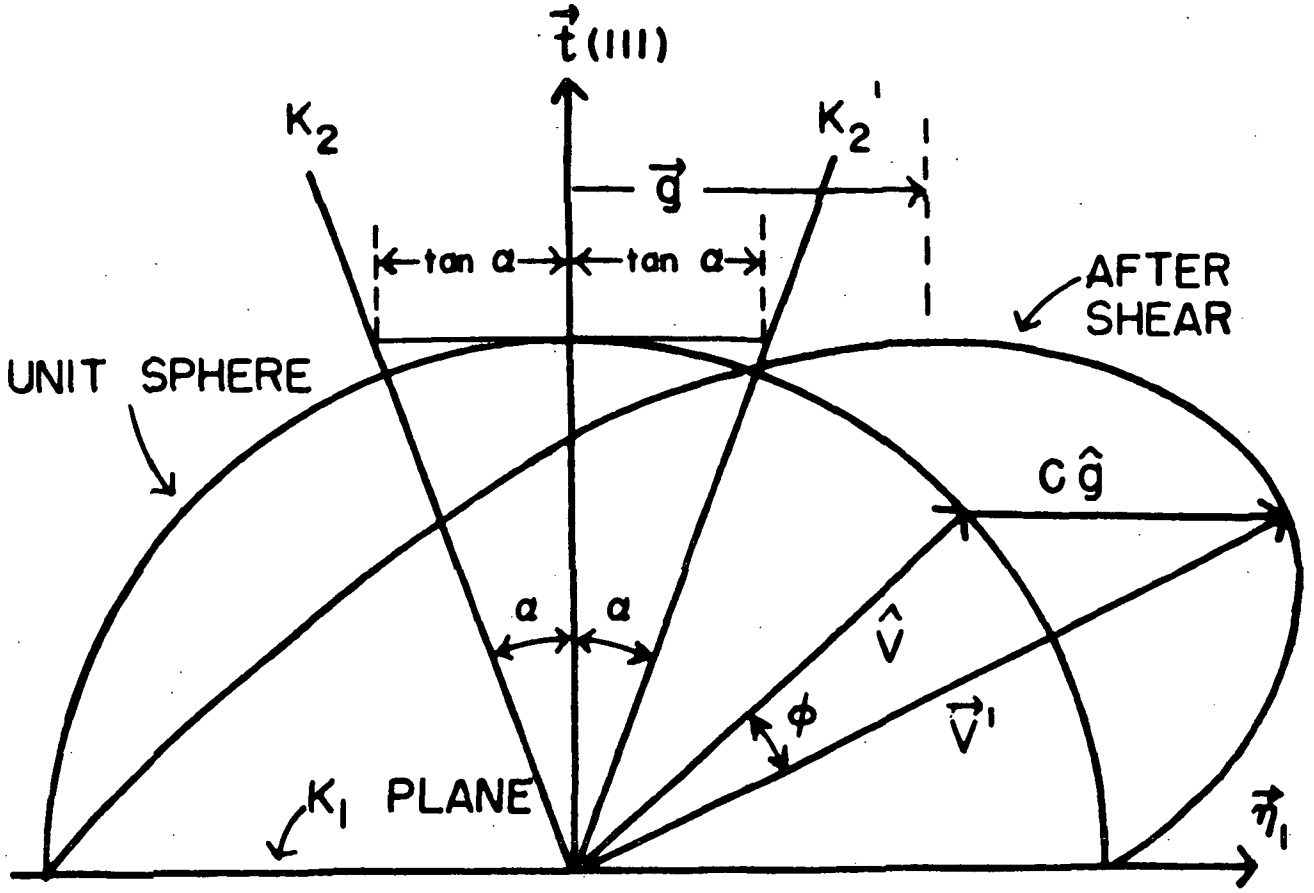

Figure 4. The distortion of a unit sphere by twinning. K_1 is the (111) twin plane whose normal is $\vec{t}$. $\vec{\eta}_1$ is the twinning shear direction, and $\vec{g}$ is the twinning shear at unit distance in the direction $\vec{\eta}_1$. The K_2 plane is rotated through angle 2α to K_2'. Twinning shears the tip of $\hat{V}$ by $C\hat{g}$ and rotates $\hat{V}$ by ϕ. (After References 8 and 9)

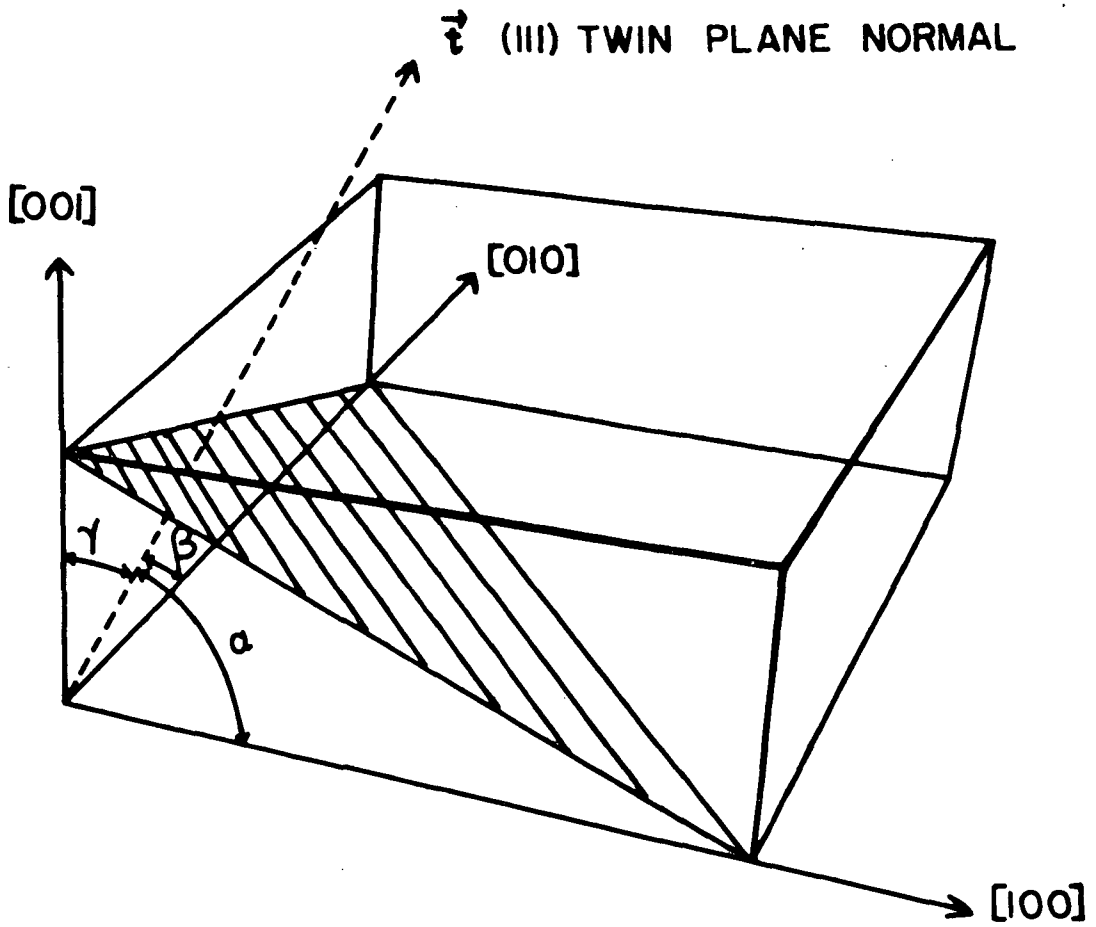

Figure 5. An exaggerated orthorhombic unit cell showing the orientation of the twin plane normal, $\vec{t}$, relative to the principal axes. $\alpha = 61.60°$, $\beta = 60.95°$ and $\gamma = 42.81°$. The (111) twin plane normal and the [001] are employed to orient and characterize the twin system as discussed in the text.

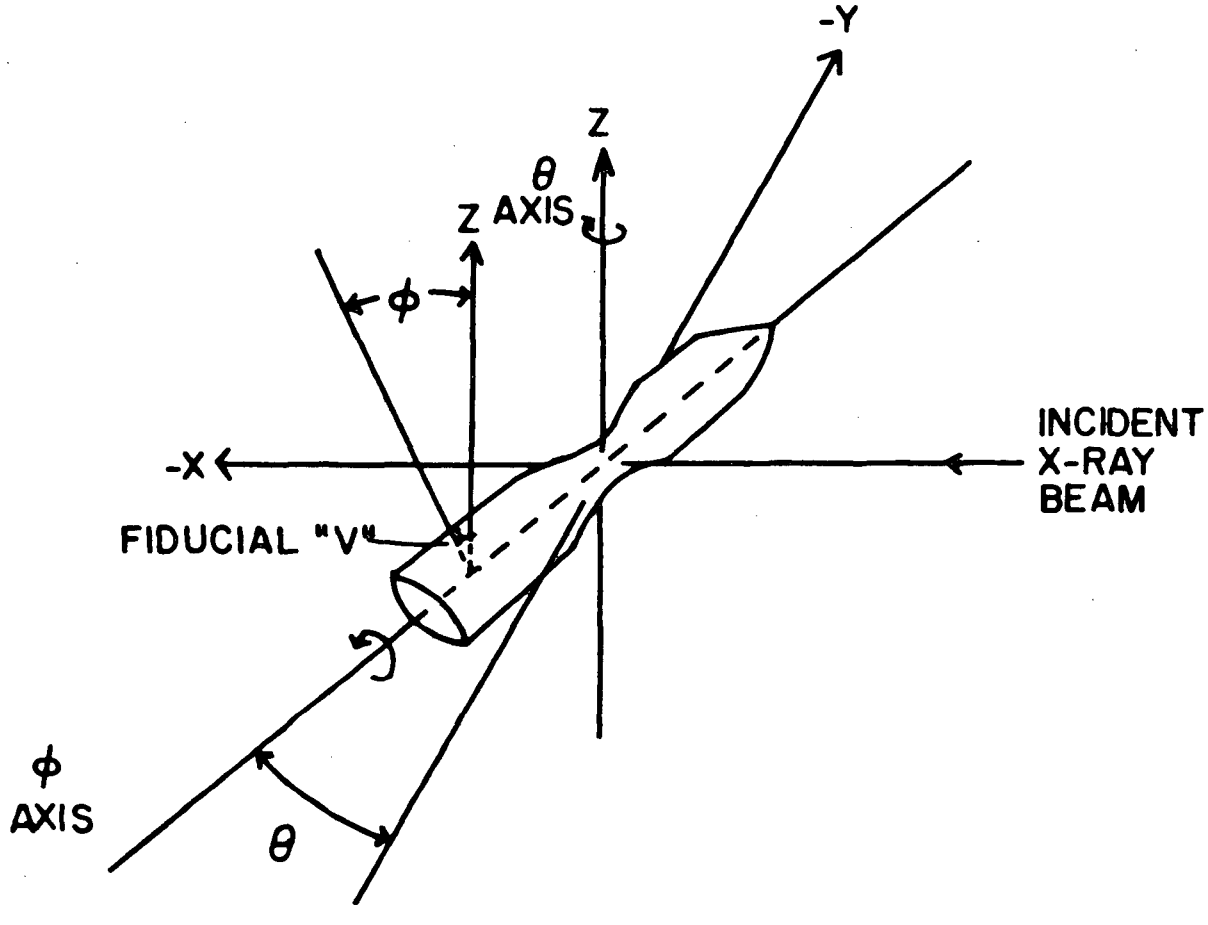

Figure 6. Schematic of the goniometer for x-ray orientation showing its degrees of freedom Θ, about the z axis measured from the +y direction, and ϕ, about the specimen axis measured from the vertical to the fiducial "V" on the shoulder.

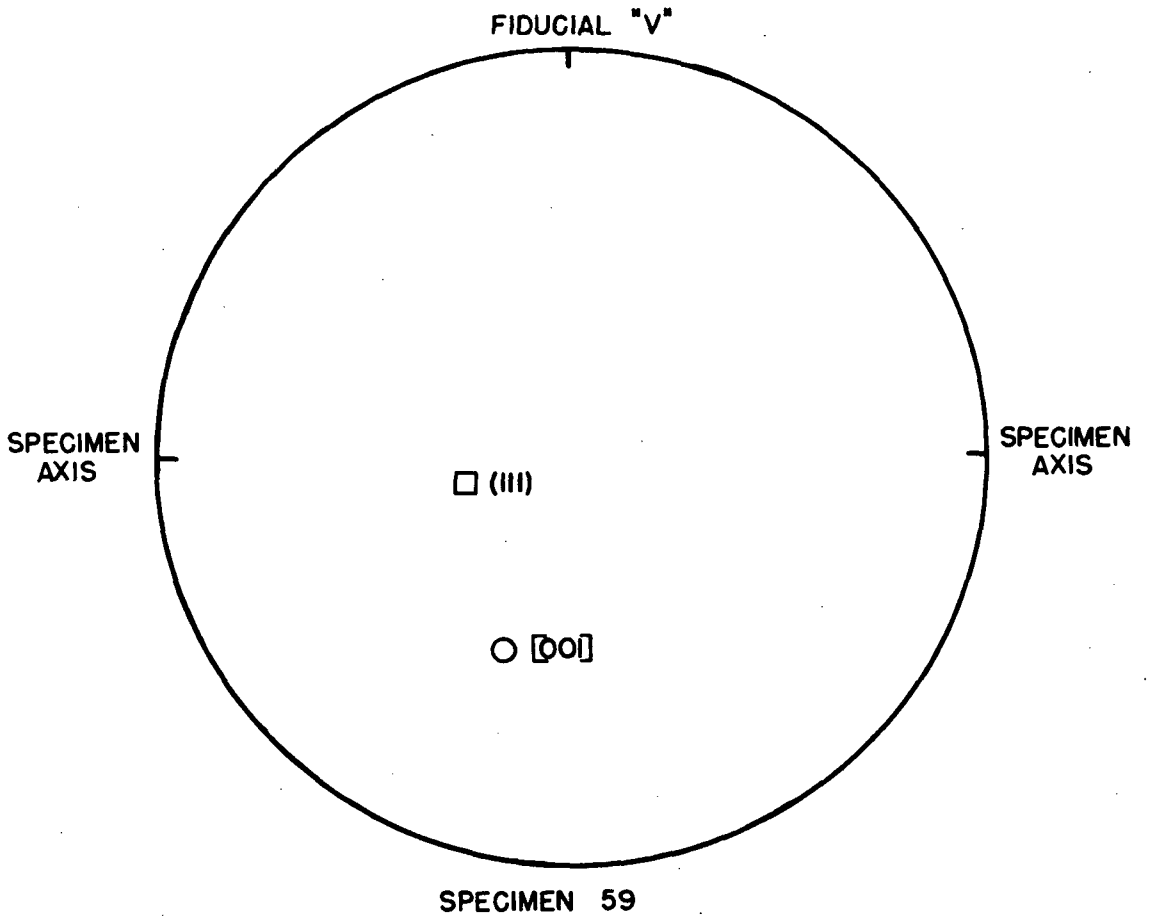

Figure 7. The stereographic projection of a typical twin system orientation expressed relative to the specimen axis system. The (111) twin plane and [001] of one twin are sufficient to characterize the system as discussed in the text.

corresponding to the fiducial "V" (Figure 6).

C. Mechanical Testing and Fractography

1. Tensile Testing

Four tensile specimens described earlier were tested on an Instron TTC machine at strain rates between 0.01 and 0.02 inches per minute. The specimens had 1-1/4 inch gage lengths, and strain was measured with a 1 inch clip-on extensometer. This machine was not suitable for tension-compression fatigue owing to its large overshoot at higher testing frequencies.

2. Torsion Fatigue Testing

Torsion fatigue tests were conducted on Satec SF-2U eccentric weight machine, a constant force device that operates at 30 Hz. Typical torsion specimen dimensions are shown in Figure 3. Collet grips were used, and the strain was estimated from the total twist of the specimen in degrees using the treatment in Appendix C.

3. Tension-Compression Fatigue Testing

Tension-compression fatigue testing was performed on a ±20 Kip Material Testing System electrohydraulic closed loop system, and collet type grips, aligned by means of a Wood's metal pot, were employed.[18] Most specimens were tested in load control due mainly to the observation early in the work of an abrupt transition to a high modulus region terminating deformation by twin boundary motion which resulted in highly variable peak loads and a certain amount of non-twin related (plastic) deformation when stroke (ram displacement) control was used.

Since the purpose of this research was to study deformation by twin boundary motion and not by classical plastic mechanisms, the load limits were generally set far below that for measurable plastic deformation but sufficiently high to observe the end of twin boundary motion. Because of the above argument against stroke control and because it was often necessary to move the diametral extensometer employed in strain measurement during testing (Section III), strain control testing was not attempted. The extensometer was mounted on a circular track graduated in degrees and concentric with the ram to facilitate its positioning relative to the fiducial "V" on the specimen (Figure 6). Testing frequencies were generally 6 to 7 Hz but were occasionally as high as 20 Hz and as low as 2×10^{-4} Hz. The shapes of the load-stroke and load-diametral strain hysteresis loops were monitored during testing on a CRT, and the loops were recorded on an x-y recorder at rates of 8×10^{-2} Hz and below at various times during testing. Failure was defined as the detection of a visible crack (~0.01").

4. Temperature Control

A simple temperature control system was devised to allow testing between -126°C and +65°C on the MTS machine. The system, shown schematically in Figure 8, employed a copper "T" inserted over the specimen before attaching the upper grip and some copper tubing. Dry helium was forced through the tubing which was either heated over a bunsen burner or cooled by immersion in liquid nitrogen. Temperature was measured with a copper-constantan thermocouple and controlled by regulating the gas pressure to ±4°C for heating and ±2°C for cooling.

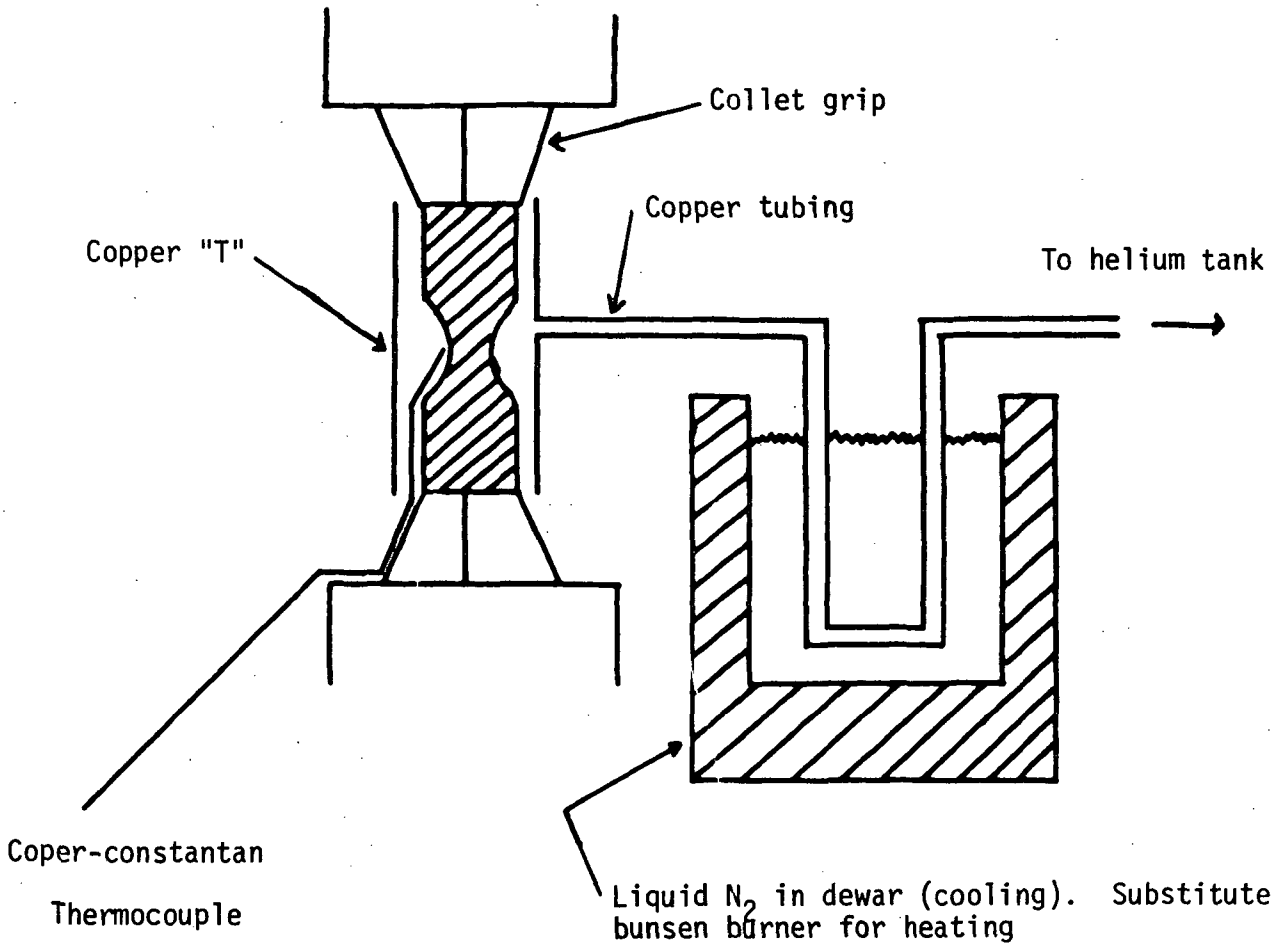

Figure 8. Schematic drawing of the temperature control system used with the MTS testing machine in the range -126°C to +65°C.

5. Fractography

Fracture surfaces were observed in a Jeolco JSM-13 scanning electron microscope and a Zeiss polarized light microscope using the Nomarski objectives.

III. THE CRYSTALLOGRAPHY OF STRAIN AND THE PREDICTION OF MECHANICAL BEHAVIOR

Hourglass specimens are commonly employed for high strain (> ±2 percent) fatigue in isotropic materials to prevent buckling.[19] This shape requires diametral strain measurements which are easily converted to longitudinal strain in isotropic specimens (e.g., fine grained steel) but not in the anisotropic specimens of orthorhombic AuCd with a single set of (111) twins. However, by incorporating the (known) arbitrary specimen orientation and the geometry of twinning delineated above into a model, an algorithm was devised which permits the calculation of the maximum strain in arbitrary directions (i.e., a strain ellipsoid) when the specimen is converted from all of one twin to all of the other. In fact, the specimen may only be partially converted, in which case the strains would be simply related to the maximum strains by a proportionality factor less than one. Now the very anisotropy of a single set of orthorhombic AuCd twins can be exploited to predict the actual strains expected in any direction from a single measured strain without the need to determine the amount of actual twin conversion. In particular, a measurable strain such as a diametral strain could be used to calculate an immeasurable strain of interest, namely the longitudinal strain at the midsection. Such a model was developed, validated, and used in this work. The algorithm is discussed in greater detail in Appendix D.

Figure 9 shows the predicted diametral strain pattern for Specimen 62 transformed to a single set of twins during the compression to tension half of the stress-strain hysteresis loop assuming complete twin conversion.

Figure 9. The predicted diametral strain pattern on increasing axial tensile strain for Specimen 62 assuming complete twin conversion. ϕ is the angle of rotation about the specimen axis between a diameter and the fiducial "V" as shown in Figure 6. Note the region where diameters are <u>increasing</u> on <u>increasing</u> tension in the vicinity of $\phi = 150°$.

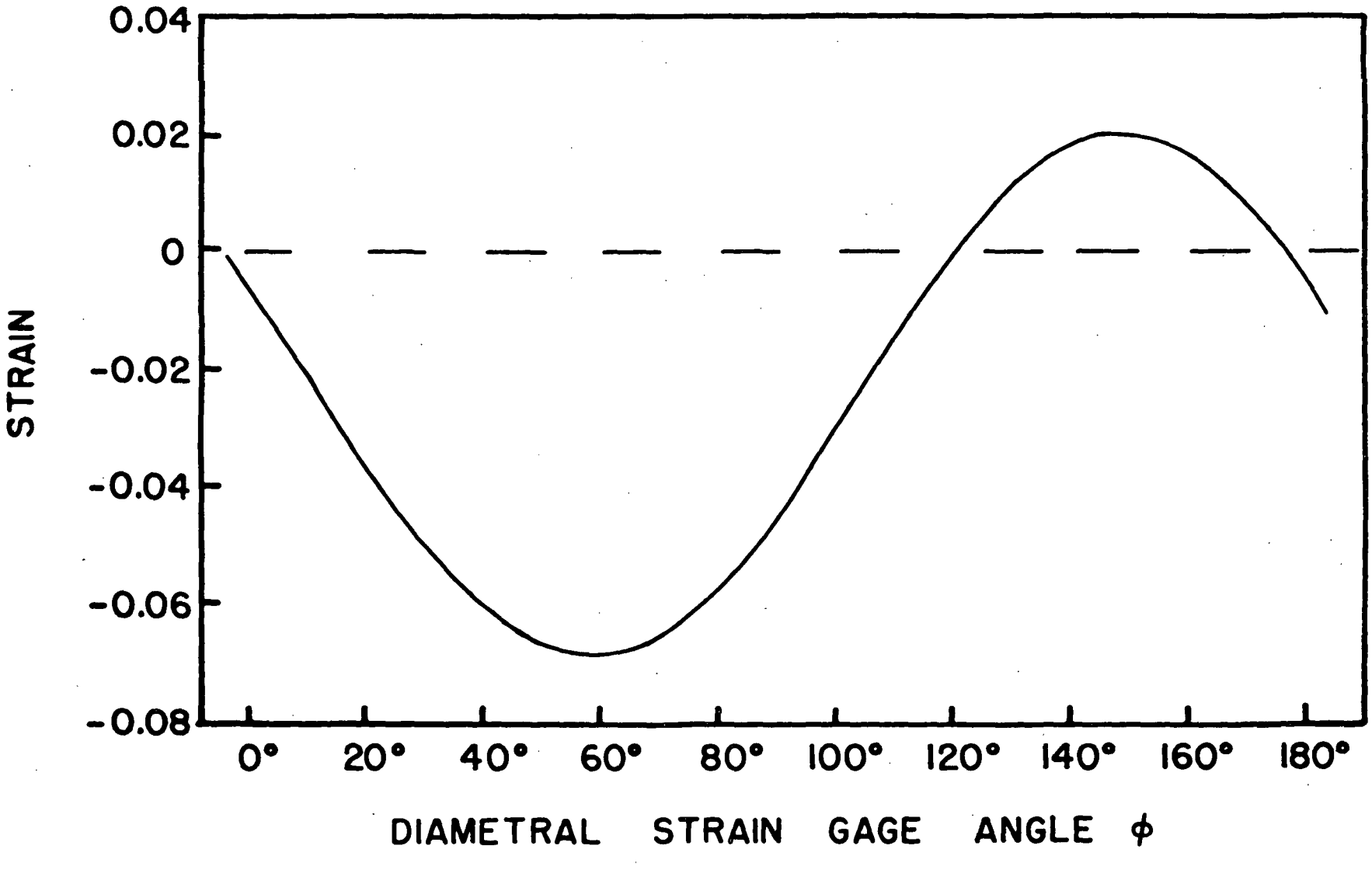
0.04
0.02
0
-0.02
-0.04
-0.06
-0.08
STRAIN
0°
20°
40°
60°
80°
100°
120°
140°
160°
180°
DIAMETRAL STRAIN GAGE ANGLE ϕ

The diametral orientation is defined by the angle from the fiducial "V" (Figure 6); negative strain indicates a decreasing diameter on increasing tensile stress. Note the extreme anisotropy predicted for the diameters between $\phi = 130°$ and $\phi = 180°$ which are calculated to <u>increase</u> with <u>increasing</u> tensile strain. This predicted strain pattern (Figure 9) will be compared with the measured strain in Section IV, A.

The major application here of the algorithm is for determining "favorable" and "unfavorable" orientations, that is, for predicting the extent a specimen can be expected to strain to relieve axial stress through twin boundary motion (LeChatelier's principle). A more intuitive understanding of the physical significance of "favorable" and "unfavorable" orientations may be obtained from a geometric argument which parallels the algorithm. Figure 10 is the schematic representation of how one set of twin lamellae in a single region specimen grows at the expense of the other in response to stress. From the geometry of twinning discussed in Section II, B and shown in Figure 11, the largest strain which could result from complete conversion of one twin to the other involves the interchange of $2\underline{a}$ and $\sqrt{b^2 + c^2}$ (see Figure 11) and is calculated from the lattice parameters (and subsequently verified experimentally) to be ~0.076. As can be seen in Figure 11, $2\underline{a}$ is along [001] in one twin, and $\sqrt{b^2 + c^2}$ is only 4.4° from the [001] in the other twin.

The choice of the [001] (along with the (111) K_1 plane) to characterize the twin system orientation (Section II, B) is now seen to have most advantageous and important consequences: it permits the easy identification of the direction of maximum strain during twin conversion (which, as mentioned above, is along the [001] and the prediction by inspection of how arbitrarily

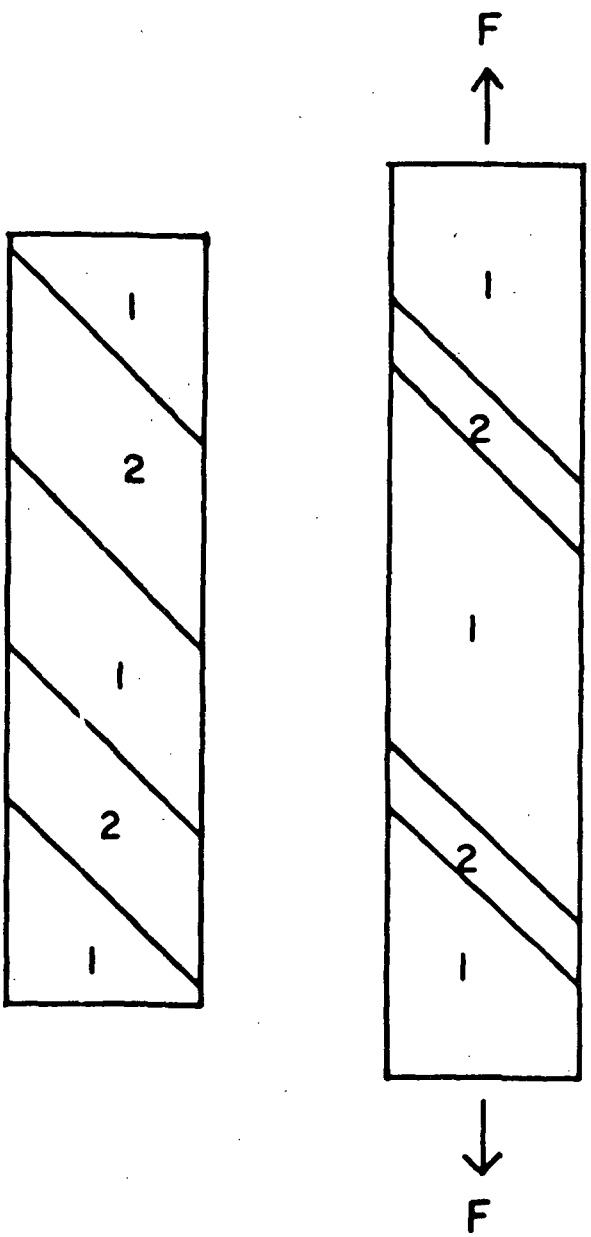

Figure 10. Representation of a single region specimen with twin orientations (1) and (2) showing schematically how orientation (1) grows at the expense of orientation (2) in response to load F.

Figure 11. (a) Two primitive cells placed together to form a unit cell 2a x b x c to illustrate (111) twins. $\underline{a}$ = 3.1540 Å, $\underline{b}$ = 4.7645 Å, and $\underline{c}$ = 4.8644 Å. (b) The same unit cell as (a) in a twin related positon showing their common (111) plane. (c) Unit cells (a) and (b) joined together along the (111) twin plane. Note that twinning has the effect of interchanging 2a with a vector length $\sqrt{b^2 + c^2}$. (After Schmerling[8])

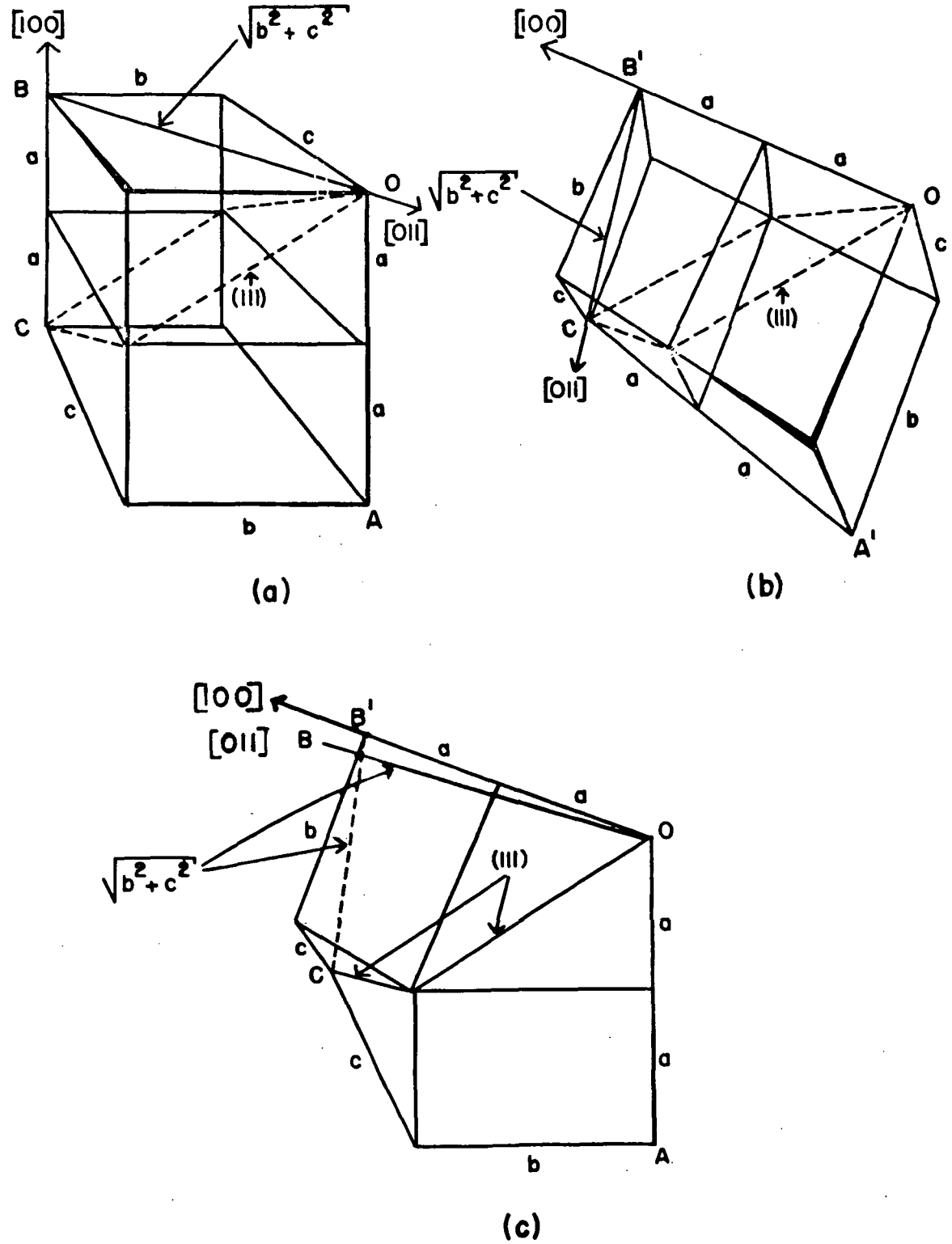
[100]
$\sqrt{b^2+c^2}$
B
b
a
c
O
[011]
a
(111)
C
c
a
b
A
(a)
[100]
B'
a
a
b
$\sqrt{b^2+c^2}$
O
c
c
C
[011]
a
(111)
b
a
A'
(b)
[100]
[011]
B'
B
a
a
b
$\sqrt{b^2+c^2}$
O
(111)
a
c
C
c
a
b
A
(c)

oriented crystals will (or will not) respond to axial tension or compression by twin boundary motion, i.e., by the growth of one twin at the expense of the other to relieve the stress. The two twin related [001] short 2a axes are 85.62° apart, and hence would represent a favorable orientation for deformation if one [001] is approximately parallel to the specimen axis since the [001] in the other twin must be close to perpendicular to it. Thus, the twin represented by the first [001] would grow in compression while that represented by the second would grow in tension. When the two [001] axes make the same angle with the specimen axis, however, the orientation would not be favorable for deformation by twin boundary motion since twin conversion would not change the specimen length. The two above examples suggest that one measure of a specimen's ability to respond to longitudinal stress is the difference between the angles the two twin related [001] axes make with the specimen axis; a large difference corresponds to a favorable specimen orientation.

Figure 12 is the stereographic projection of a typical single region specimen with the two twin orientations represented by their [001] orthorhombic axes as described above. The difference between the angles the two [001] axes make with the specimen axis may be expressed in terms of the angles γ and δ (Figure 12). γ is the angle the $(111)_T$ twin plane normal makes with the tension axis. The $(111)_T$ must, by twinning crystallography, bisect the arc joining the two [001] axes. Thus when γ is zero or $\pi/2$, the [001] axes must be equiangular with the specimen axis, and converting one twin to the other will produce zero longitudinal strain. However, a γ value near $\pi/4$ would allow the difference between the angles the

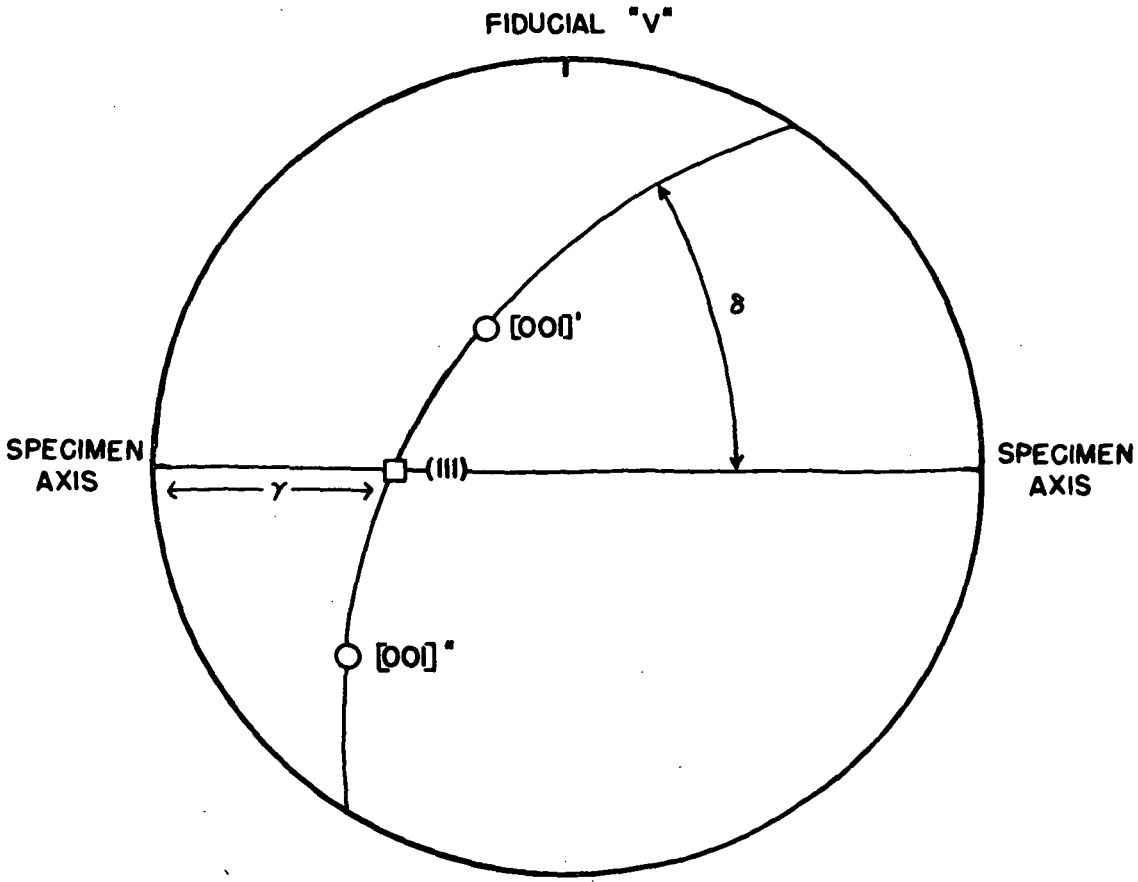

Figure 12. Definition of the angle γ between the specimen axis and the (111) twin plane and the angle δ between a great circle through the specimen axis and one through the twin related [001]' and [001]" orientations. δ is measured 90° from the great circle intersections at the (111).

two [001] make with the specimen axis to be closest to the maximum value of 85.62° (the angle between two twin related [001] directions) and thus allow the maximum longitudinal strain amplitude.

Since the strain amplitude (for complete twin conversion) should be a smoothly varying function of γ, this suggests a γ dependence of the form $\sin \gamma \cos \gamma$ which is zero at $\gamma = \pi/2$ and $\gamma = 0$ and maximum at $\gamma = \pi/4$. δ is the angle between the great circle through the twin plane including the [001] axes and that through the twin plane which includes the tension axis. Regardless of the γ value, a δ value of $\pi/2$ will cause the [001] axes to be equiangular with the specimen axis and thus allow no longitudinal strain by twin boundary motion. Since the strain amplitude should vary smoothly with δ and is maximum for $\delta = 0$, this suggests a δ dependence of the form $\cos \gamma$ and a reasonable approximation to the overall dependence of the form:

$$\text{Total Strain Amplitude} \quad \tilde{\alpha} \quad \sin \delta \cos \gamma \cos \delta \qquad (1)$$

In the next section the above treatment is applied to stereographic projections of specimens with a single set of transformation twins to predict if they will respond to relieve axial stress by a) the motion of twin boundaries, b) mechanical twinning, or c) neither. It is also applied to twinning in orthorhombic single crystals where there was only one [001] axis present but four possible twinning systems on the four (111) planes. All twinning systems must be considered to determine which gives the largest axial strain amplitude and would therefore be expected to operate. The anticipated diametral strain pattern may also be calculated as described earlier. Since deformation by twin boundary motion involves no volume change, strains in

multiple region specimens - or single region specimens whose orientation is unknown - may be determined from the diametral strain data by determining the change in cross sectional area. Strains in polycrystalline and unfavorably oriented specimens not exhibiting twin boundary motion may be estimated from the stroke amplitude using the treatment in Appendix E.

IV. EXPERIMENTAL RESULTS AND PARTIAL DISCUSSION

A. Diametral Strain Patterns

Figure 13 compares the predicted diametral strain pattern on increasing tensile strain (Figure 9) with that measured with a diametral extensometer for Specimen 62. Both curves show a large segment where diameters increase with increasing tension, and the peak strain amplitudes, both positive and negative, match to within 5%. The only significant discrepancy is a 10 degree phase shift between the curves due mainly to fixed errors introduced in fiducial mark placement and extensometer alignment. Owing to the small specimen diameters (0.210 inches), a total error equivalent to an 0.02 inch displacement of the fiducial mark would account for the discrepancy. In addition, a smaller fixed error (± 2°) in positioning the predicted curve is introduced during x-ray orientation. The accuracy of the algorithm in predicting the diametral strain pattern of a random specimen orientation establishes its validity for use in determining tensile strain as described in Section III. The algorithm was applied to the eight single region and orthorhombic single crystal specimens exhibiting twin boundary motion and predicted the observed diametral strain pattern in all cases, the only discrepancy being a phase shift of less than 15 degrees.

The ratio of the observed strain amplitude to that predicted for complete twin conversion is shown plotted against the predicted strain in Figure 14 for single region and single crystal orthorhombic specimens. Note that above 0.045 predicted strain, $\varepsilon_{measured}$ and $\varepsilon_{predicted}$ (ε_m and ε_p) agree while below 0.03 predicted strain, no deformation by twin boundary motion was observed. Another way of plotting the data to make the explanation of

Figure 13. Comparison of the measured diametral strain pattern on increasing tensile strain with that predicted (Figure 9) for Specimen 62. Note that both curves show certain diameters increasing on increasing tensile strain and that the strain amplitudes match well; the phase shift is associated with a fixed error estimated at ±15° discussed in the text.

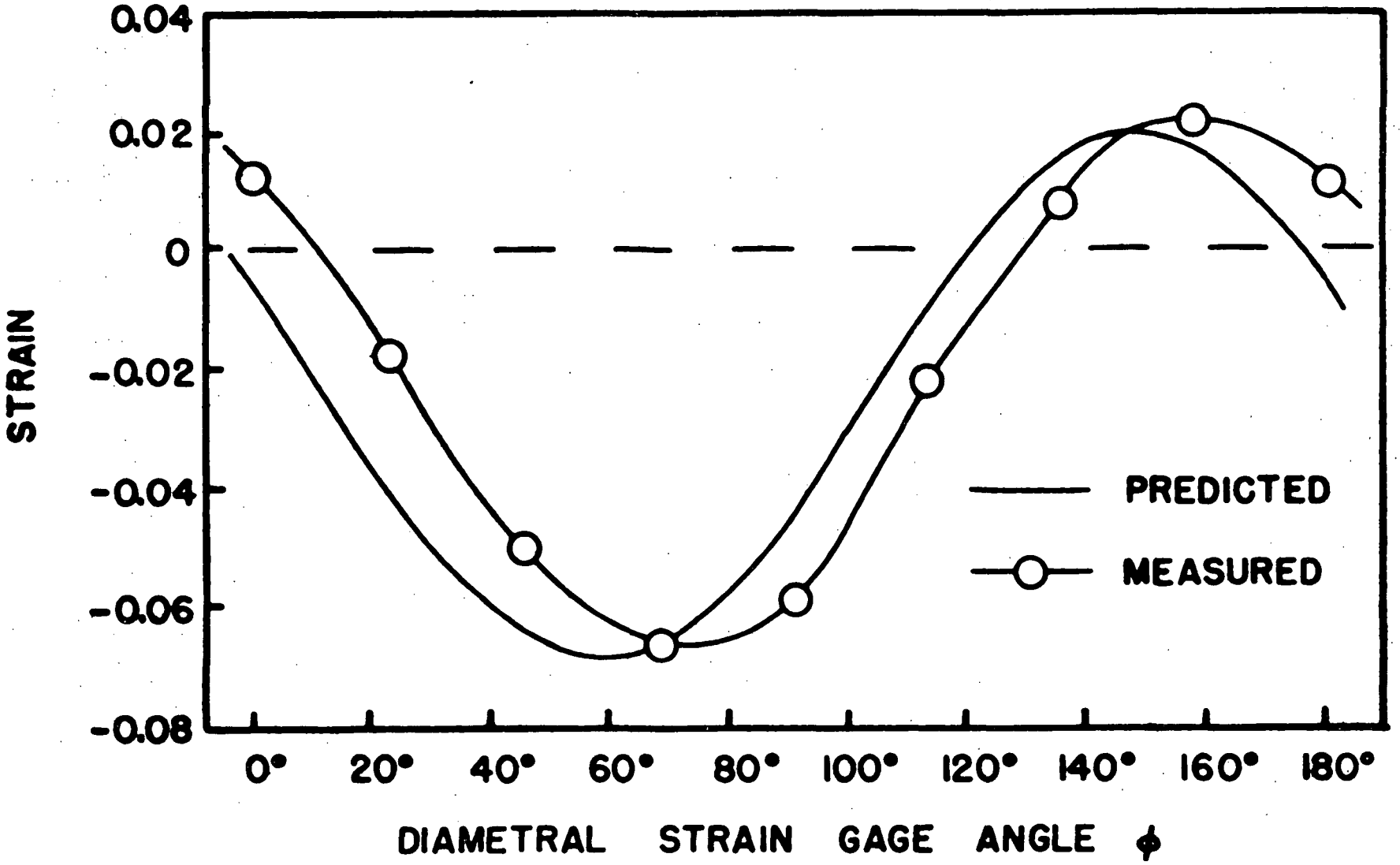
0.04
0.02
0
-0.02
-0.04
-0.06
-0.08
STRAIN
0°
20°
40°
60°
80°
100°
120°
140°
160°
180°
DIAMETRAL STRAIN GAGE ANGLE φ
PREDICTED
MEASURED

Figure 14. The ratio $\varepsilon_m/\varepsilon_p$. Above 0.045, $\varepsilon_m \approx \varepsilon_p$ while below 0.035 no deformation on the predicted twin system was observed. The specimens in the transition region are discussed in Section V, A.

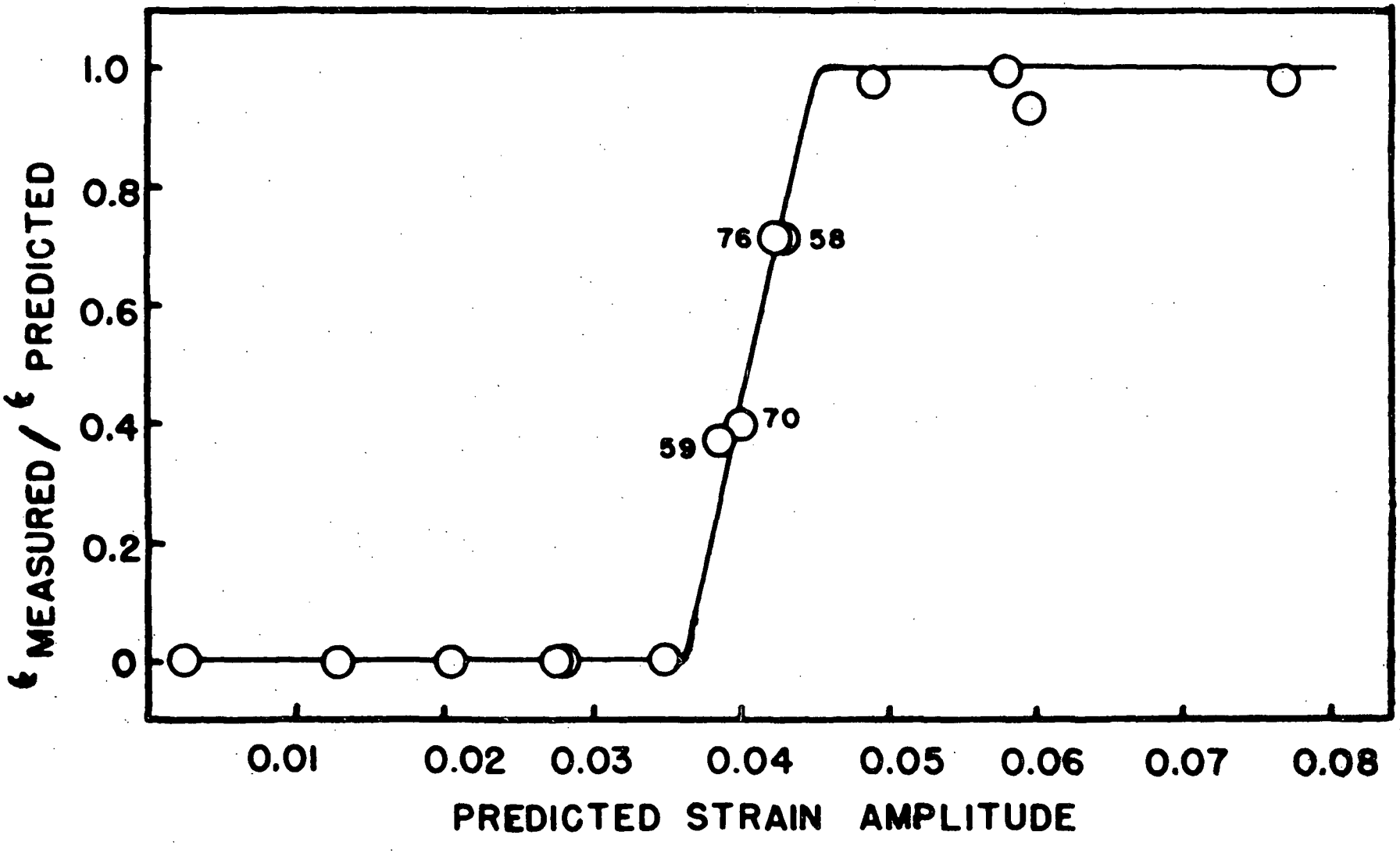
1.0
0.8
0.6
0.4
0.2
0
76
58
59
70
0.01
0.02
0.03
0.04
0.05
0.06
0.07
0.08
PREDICTED STRAIN AMPLITUDE

the behavior more tractable will be shown below. Thus, Figure 15 shows that the ratio $\varepsilon_m/\varepsilon_p$ varies in a corresponding way with the fraction of the applied tensile stress resolved as shear stress on the twin plane in the twinning direction (calculated in Appendix F). Examining the behavior in this way will be shown to be more fruitful (Section V, A).

B. Mechanical Behavior

1. Deformation by the Motion of a Single Set of Twin Boundaries

Figure 16 is the stereographic projection of Specimen 58 which was predicted to deform by transformation twin boundary motion in both tension and compression because of favorable γ and δ values (Section III, Expression 1). This specimen's behavior matched the algorithm's predictions as shown by the tension to compression stress-strain hysteresis loop (henceforth called the "hysteresis loop" or "loop") in Figure 17. When the tensile stress was increased from zero, a narrow, high modulus region was first observed followed by a rather abrupt transition or threshold to a low modulus region as twin boundaries moved and one twin grew at the expense of the other. Because of its shape, this portion of the stress-strain loop will henceforth be referred to as a "stress step". When twin boundary motion ceased (i.e., when the specimen was completely converted to one twin orientation), another high modulus region was observed. There was a third high modulus region on unloading followed by another low modulus region as the twin orientation that previously grew under stress contracted and the twin boundaries returned to their original positions in response to a restoring force that apparently originates within the twin volumes.[8] The compressive portion of the loop showed similar behavior to that in tension.

Figure 15. The fraction of the predicted longitudinal strain actually observed, $\varepsilon_m/\varepsilon_p$, vs the fraction of the applied stress resolved on the twin plane in the twinning direction. These data correlate with those of Figure 14 with a resolved stress fraction above 0.30 corresponding to a predicted strain above 0.045 and that below 0.13 corresponding to a strain prediction below 0.035. The data in the transition region are discussed in Section V, A.

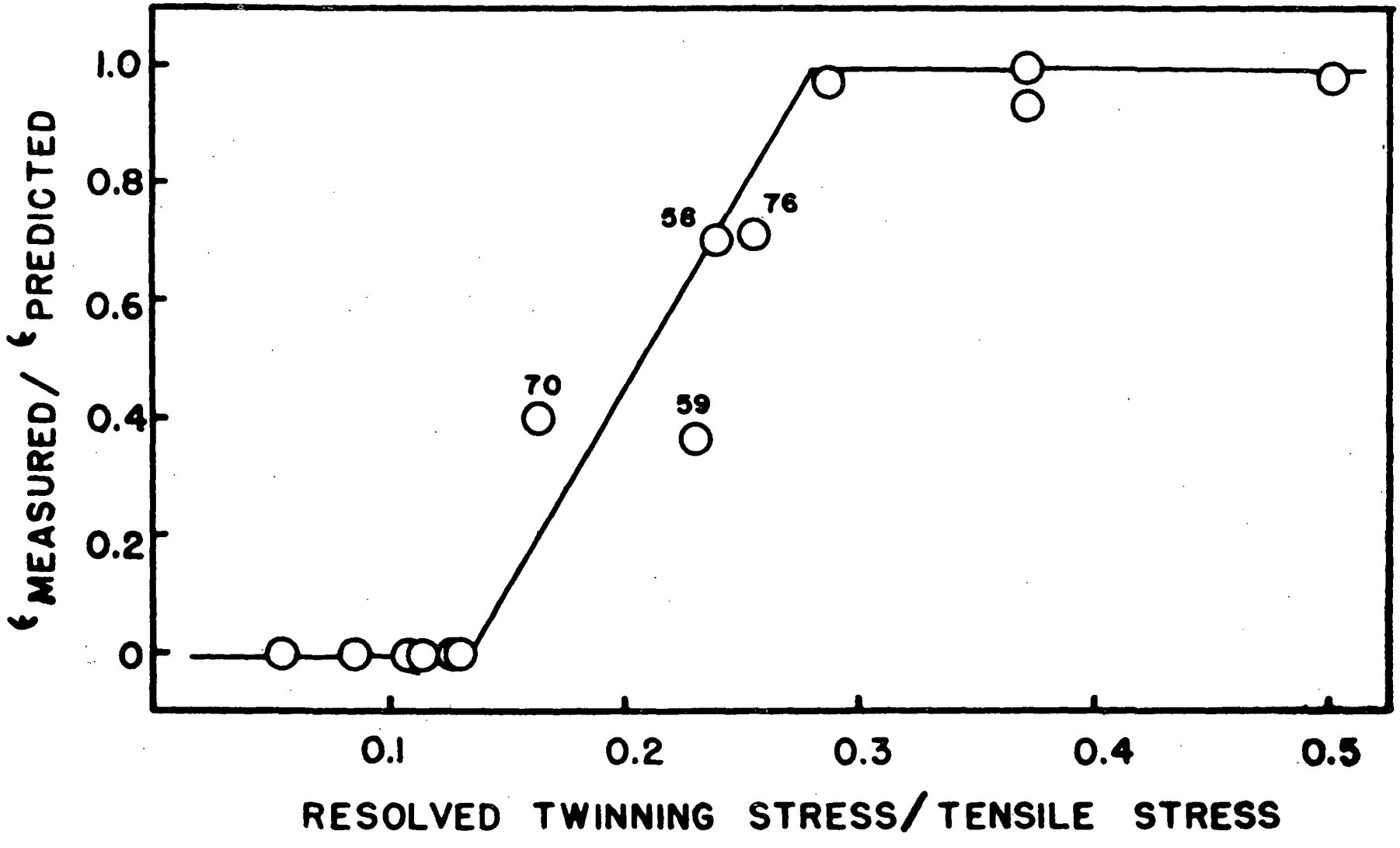
1.0
0.8
0.6
0.4
0.2
0
'MEASURED/ 'PREDICTED
58
76
70
59
0.1
0.2
0.3
0.4
0.5
RESOLVED TWINNING STRESS/TENSILE STRESS

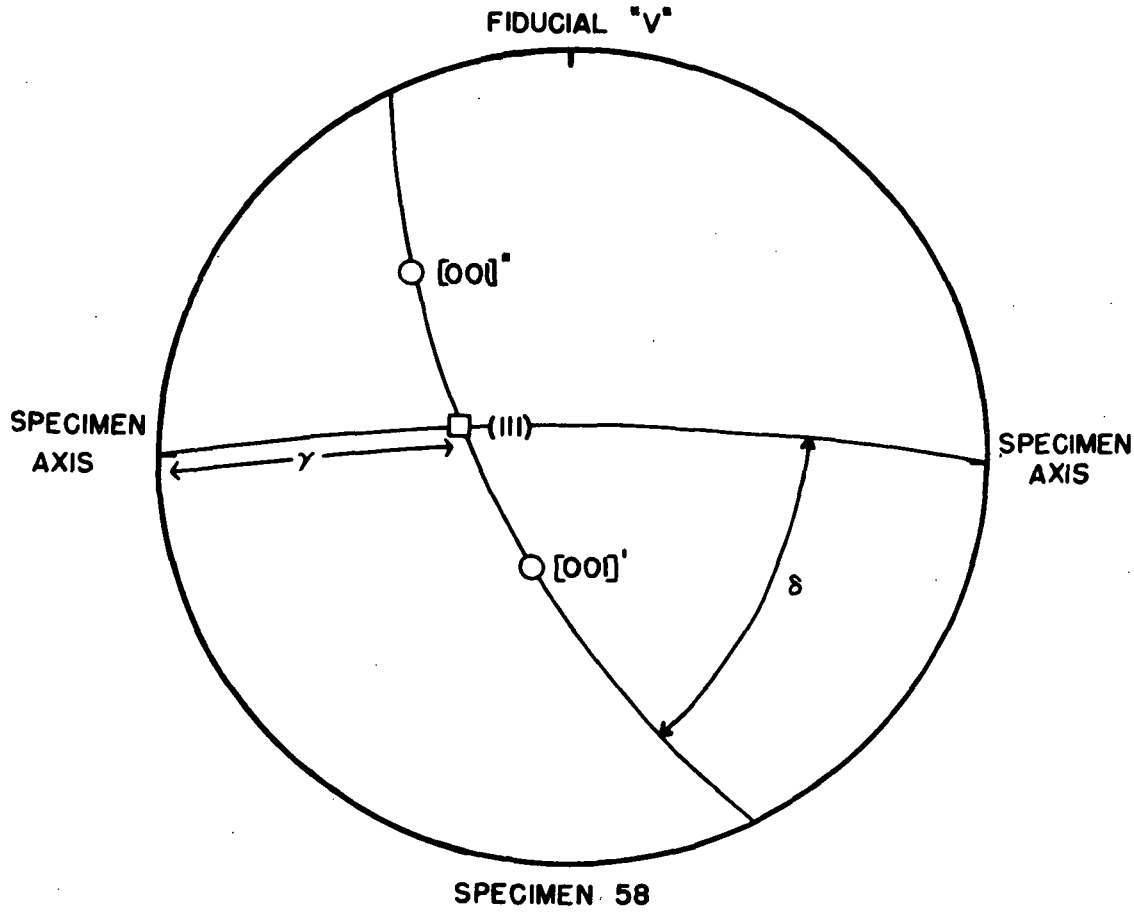

Figure 16. The stereographic projection of single region Specimen 58 showing favorable γ and δ values for deformation by transformation twin boundary motion (Section III, Expression 1).

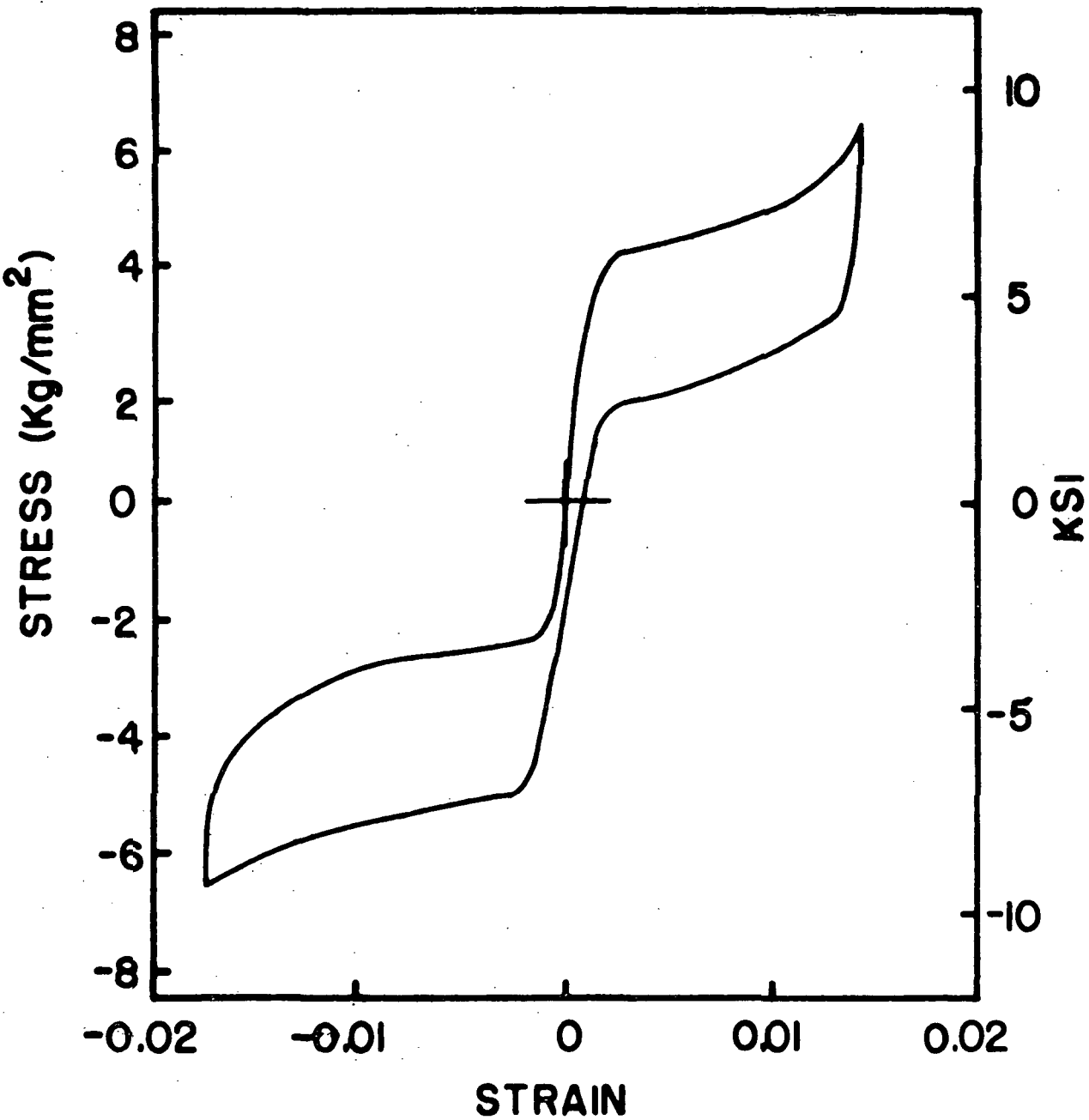

Figure 17. Hysteresis loop for single region Specimen 58 deforming by transformation twin boundary motion early in fatigue life (cycle 25). Note the abrupt "stress steps" near zero strain in both tension and compression discussed in the text.

The loop showed less than 0.001 strain hysteresis at zero stress and remained essentially unchanged for the first 10,000 cycles. Over the next 20,000 cycles the loop gradually changed to that shown in Figure 18 and then remained essentially unchanged as long as cycling was continued. The modulus associated with twin boundary motion was still rather low (215 Kg/mm^2) but higher than in the initial cycles (102 Kg/mm^2), and the stress step at zero strain (Figure 17) had disappeared. The other two high modulus segments at the strain limits after the specimen had been converted to all of one orientation or the other and at the start of unloading were still observed. There was also a substantial strain remnant. Loops similar in shape to that in Figure 18 showing no stress steps will be called "stable" loops. This terminology is employed to conform to conventional fatigue usage. It should not be confused with the volume stabilization process and well-stabilized specimens.

2. Deformation by Mechanical Twinning When Transformation Twin Boundary Motion Is not Possible

Deformation by transformation twin boundary motion was predicted to be impossible for Specimen 73 because, as can be seen from its stereographic projection in Figure 19, $\gamma \approx \frac{\pi}{2}$ (Section III, Expression 1). Both transformation twin orientations are twin related, however, to a potential twin shown as $[001]_M$ in Figure 19 which is more favorably oriented than either transformation twin to relieve compressive stress. Such stress did indeed nucleate spikes of material twin related to both transformation twins. These spikes spread across the specimen and widened as shown in Figure 20. The geometry of this mechanical twinning[20] is shown in Figure 21, and the

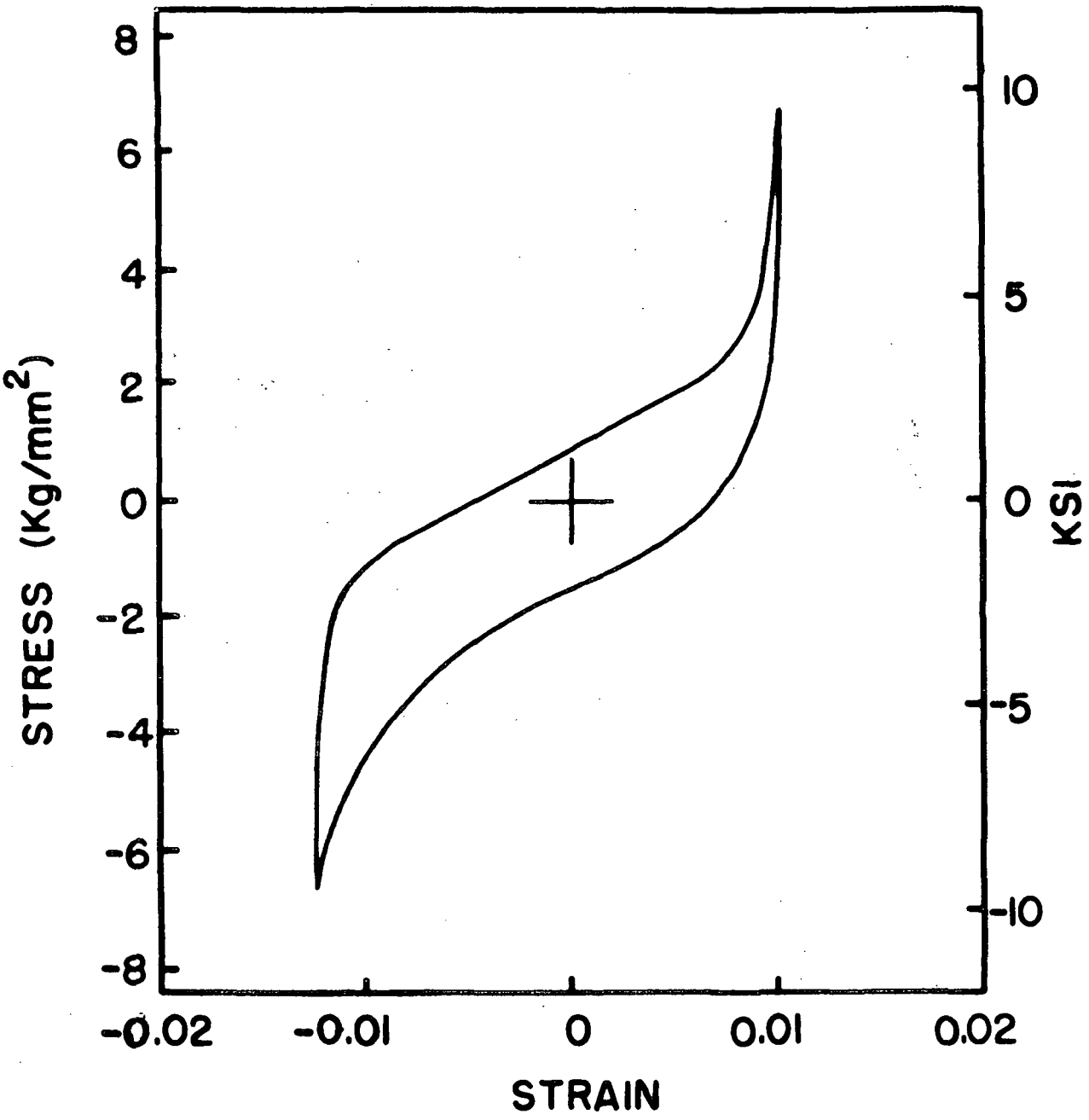

Figure 18. Stable loop of single region Specimen 58 late in fatigue life (100,000 cycles). Note the absence of the stress steps present in Figure 17; see text. (Same scale as Figure 17.)

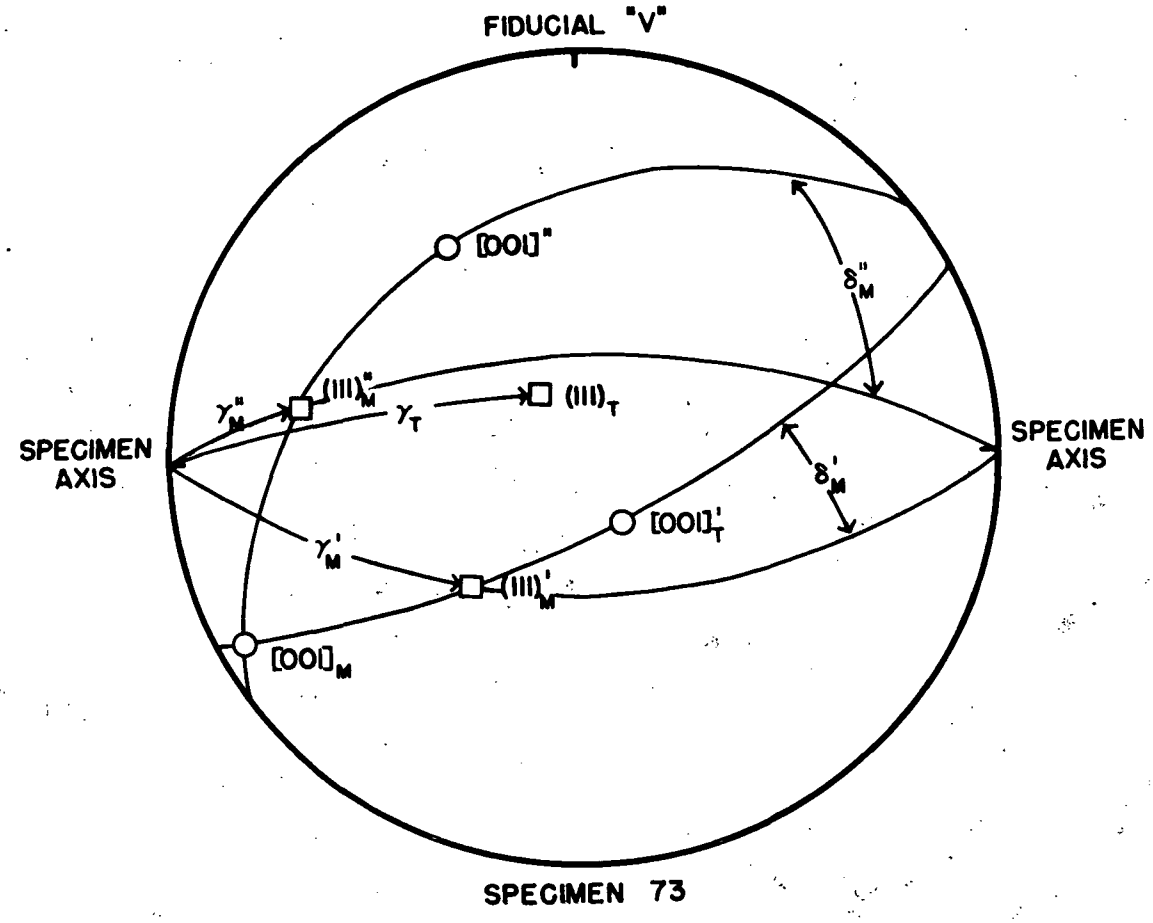

Figure 19. Stereographic projection of single region Specimen 73. The subscript "T" refers to the transformation twin system orientation and "M" to the mechanical twin system. The former cannot operate because $\gamma_T \approx \pi/2$ (Section III, Expression 1). Both transformation twins, $[001]'_T$ and $[001]''_T$, are twin related to a mechanical twin, $[001]_M$, across the $(111)'_M$ and $(111)''_M$ twin planes respectively. Owing to favorable γ and δ (not shown) values, the $[001]_M$ is favorably oriented to relieve compressive stress.

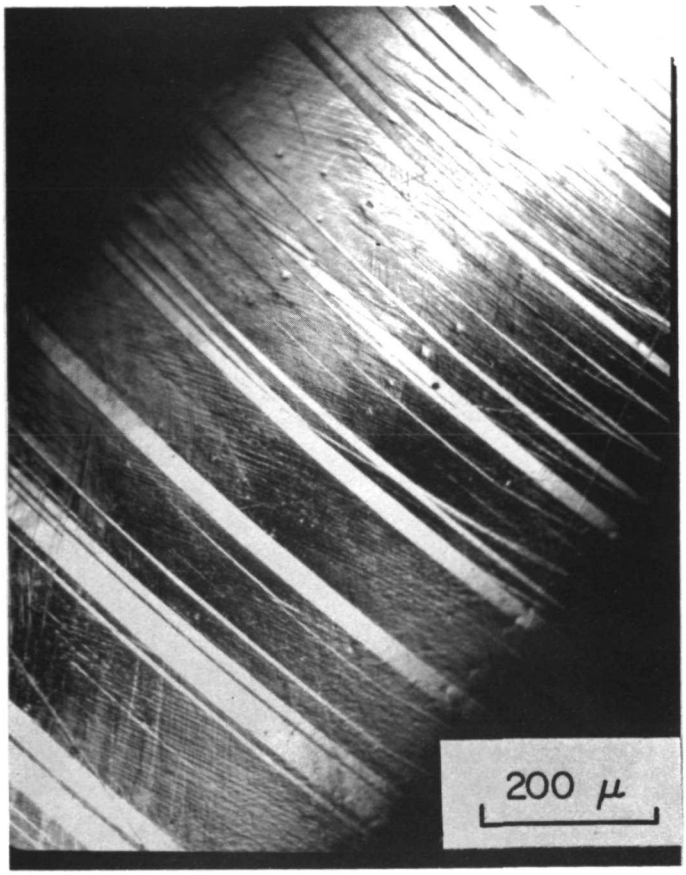

Figure 20. Mechanical twin spikes on the surface of single region Specimen 74. Note that in the mechanical twins (white), no transformation twins were seen by Nomarski technique at 200x, and the mechanical twin composition plane does not change direction at the transformation twin boundaries visible in the darker regions.

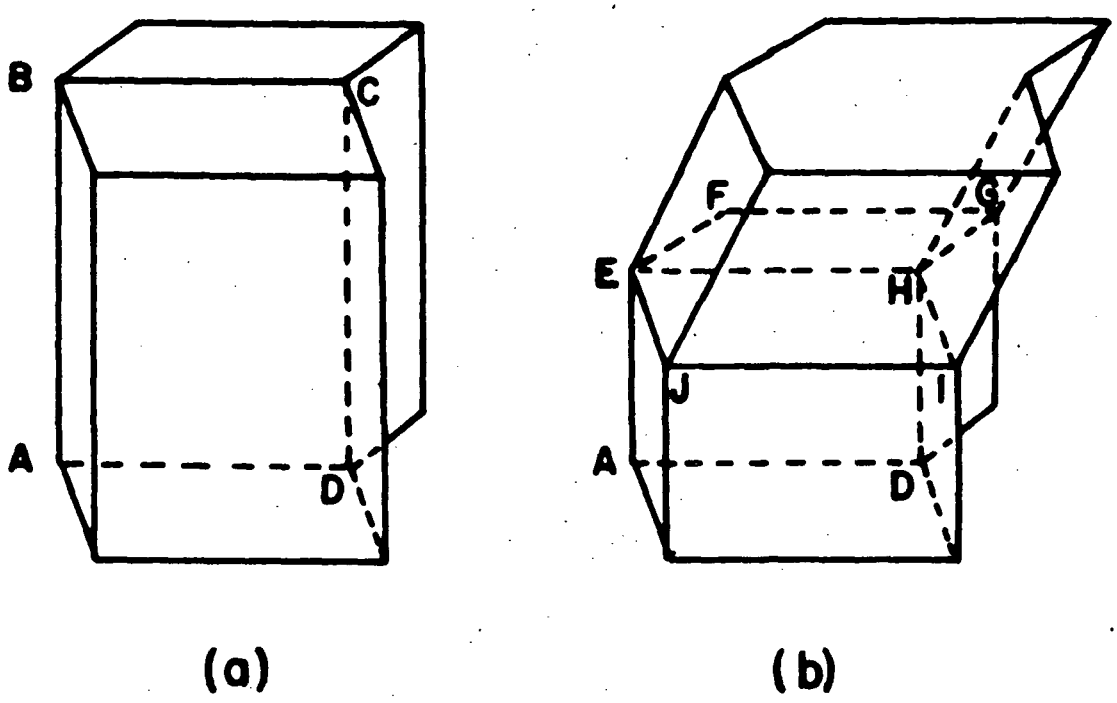

Figure 21. Very schematic geometric representation of the situation in Figure 20 consistent with Figure 19. (a) shows two regions twin related across the (111) transformation twin boundary ABCD. (b) shows the introduction of a mechanical twin twin-related to both transformation twins with plane EFGHIJ the composition plane. The original transformation twins remain related across plane EHDA as with the black regions of Figure 20. No attempt has been made to draw the mechanical twin composition plane in its actual orientation in Figure 20.

hysteresis loop during the first cycle is shown in Figure 22. Twin nucleation was accompanied by an audible "clock" and a yield drop followed by a low modulus serrated region as the twin spikes widened. A high modulus region was observed after the spikes had consumed the specimen midsection. When the compressive stress was removed, the mechanical twin was observed to contract into gradually shrinking spikes that did not completely disappear until tensile stress was applied. As cycling continued, the threshold stress for twinning decreased, the yield drop disappeared, and the loop became more symmetric about zero stress as shown in Figure 23. This loop is similar in form to the corresponding stable loop in single region specimens (Figure 18). The transition to the "stable" loop was complete in 15 cycles.

3. Deformation Where Neither Transformation Twin Boundary Motion nor Mechanical Twinning Is Possible.

Figure 24 shows the stereographic projection of Specimen 61 which, according to the algorithm, should not deform by transformation twin boundary motion (since $\delta \approx \frac{\pi}{2}$) nor by mechanical twinning (because $\gamma \approx \frac{\pi}{2}$ for both mechanical twin planes—Section III, Expression 1). This specimen behaved as predicted. Low modulus segments associated with twin boundary motion are absent in its hysteresis loop in Figure 25, and a high stress (>10 Kg/mm^2) produced only a small strain (<0.01) compared with deformation by twinning in other specimens (Figures 17, 22, and 26).

4. Deformation by Twin Boundary Motion in Orthorhombic Single Crystals

Figure 26 shows the hysteresis loop of an orthorhombic single crys-

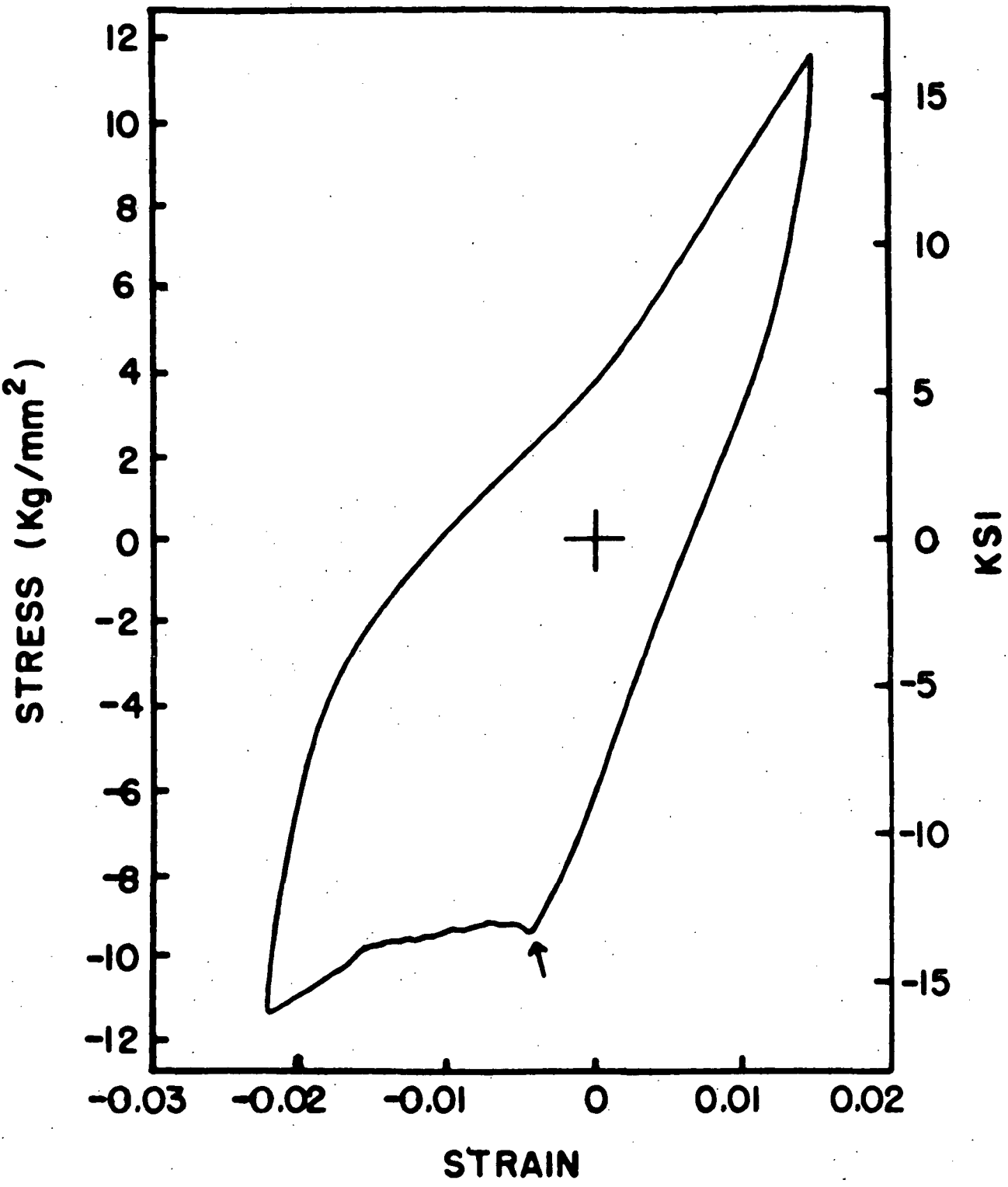

Figure 22. The hysteresis loop of single region Specimen 73 showing mechanical twinning in compression on the first testing cycle. Note the yield drop on twin nucleation as indicated by the arrow.

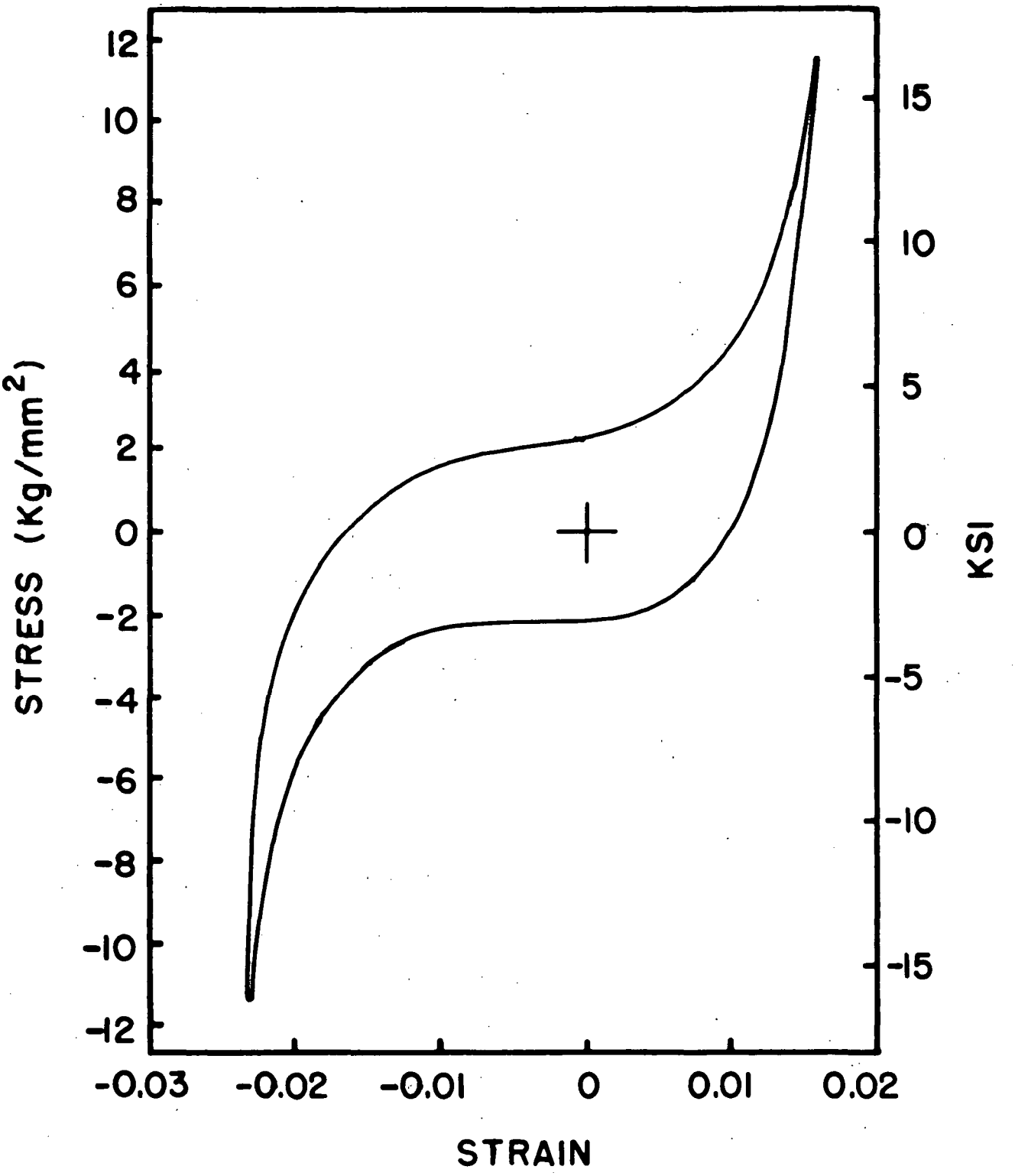

Figure 23. Stable loop of Specimen 73 (cycle 160). Note the absence of the yield drop and the symmetry of the loop about zero stress. (Same scale as Figure 22.)

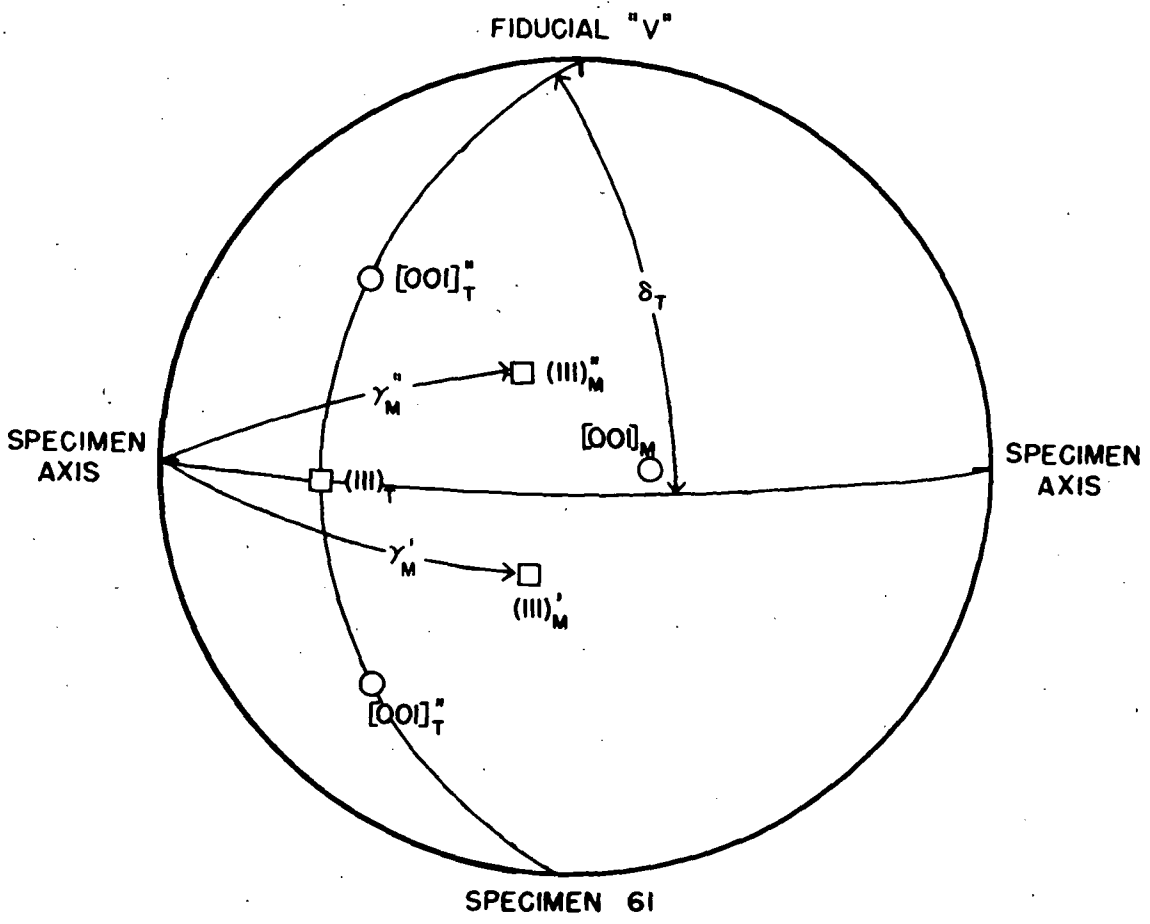

Figure 24. Stereographic projection of Specimen 61. The subscript "T" refers to the transformation twin system which cannot operate because $\delta_T \approx \pi/2$ (Section III, Expression 1). Likewise, mechanical twinning cannot occur because γ'_M and $\gamma''_M \approx \pi/2$ for each mechanical twin plane in the above mentioned expression.

Figure 25. The hysteresis loop of Specimen 61 showing no low modulus segments indicative of twinning at stress levels high relative to those where twin boundary motion is observed. This specimen was subsequently tested under ±19 Kg/mm^2 stress and showed considerably more plastic deformation than is apparent here. Note the expanded strain scale compared with earlier figures.

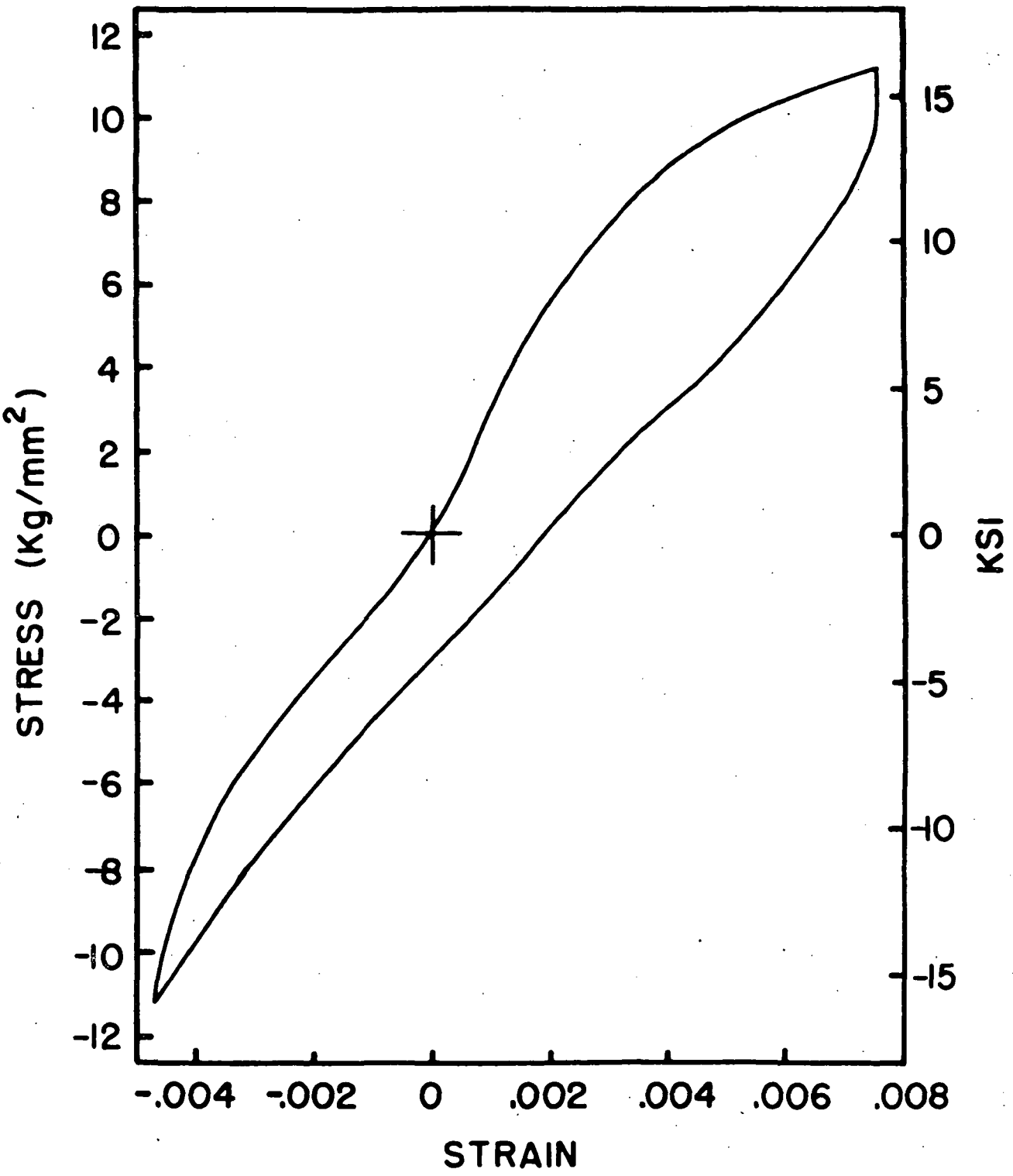
12
10
8
6
4
2
0
-2
-4
-6
-8
-10
-12
STRESS (Kg/mm²)
15
10
5
0
-5
-10
-15
KSI
-.004
-.002
0
.002
.004
.006
.008
STRAIN

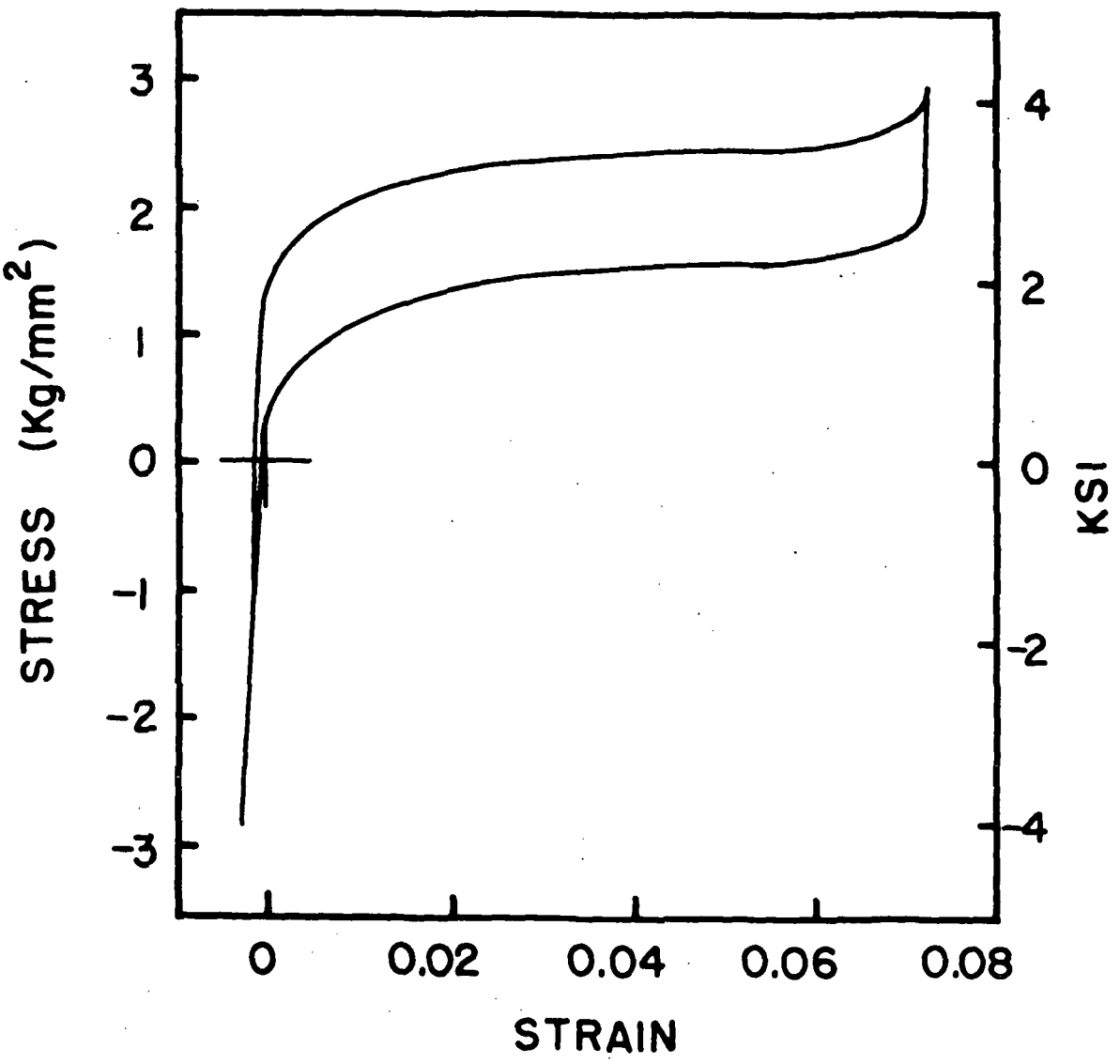

Figure 26. The hysteresis loop of single crystal orthorhombic Specimen 68 early in fatigue life (20 cycles) which was favorably oriented to deform in tension only. The body of the loop lies above zero stress because the specimen was well stabilized (rubber-like). Thus, the restoring force returned the twin boundaries to their original configuration and the specimen to its original shape when the stress was removed. Note the compressed strain scale (and the expanded stress scale) relative to earlier figures to illustrate the 0.072 strain at low stress with this specimen.

tal early in fatigue life which remained essentially unchanged the first 1,000 cycles. The [001] short axis of this stabilized single crystal was only 8 degrees from the longitudinal axis making this orientation favorable only for deformation in tension since there was no more favorable twin related orientation for compression. Hence, the asymmetry of the loop was anticipated. In Section III, it was predicted that any twin system with an [001] axis of one twin near the tension axis should have a large strain amplitude. This specimen could respond to tensile stress by twinning on any of the four possible (111) twin systems, and that which permitted the greatest elongation was observed to operate. The low tensile stress for twin boundary motion (2.1 Kg/mm^2) relative to that for mechanical twinning (10 Kg/mm^2) suggests that twin nuclei may have been present prior to testing although x-ray and microscopic examination showed no evidence of them.

As testing continued, the loop shape in Figure 26 changed to that in Figure 27 which then remained essentially unchanged from 10,000 to 1,005,000 cycles when testing was stopped. This stable loop (Figure 27) was the same form as those for transformation twin boundary motion (Figure 18) and mechanical twinning (Figure 23).

5. Deformation in Multiple Region Specimens

As mentioned in the introduction, it is possible to transform a single crystal parent by several interfaces producing several different twinned lamellar regions all with crystallographically equivalent relations to the cubic single crystal parent[10,11] (Figure 2). Birnbaum and Read reported that twin and region boundaries move in response to stress in such

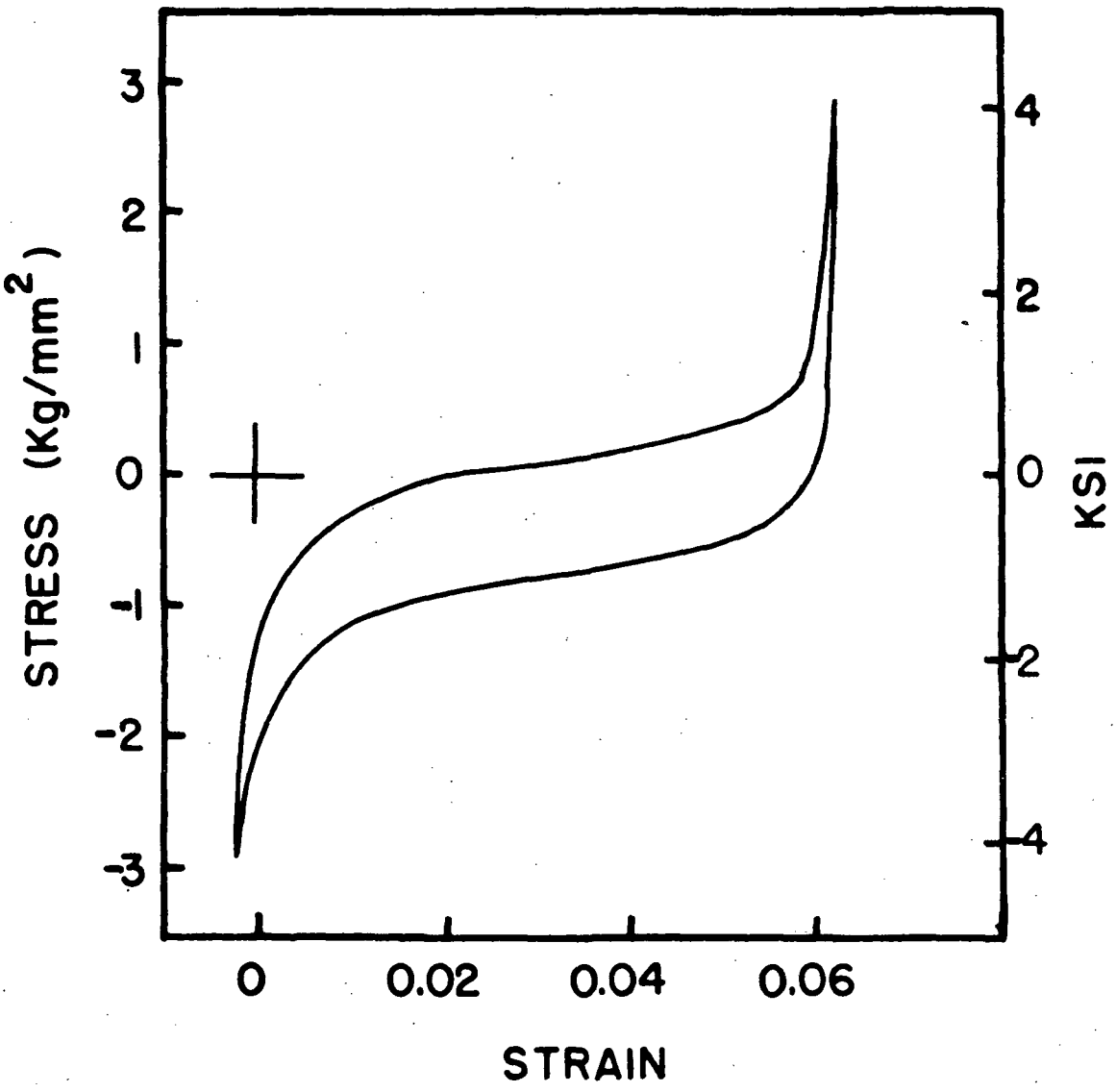

Figure 27. Stable loop of single crystal orthorhombic Specimen 68 (cycle 30,000). Note the shift of the body of the loop downward relative to Figure 26 and thus the relative absence of the ferroelastic restoring force. (Same scale as Figure 26.)

specimens.[12] Of the five multiple region specimens tested, two showed twinning type deformation with typical stable loops and step phenomena while three behaved similarly to a poor single region orientation (Section IV, B, 3).

6. Deformation in Polycrystalline Specimens

Four polycrystalline specimens with approximately 1 mm average grain size were tested to failure in stroke control. Their hysteresis loops showed no indication of deformation by twinning and resembled that of a poor single region orientation (Section IV, B, 3).

7. Rate and Temperature Effects on the Hysteresis Loop

The testing temperature and cycling frequency were found to have significant effects on the shape of the stable hysteresis loop, especially at frequencies below 10^{-1} Hz. Shown in Figure 28 are loop shapes for several frequencies traced at several temperatures. The loop hysteresis generally decreased with increasing frequency and decreasing temperature at frequencies below 7.5×10^{-2} Hz. The loops did not appear to change, however, when viewed on a CRT as the testing frequency was increased from 7.5×10^{-2} Hz to approximately 7.5 Hz at all temperatures. This will be discussed further below (Section V, B).

8. Step Phenomena

The formation of a stress step whenever cycling was stopped for more than a few seconds was a common feature of all "stable" loops of specimens deforming by twin boundary motion described in Section IV, B, 1,

Figure 28. The effect of cycling frequency and temperature on the stable loop shape of Specimen 76. Frequency decreases to the right, and temperature decreases towards the bottom of the page.

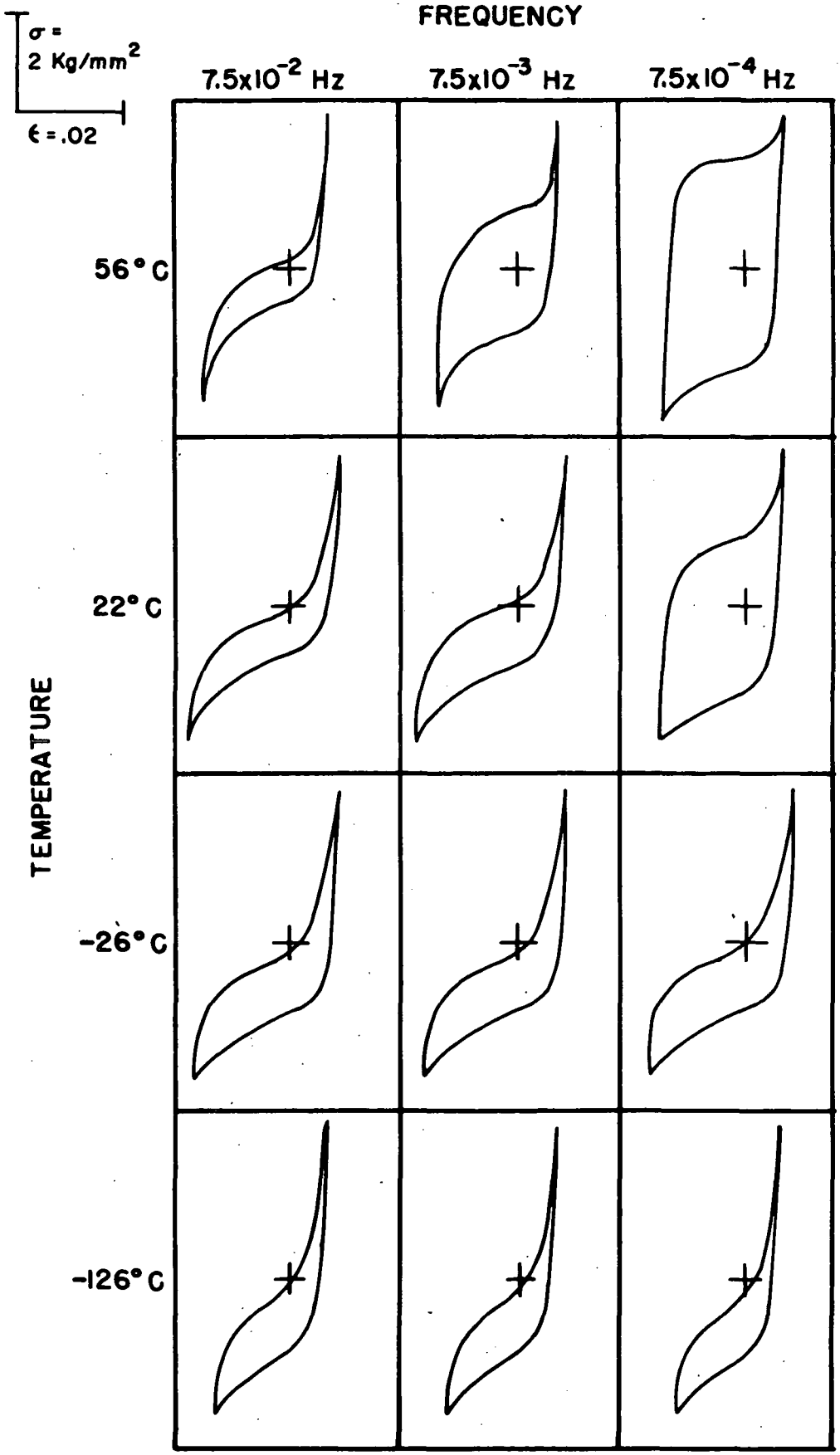
FREQUENCY
σ =
2 Kg/mm²
ε = .02
7.5x10⁻² Hz
7.5x10⁻³ Hz
7.5x10⁻⁴ Hz
56° C
22° C
-26° C
-126° C
TEMPERATURE

2, and 4. Figure 29 shows the effect of a 10 minute holding period at zero load and room temperature on the shape of a stable loop. One side of the loop has been vertically displaced relative to the other, and moduli for twin boundary motion in the vicinity of this step have decreased relative to the stable loop. The step height is defined to be vertical displacement of the center C in the two portions of the loop, i.e., between the two stress midpoints C' and C" of the two half loops in Figure 29. This has been plotted vs holding time at various temperatures in Figure 30 for the specimen illustrated in Figure 29. Steps may be created anywhere in the low modulus region of the loop (i.e., not only at zero stress), and several steps may be introduced into one loop.

When cycling is resumed, the steps shrink and disappear at a rate which depends on frequency. In Figures 31 and 32 are plotted the fraction of the initial step height vs time and number of cycles respectively at several cycling frequencies after a ten minute hold at zero stress. The data for 8.3×10^{-2} Hz is plotted vs cycles on an expanded linear scale in Figure 33 to show that the effect of a single cycle on a "ten minute" step height is a decrease of approximately 2 percent which is small relative to the step measurement error ($\pm$ 4 percent) and negligible relative to the step reproducibility ($\sim \pm$ 20 percent) in one specimen. Hence, the step height growth at various temperatures (Figure 30) observed by tracing single 8.3×10^{-2} Hz loops was plotted not against total elapsed time, but after subtracting the cumulative tracing time (12 sec per loop) from the elapsed time for each point. This procedure will be justified further below (Section V,B).

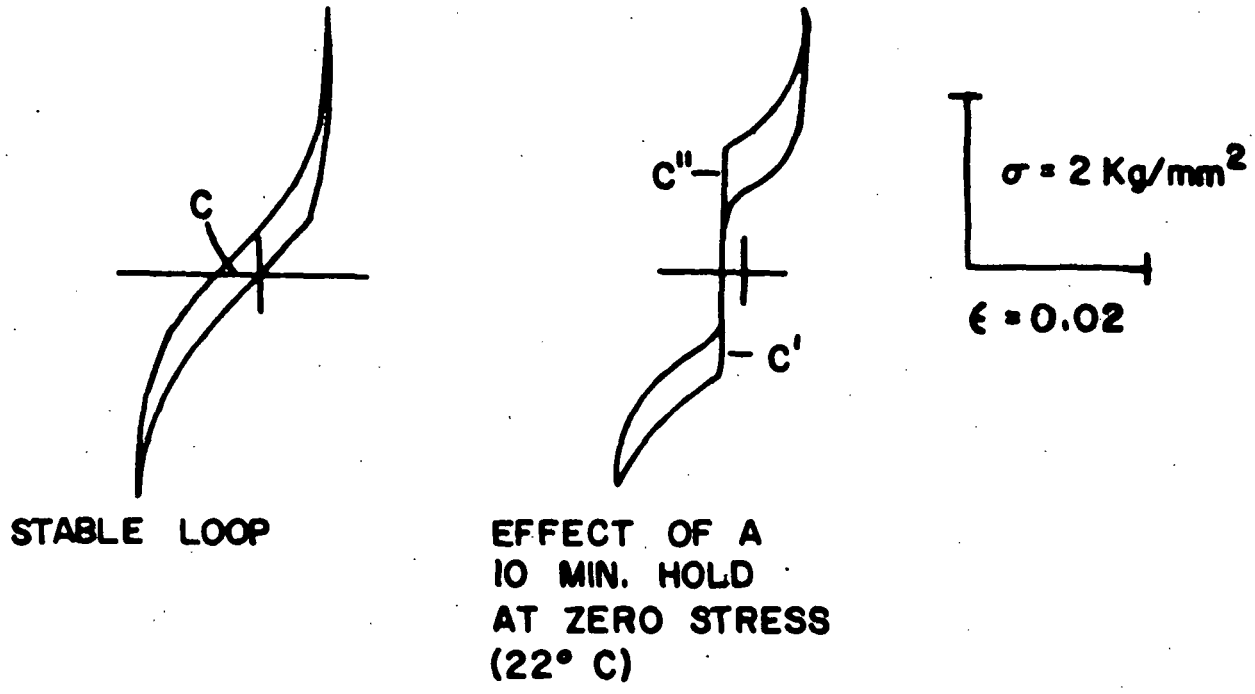

Figure 29. The displacement of the left and right portions of a stable loop caused by a ten minute hold at zero load and room temperature. The step height is defined as the separation displacement of the loop's center C to C' and C". Note that while the modulus of the loop near the holding point has been decreased somewhat by the hold, the stress hysteresis (vertical width) is virtually unchanged.

Figure 30. The growth of a step (C' - C" of Figure 29) with holding time at several temperatures for Specimen 76. The time axis is the total hold time (the total elapse time minus the time required to trace the loops); see text.

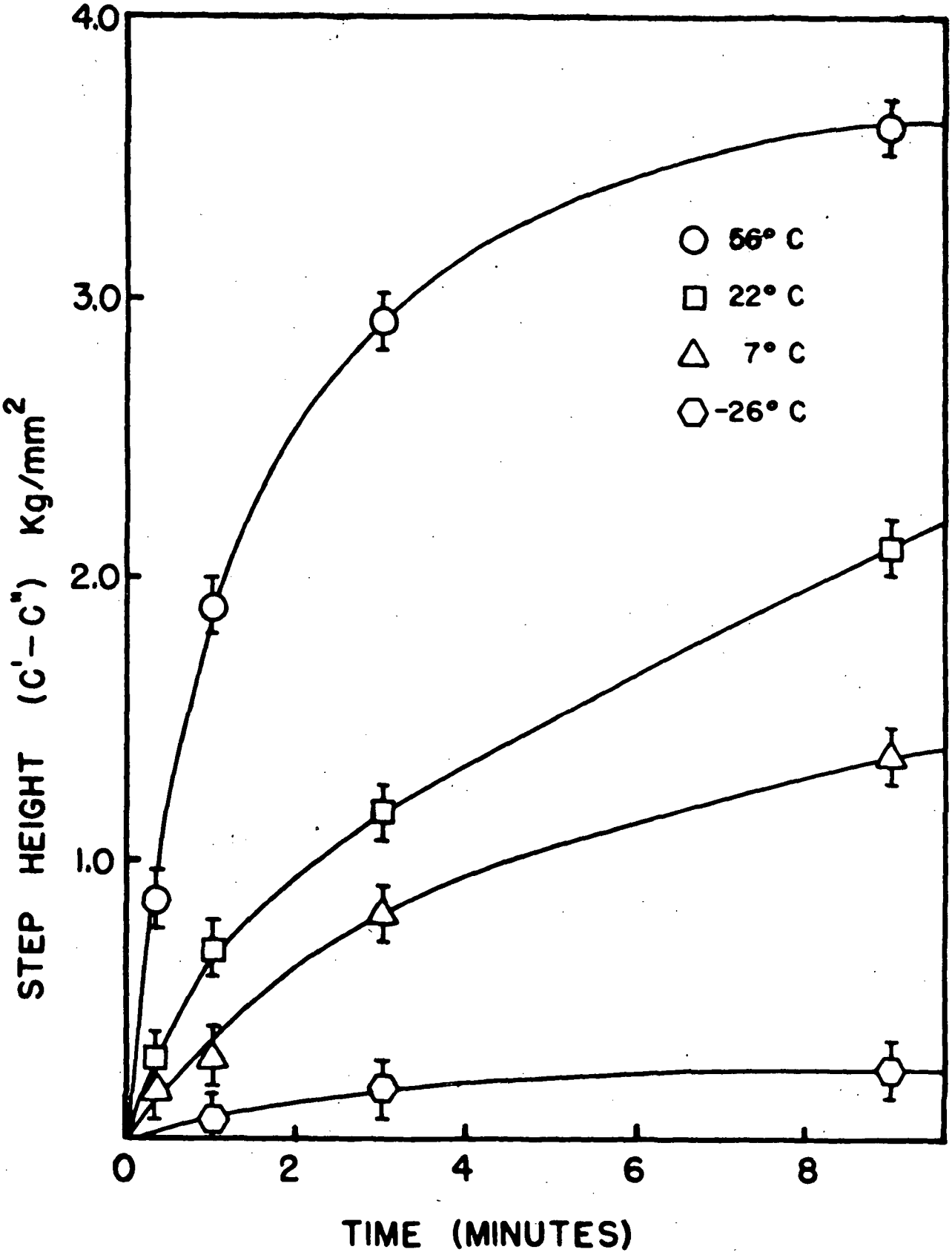
4.0
3.0
2.0
1.0
0
2
4
6
8
STEP HEIGHT (C'-C") Kg/mm²
TIME (MINUTES)
56° C
22° C
7° C
-26° C

Figure 31. The disappearance of a stress step (formed by a ten minute hold on a stable loop at room temperature) when cycling is resumed vs time for several frequencies for Specimen 56. Note that the rate of disappearance increases with increasing frequency.

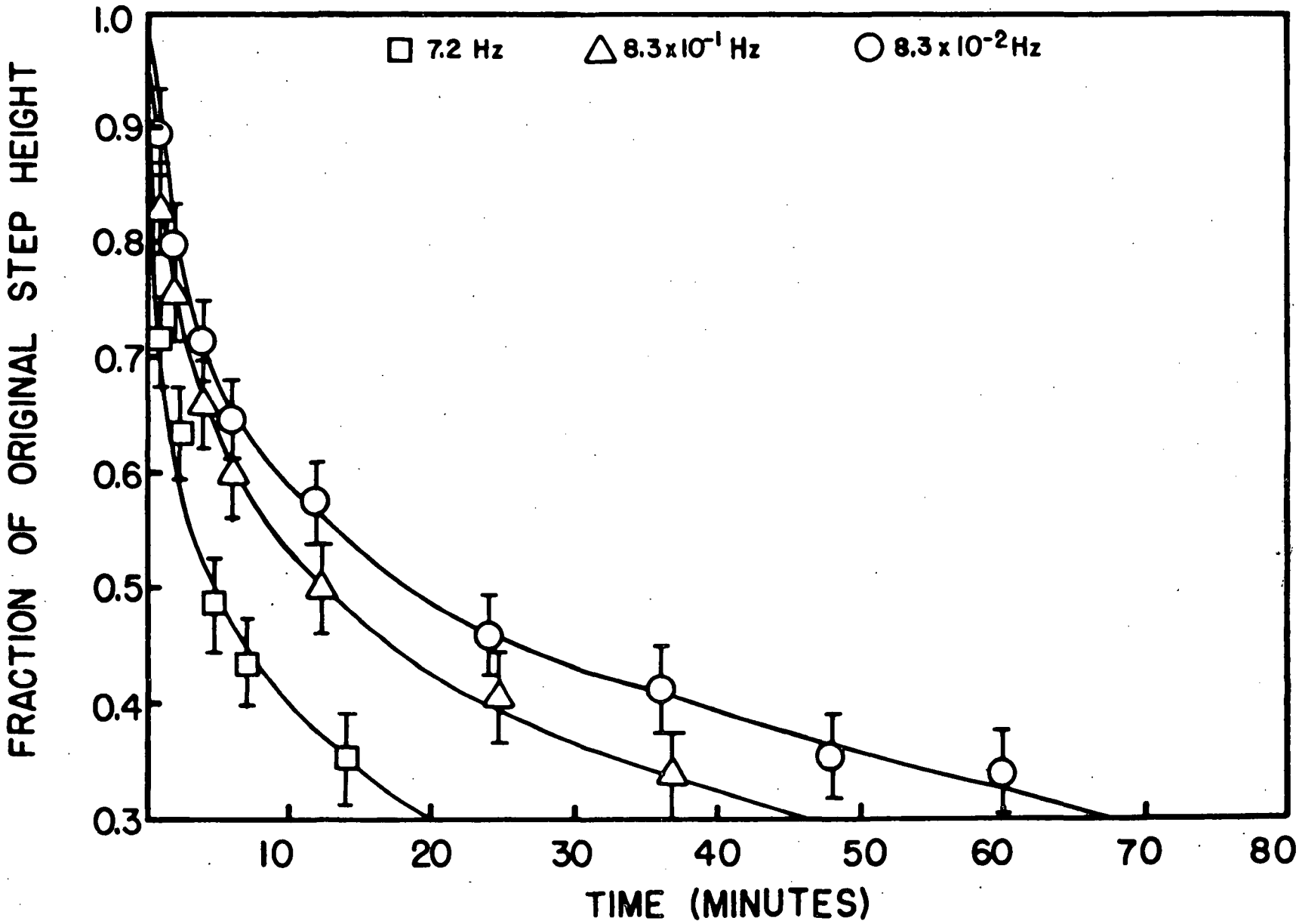
□ 7.2 Hz
△ 8.3x10⁻¹ Hz
○ 8.3 x 10⁻² Hz
FRACTION OF ORIGINAL STEP HEIGHT
1.0
0.9
0.8
0.7
0.6
0.5
0.4
0.3
10
20
30
40
50
60
70
80
TIME (MINUTES)

Figure 32. The same data as in Figure 31 vs the number of cycles showing that the fraction of the step height lost per cycle decreases with increasing frequency.

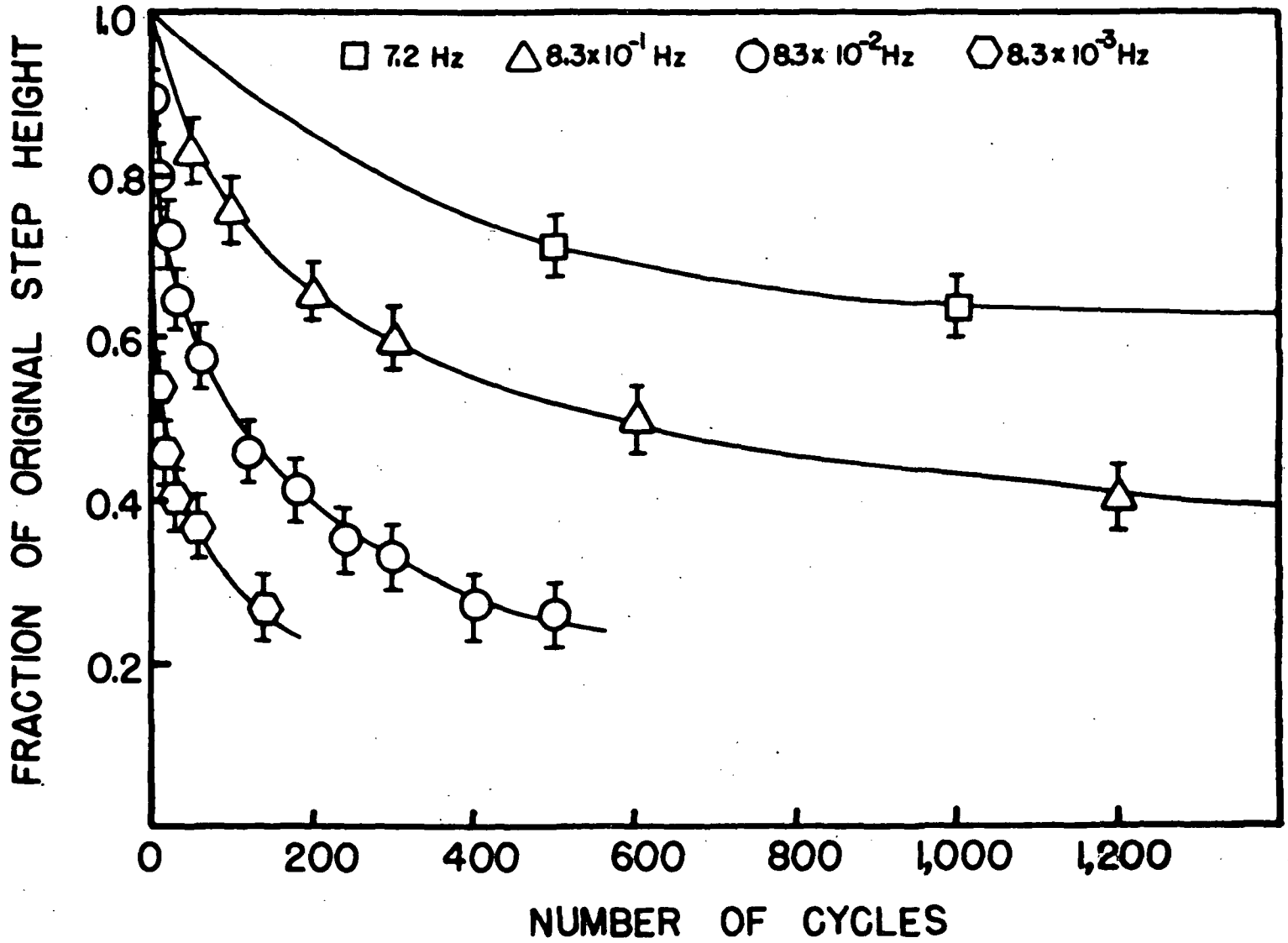
FRACTION OF ORIGINAL STEP HEIGHT
1.0
0.8
0.6
0.4
0.2
0
200
400
600
800
1,000
1,200
NUMBER OF CYCLES
7.2 Hz
8.3x10⁻¹ Hz
8.3x10⁻² Hz
8.3x10⁻³ Hz

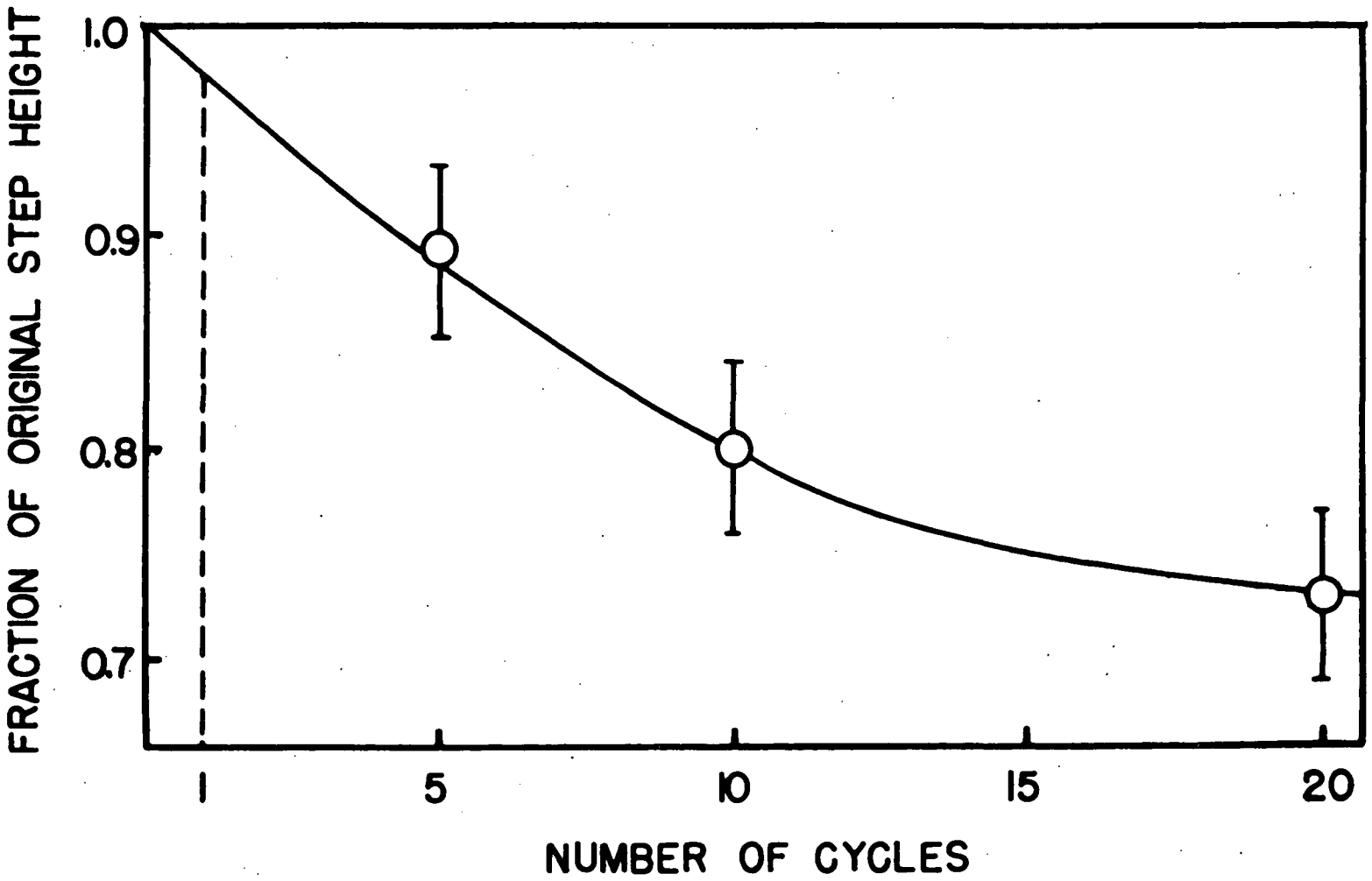

Figure 33. An expanded view of the 8.3×10^{-2} Hz data showing that the effect of a single loop tracing on a "ten minute" stress step is ~2% reduction in step height.

All the above step height observations were made while specimens remained mounted in the testing machine. This was found to influence the step shape as illustrated in Figure 34 which compares an "in machine" step to an "unconstrained" step obtained by releasing the specimen from the upper grip during the hold. The machine appears to effect the phenomenon by raising the step modulus and decreasing its strain hysteresis. An "in machine" step was changed to an "unconstrained" step after an additional ten minute hold with the upper grip released. Difficulty in removing and re-attaching the upper grip, particularly at nonambient temperatures, limited the study of the "unconstrained" step phenomena and hence the quantitative information which could be obtained from these studies.

C. Fatigue Properties

1. Torsion Fatigue Data

Torsion fatigue data were obtained on a Satec SF-2U constant force machine. Figure 3 shows a typical torsion specimen. The strain estimation calculations are outlined in Appendix C. All specimens were single region, but were not oriented prior to testing. Type 302 stainless steel specimens (Figure 35) were tested for comparison with the AuCd specimens. The results are shown in Figure 36 as a conventional log strain ($\Delta\varepsilon$) vs log cycles to failure diagram. However, the inhomogeneity inherent in torsion fatigue and the inflexibility of the Satec machine made it difficult to examine such factors as rate and orientation dependence. Therefore, the major effort was expended in tension-compression testing.

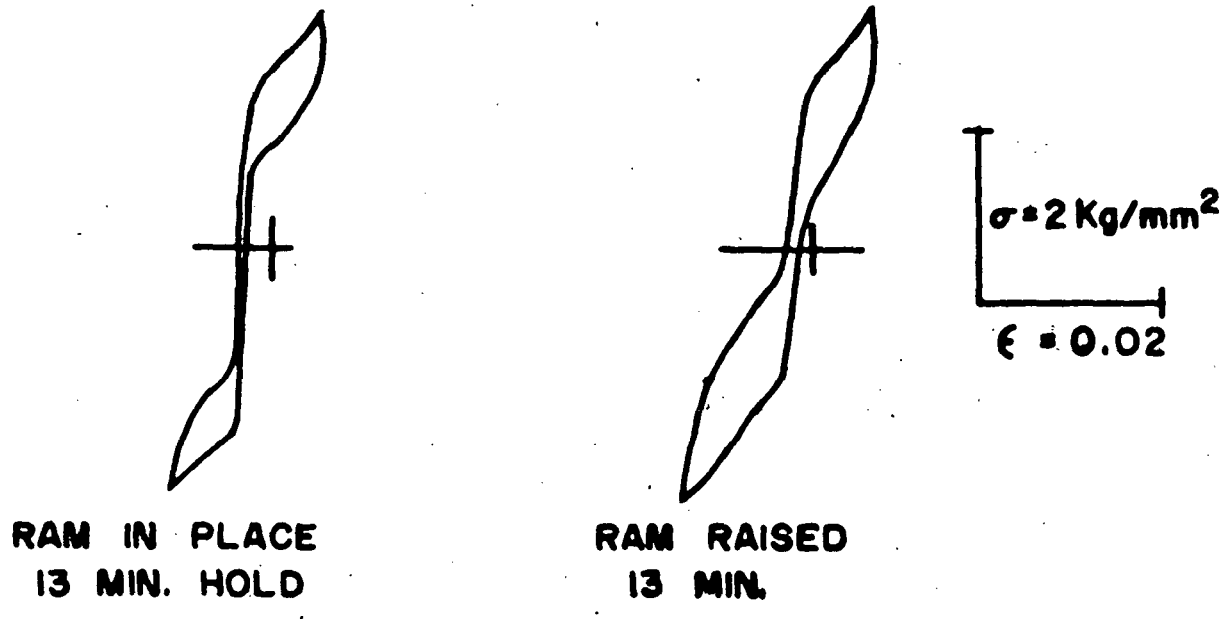

Figure 34. The difference between stress steps resulting from a hold when the specimen is constrained by the machine and when the upper grip is released. The machine appears to cause a narrower stress hysteresis and a larger step height.

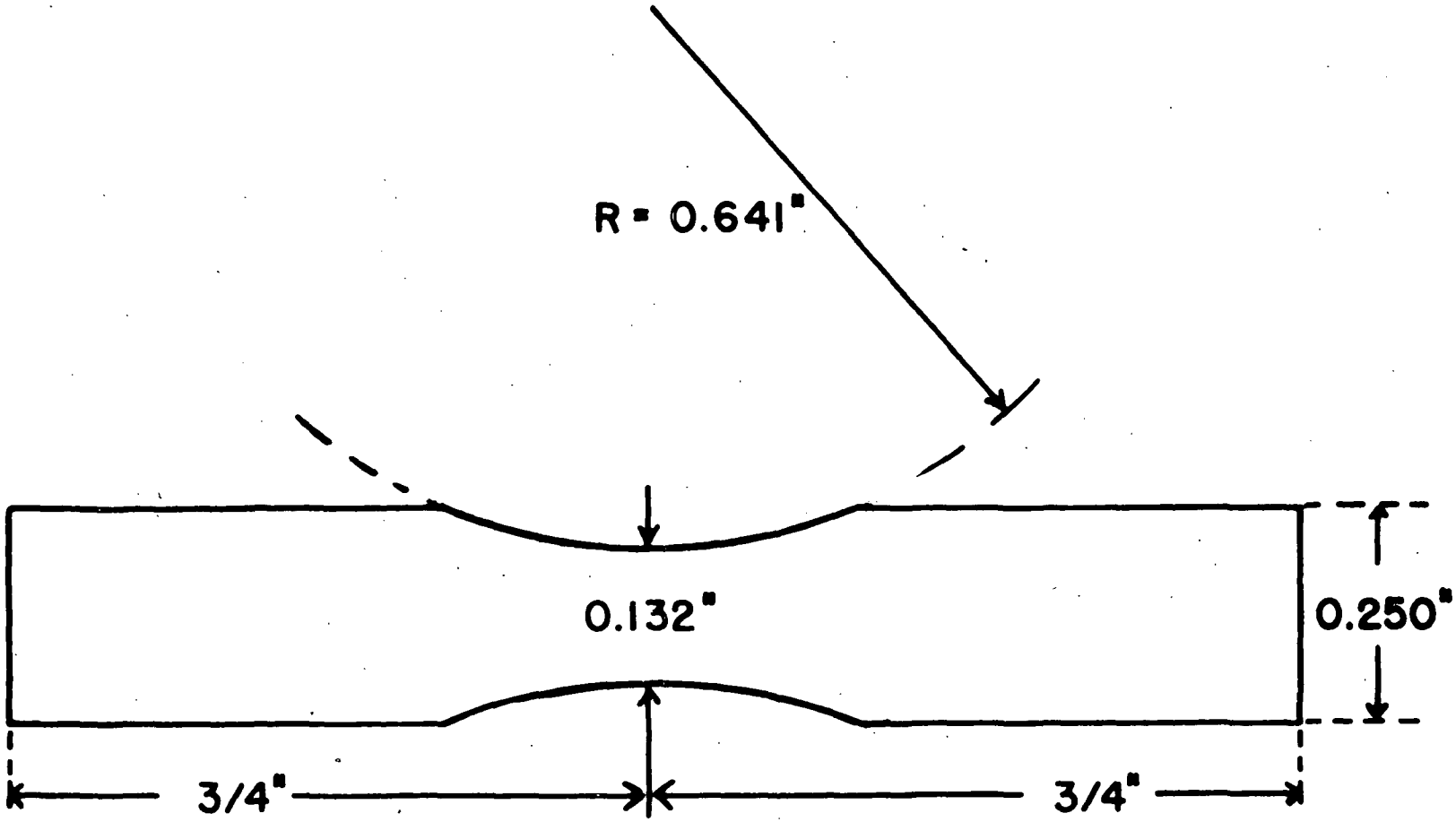

Figure 35. The dimensions of the type 302 stainless steel cylindrical specimens prepared for comparison to the AuCd torsion fatigue data.

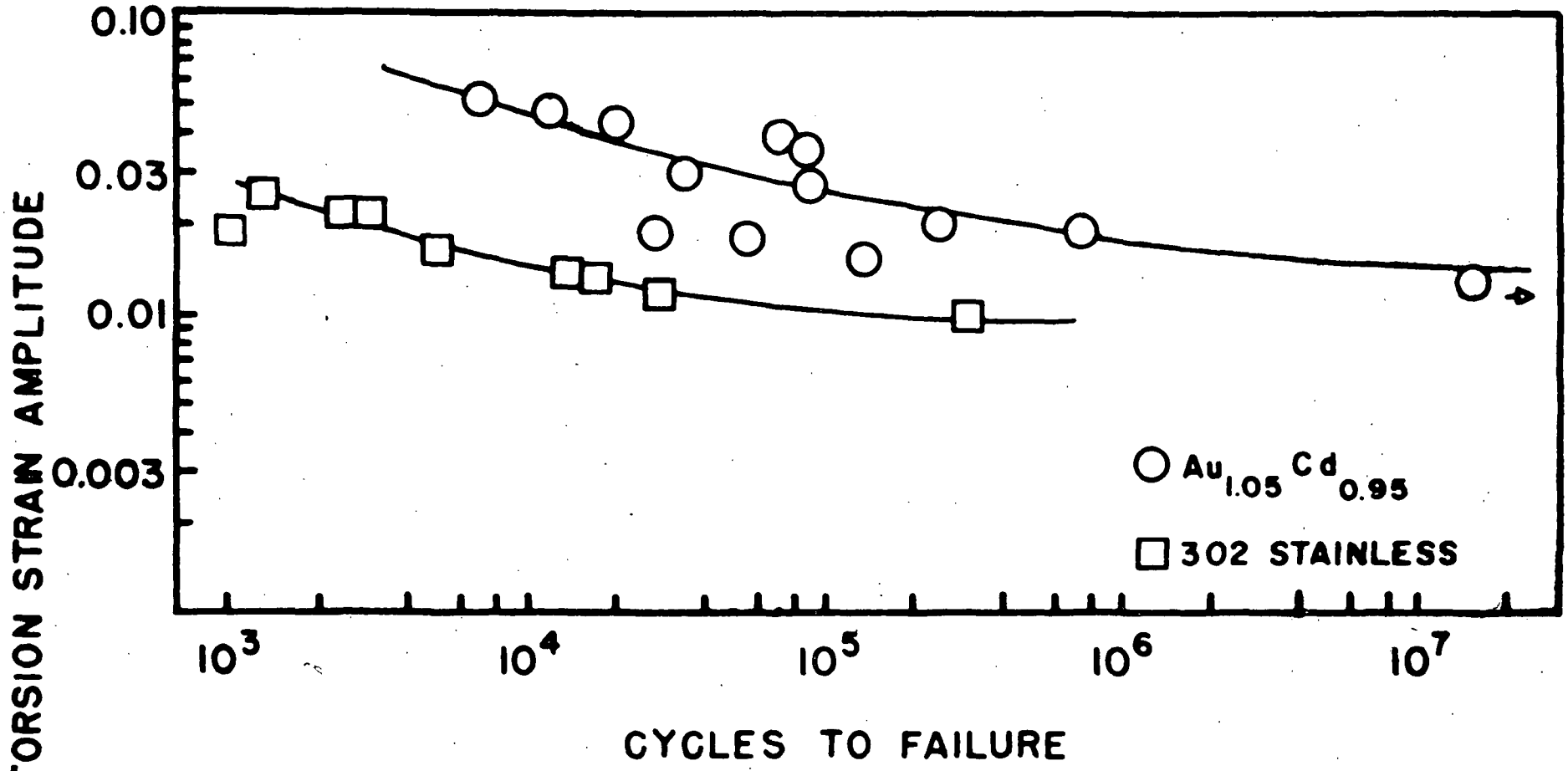

Figure 36. Torsion fatigue data plotted as log strain vs log number of cycles to failure. The strain values given are total strain, $\Delta\varepsilon$. The data demonstrate the strain fatigue resistance of AuCd single region specimens compared with a fatigue resistant steel.

2. Tension-Compression Fatigue Data

Tension-compression fatigue testing was performed on several single region and polycrystalline specimens. The results and relevant data on each specimen are tabulated in Appendix B. The testing procedure is described in Section II, and most specimens were cycled in load control for reasons outlined there. Therefore, the strain amplitude, being an uncontrolled variable, could vary during testing but was observed to hold relatively constant in most cases. The variation in the uncontrolled variable (stress or strain - here strain is considered a controlled variable in stroke control) for each specimen is listed in Appendix B, and the half-life value is used to characterize the specimen's behavior. The β' AuCd fatigue behavior is summarized in Figure 37 as log total strain amplitude ($\Delta\varepsilon$) vs log cycles to failure* and in Figure 38 as log stress vs log cycles to failure (Figure 32). While little change in the "stable" loop shapes were observed during testing** (Sections IV, B, 1, 2, and 4), removal of specimens from the machine well into testing (>100,000 cycles) for periods of hours was found to significantly influence mechanical behavior. Figure 39 shows this effect for two single region specimens

---

* "strain amplitude" in this paper is defined as $\Delta\varepsilon$ to avoid possible confusion between the algorithmic strain predictions which are always $\Delta\varepsilon$ and the conventional usage of strain amplitude, $\frac{\Delta\varepsilon}{2}$.

** There was no measurable change in the stress hysteresis of any stable loop, and the strain amplitudes and modulii generally varied no more than 10% so long as cycling was not stopped or slowed below 10^{-2} Hz.

Figure 37. Tension-compression fatigue data plotted as log total strain amplitude ($\Delta\varepsilon$) vs log cycles to failure. No line has been drawn through the data because of the scatter. Similar data on an 18% Ni maraging steel are furnished for comparison to a strain fatigue resistant steel. The values plotted are the half-life strains. An arrow indicates no failure.

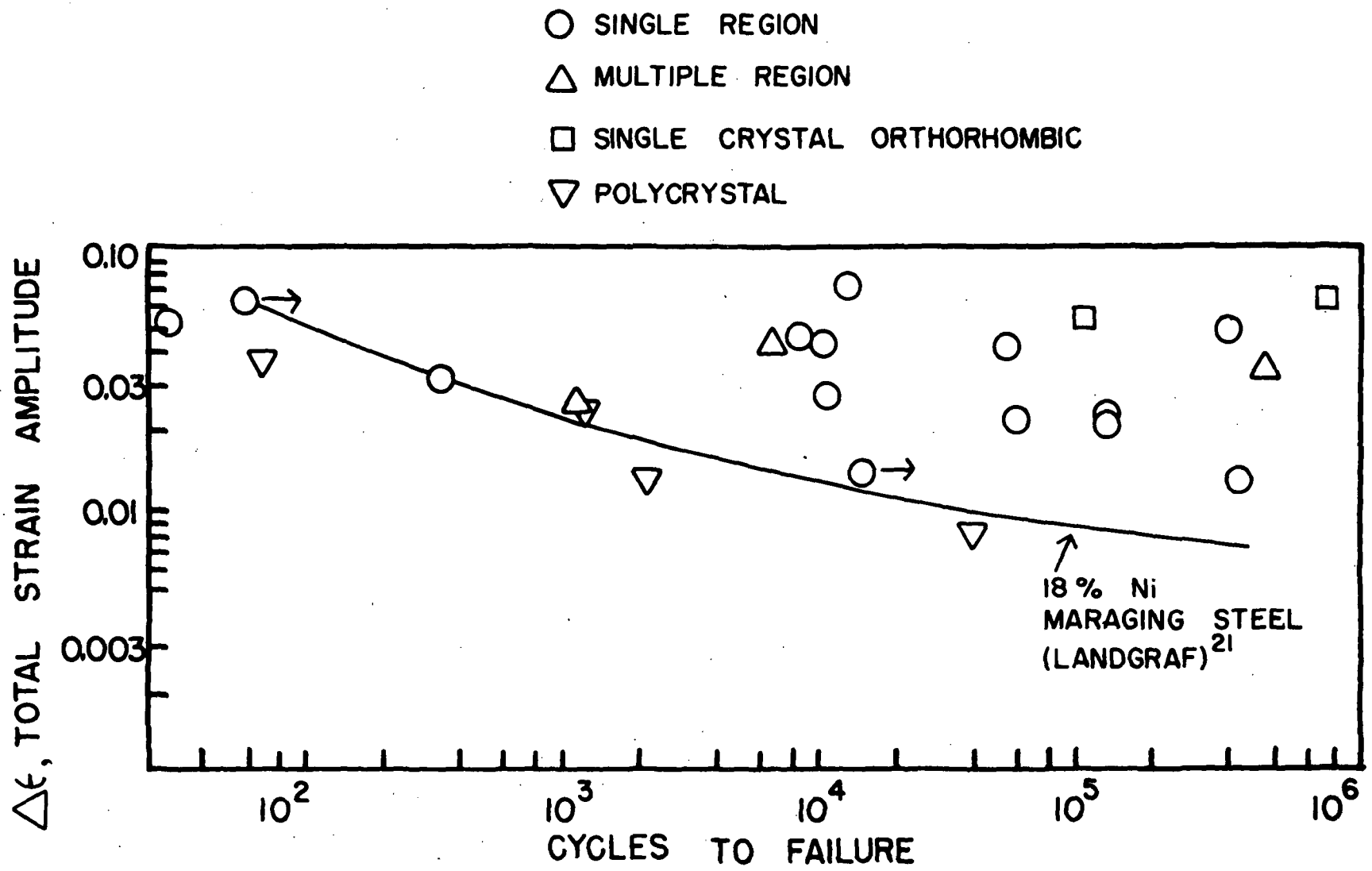
SINGLE REGION
MULTIPLE REGION
SINGLE CRYSTAL ORTHORHOMBIC
POLYCRYSTAL
0.10
0.03
0.01
0.003
Δε, TOTAL STRAIN AMPLITUDE
18 % Ni
MARAGING STEEL
(LANDGRAF)21
10^2
10^3
10^4
10^5
10^6
CYCLES TO FAILURE

Figure 38. Tension-compression fatigue data of stress vs number of reversals to failure on a log log scale. AuCd follows Basquin's stress relation regardless of orientation. The stresses given are half life values, and an arrow indicates no failure.

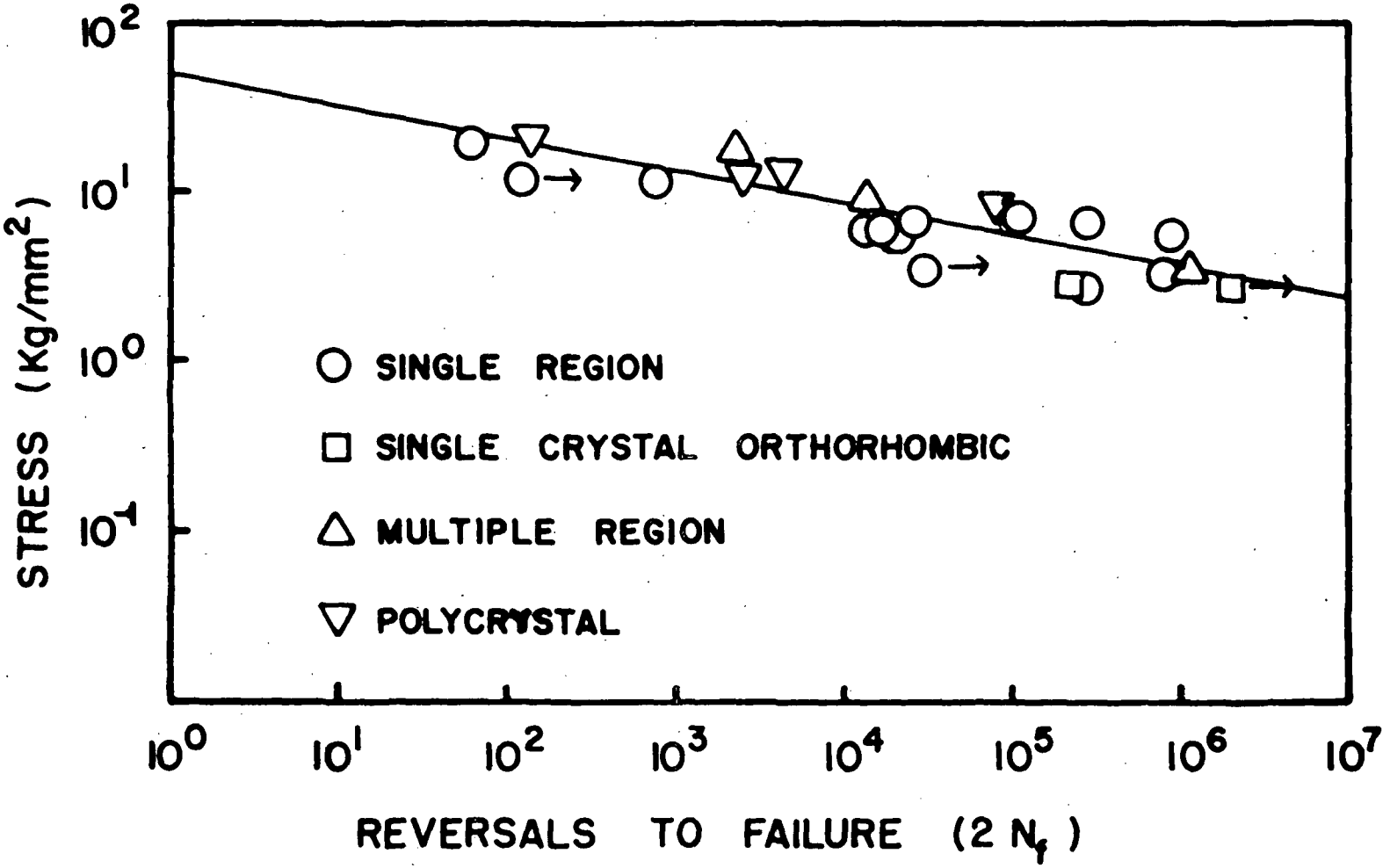
STRESS (Kg/mm²)
10²
10¹
10⁰
10⁻¹
SINGLE REGION
SINGLE CRYSTAL ORTHORHOMBIC
MULTIPLE REGION
POLYCRYSTAL
10⁰
10¹
10²
10³
10⁴
10⁵
10⁶
10⁷
REVERSALS TO FAILURE (2 Nf)

Figure 39. The "hardening" effect shown in load control as a decrease in the strain amplitude and in stroke control as an increase in peak load after a 12 hour testing interruption at room temperature late in fatigue life. The step in the 400,000 cycle loop of Specimen 62 was caused by stopping the machine (Section IV, B, 8).

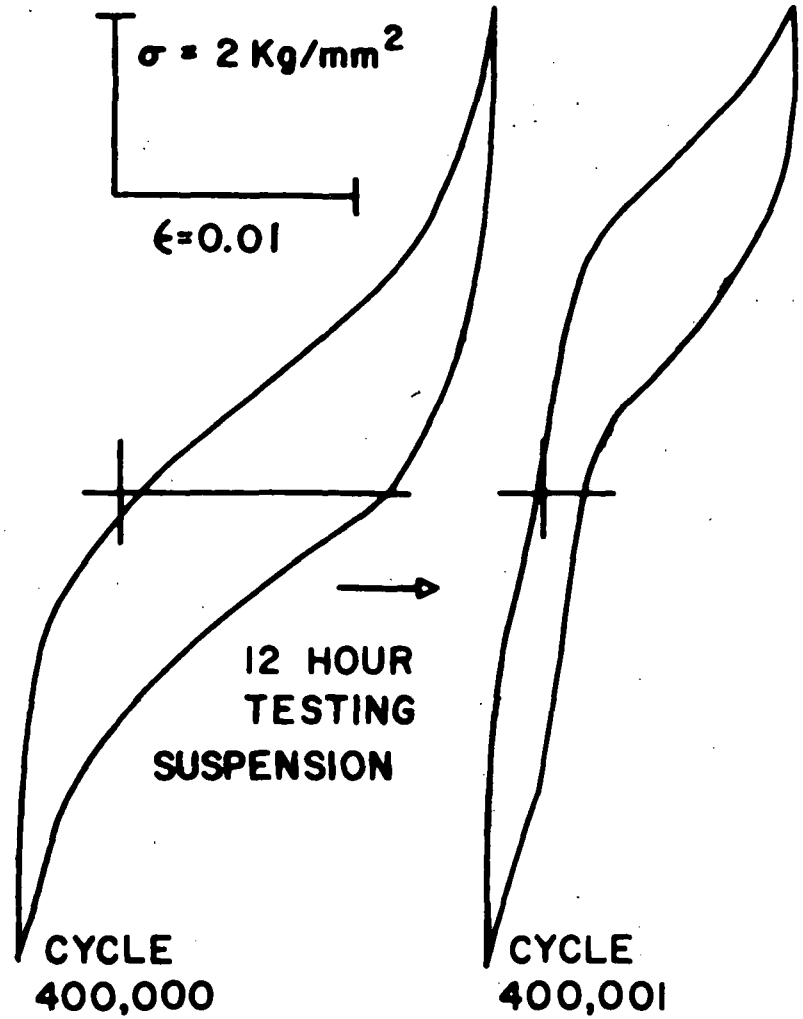

SPECIMEN 70

(LOAD CONTROL)

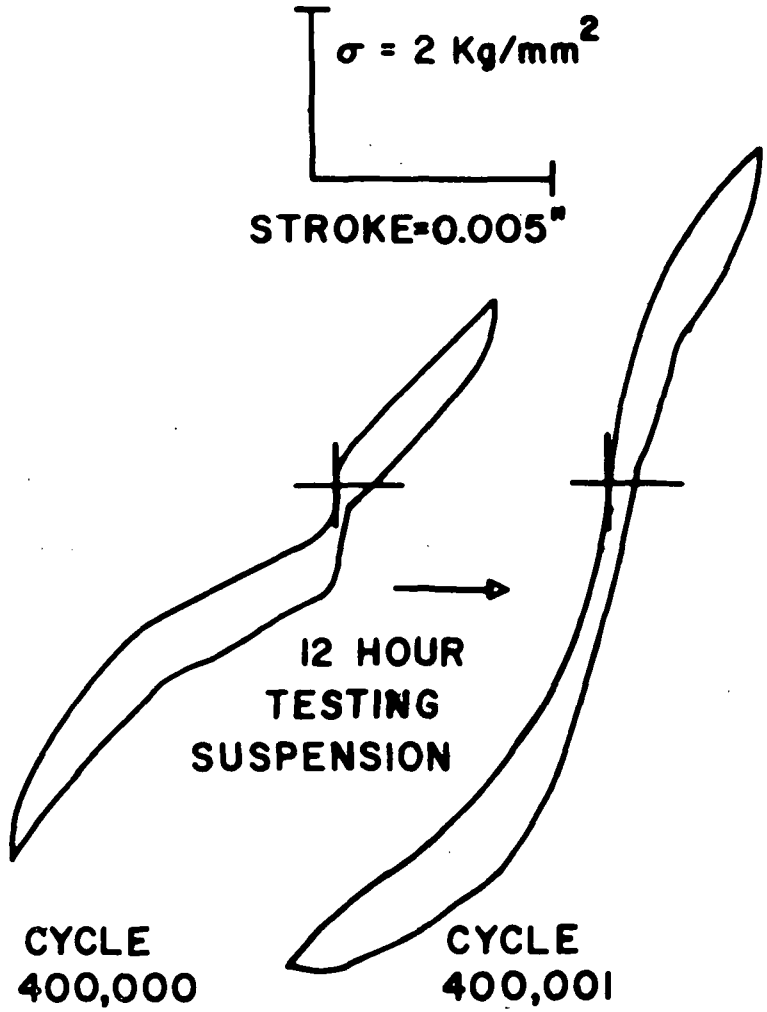

SPECIMEN 62

(STROKE CONTROL)

tested 400,000 cycles and held for 12 hours at room temperature. Specimen 62 was tested in stroke (ram displacement) control, and the interruption raised the maximum stress (the uncontrolled variable) from 3.3 Kg/mm^2 to 4.8 Kg/mm^2. Specimen 70 was tested in load control with the delay lowering the strain amplitude from 0.0160 to 0.0104. This phenomenon will be called the "hardening effect" and apparently is permanent since there was no return to the former loop shape with continued testing.

Specimen 73 was tested 118,000 cycles and stored 66 hours at -190 degrees centigrade to determine whether specimens kept at low temperature would exhibit the effect. Figure 40 shows the final hysteresis loop before the delay and the initial 10,000th and 18,003rd loops after the delay. A stress step (Section IV, B, 8) formed during the testing suspension which disappeared over the subsequent 10,000 cycles leaving a hysteresis loop virtually identical to that before the hold. However, 41 minutes of subsequent room temperature holds reduced the stroke amplitude (an uncontrolled variable) from 0.0138 inches to 0.0065 inches. These data will be further discussed in Section V, C.

D. Fractography

Figure 41 shows several scanning electron micrographs of fracture surfaces on AuCd specimens. They all exhibit characteristics of brittle failure typical of ordered alloys tested well below their melting points; the tests reported here were conducted below 56°C while AuCd melts at ~680°C.

Characteristics of catastrophic failure were commonly observed as shown in the micrograph of Specimen 62. The rivermarks traversing the

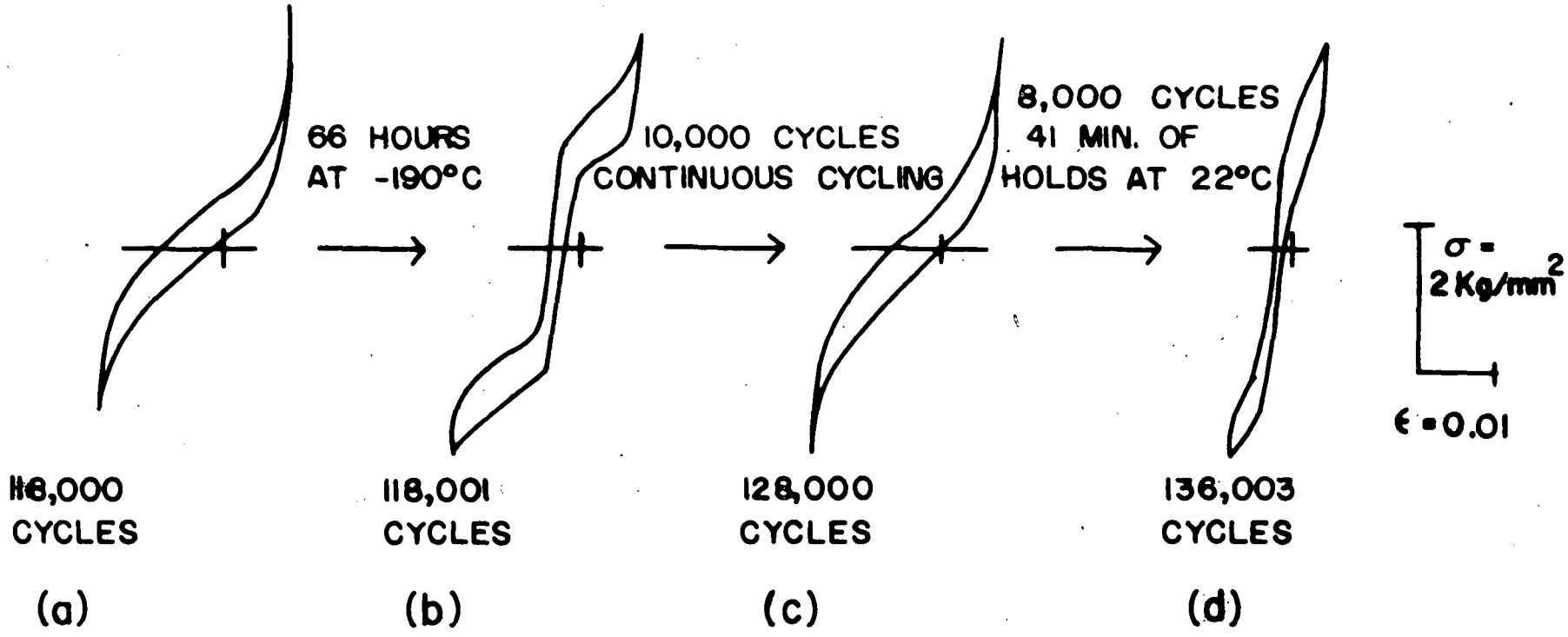

Figure 40. The prevention of hardening by storage at -190°C. Specimen 76, exhibiting a stable loop (a) after 118,000 cycles of testing, was stored 66 hours at -190°C and remounted in the testing machine. (b) shows that a stress step formed during the interruption which disappeared over 10,000 cycles, leaving the loop (c) virtually unchanged from loop (a) before the hold. However, 41 minutes of holds at room temperature caused hardening (d).

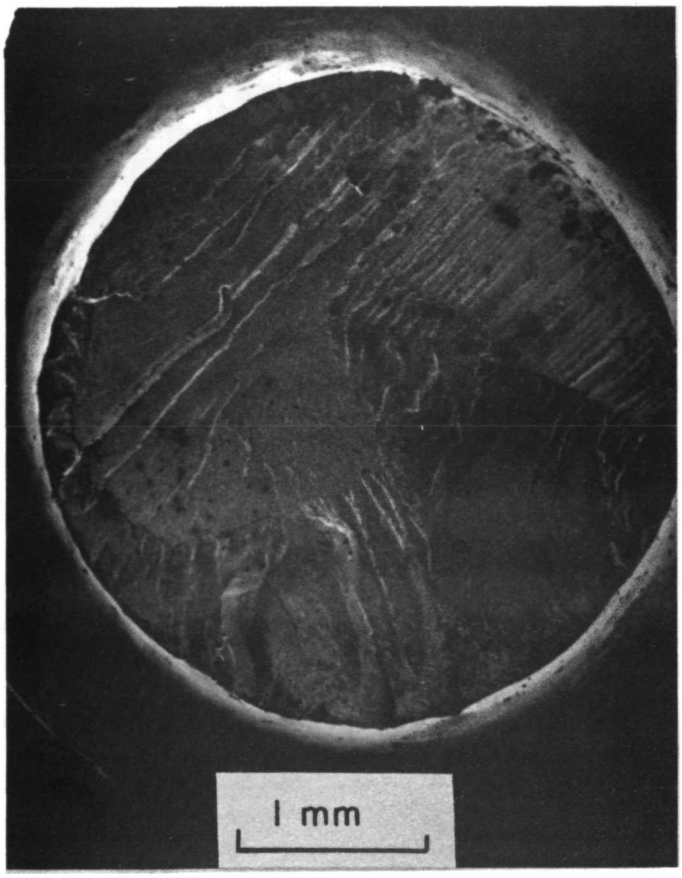

Figure 41(a). The fracture surface on Specimen 62 showing rivermarks characteristic of brittle fracture apparently originating at the upper right.

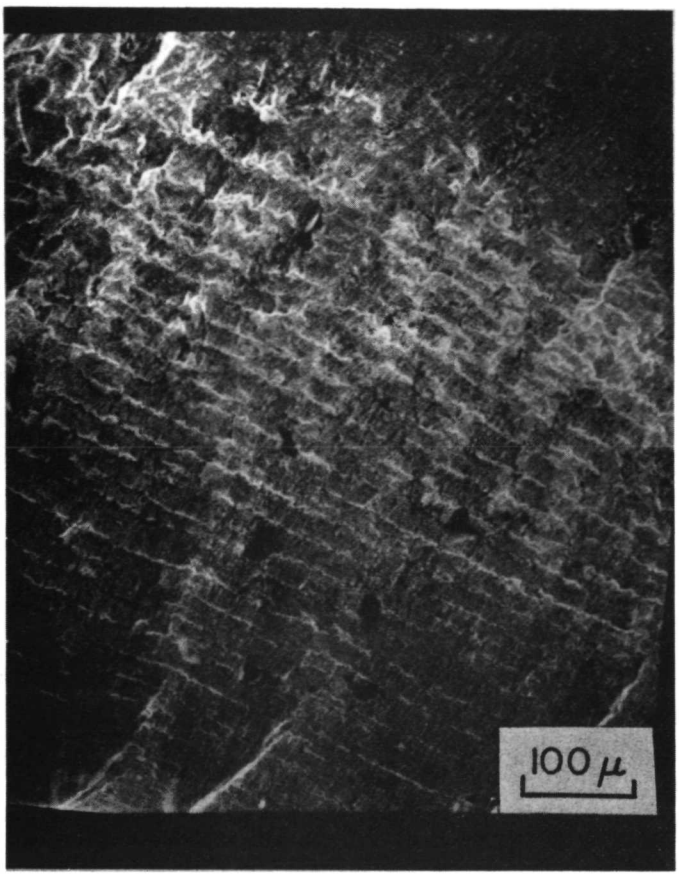

Figure 41(b). The fracture surface of Specimen 53 showing crack front striations. Note the shallow relief and sharp definition characteristic of brittle fracture.

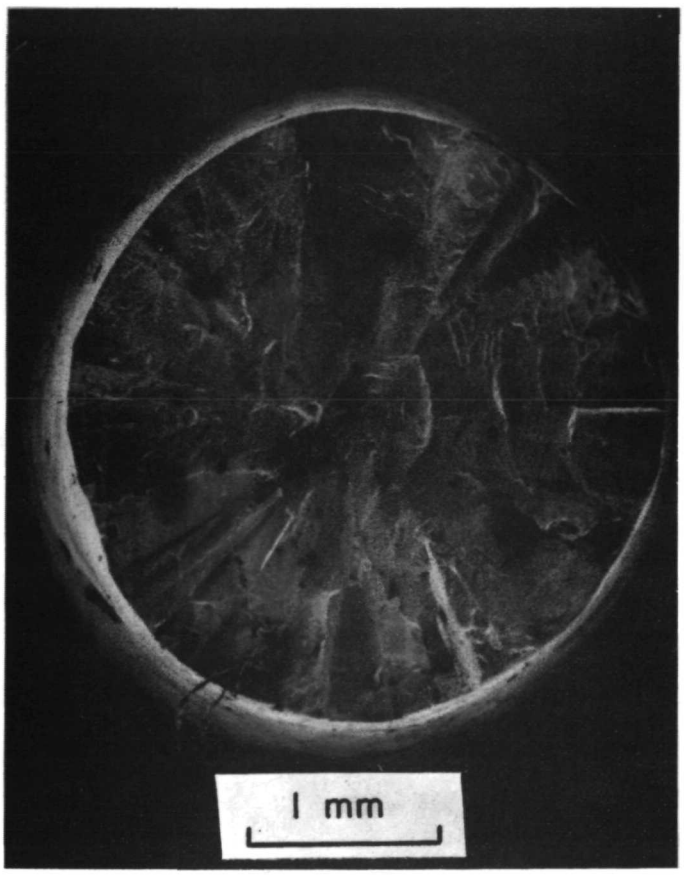

Figure 41(c). The fracture surface of polycrystalline Specimen 63 showing brittle fracture and radial grain structure.

specimen indicate a crack nucleated in the upper right part of the specimen and spread rapidly across it.

Crack front striations marking the progress of the crack on successive cycles were occasionally observed near the nucleation point. They also show brittle characteristics in their sharp definition and shallow relief. Specimen 53 illustrates these striations.

Specimen 63 illustrates a polycrystalline fracture surface. Again catastrophic failure was observed. The radial pattern is apparently due to the radial grain structure resulting from a water quench.

An early stage in crack propagation can be seen in the optical micrographs of the surface of Specimen 72 (Figure 42). This specimen was removed from the testing machine before fracture, and it demonstrates that the cracks can grow parallel to twin boundaries. The second micrograph shows the tip of a satellite crack near the main one.

Figure 42(a). A crack parallel to the twin planes in Specimen 72.

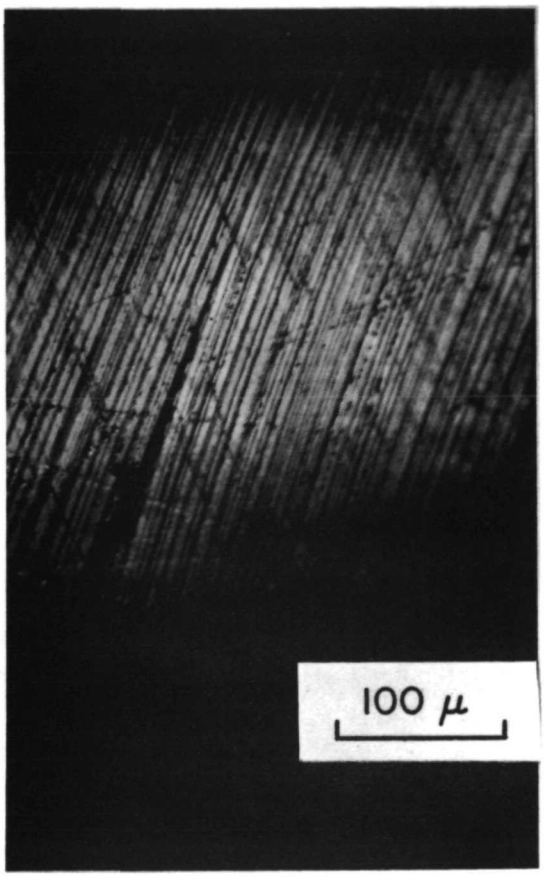

Figure 42(b). A satellite crack parallel to the main crack and ~200 μ from it.

V. FURTHER DISCUSSION

A. The Effect of Orientation on the Degree of Twin Conversion

Figure 14 shows that for longitudinal strain amplitudes above 0.045, the strain amplitude predicted by the algorithm and that measured agree to within 6%. However, for predicted longitudinal strain amplitudes below 0.030, no deformation by twin boundary motion on the predicted twin system is actually observed. Plotting the same form of the data in Figure 15 against the fraction of the stress resolved as shear on the twin plane in the twinning direction (Figure 15) and noting that the data correlate similarly in Figures 14 and 15 permits this to be understood. Since the twin plane normal and the twinning shear vector (also) define the orientation of the twin system and could, equivalently, be used as inputs to the strain prediction algorithm, this correlation is not unexpected. However, the reasons no strain is observed for predicted values below 0.030 in Figure 14 are best understood by investigating why no twin boundary motion is observed when the fraction of the applied stress resolved for twinning is less than 0.13 in Figure 15. This is because the fraction of the applied stress resolved on the twin system has a more obvious physical significance than the algorithmic prediction.

Deformation in β' AuCd can proceed by the competing processes of {100} <100> slip[22]* and twinning, the former being relatively orientation insensitive compared with the latter owing to the multiplicity of slip

---

* The slip system is given here in the orthorhombic system. It comes by lattice correspondence[10,11] from the {110} <100> in the parent β CsCℓ structure.

systems. However slip, once begun, will prevent twin boundary motion by raising the concentrations of slip dislocations and order faults and thus raising the resolved stress necessary to initiate twin boundary motion. For unfavorably oriented specimens, the tensile stress necessary for slip is reached before the shear stress necessary for twin boundary motion. Thus, the data from Figure 15 show that below a resolved twinning stress to tensile stress ratio of 0.130 (corresponding to a predicted strain of ~0.03 in Figure 14), no strain by twin boundary motion will be observed.

However, the above explanation does not adequately account for the data in Figure 14 for predicted strains between 0.030 and 0.045 since these specimens exhibit partial twin conversion, and the resolved stress criterion gives no indication as to why twin boundary motion, once started, should stop before complete twin conversion. There appears to be at least three distinct mechanisms that could limit twin boundary motion; their applicability to each specimen will be considered. Specimen 59 exhibited half the expected stress-strain hysteresis loop, showing twin boundary motion in tension but not in compression (Figure 43), and the strain amplitude is only ~0.4 of that expected. The twin plane orientation was nearly ideal for the resolved stress criterion, being 50° from the specimen axis, but the twinning shear vector was 68° from this axis. This behavior suggests that tension assists twinning shear by separating atom planes parallel to the twin plane while compression hinders this shear by forcing the planes closer together. Support for this hypothesis is found in the stress threshold values for twin boundary motion in the five specimens exhibiting it under both tensile and compressive stress. These data appear in Table 1 which show that, except

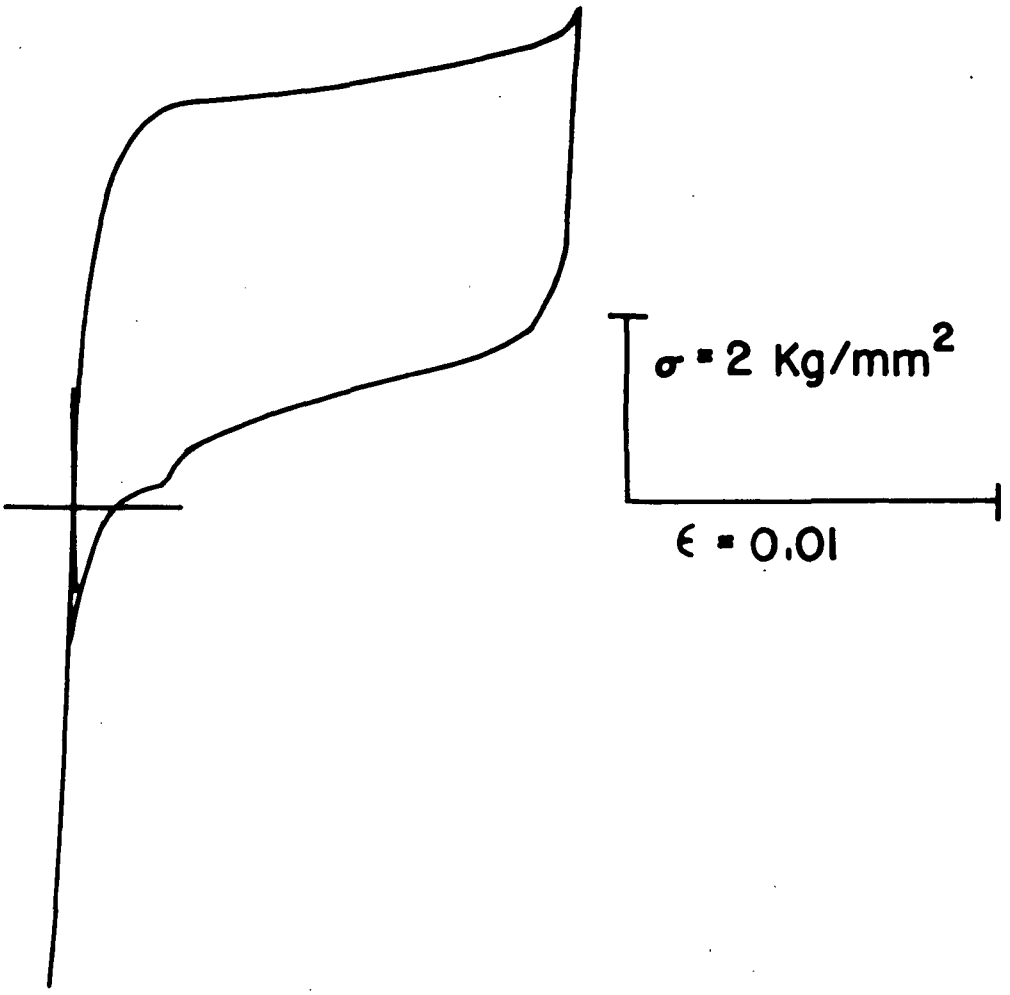

Figure 43. The hysteresis loop of Specimen 59 early in fatigue life (cycle 25) showing a low modulus segment (indicative of twin boundary motion) in tension but not in compression.

TABLE I

Threshold for Twin Boundary Motion

Specimen #	Twinning Shear Vector $\hat{g}$*	Twin Plane Normal $\hat{t}$*	Threshold (Kg/mm^2) Tension	Compression
53	63	61	2.341	2.341
58	37	59	4.422	5.019
62	68	39	2.088	2.864
75	58	44	2.955	3.689
76	64	52	1.118	1.730

* Measured from specimen axis.

for Specimen 53 where the thresholds are equal, the compressive threshold is always significantly greater than the tensile threshold.

The behavior of Specimen 70 does not seem to be explained by the above reasoning. Here the twinning shear vector was only 34° from the specimen axis while the twin plane normal was 72° from the axis. The stress-strain hysteresis loop (Figure 44) showed some twin boundary motion in both tension and compression with a significant strain remnant, but no well defined threshold for twinning deformation. Like Specimen 59, the measured diametral strain ratios agreed well with the predictions but the strain amplitudes were reduced. A possible explanation involves the specimen geometry. Here the twin plane is steeply inclined to the specimen axis such that one twin lamella extends from one shoulder through the midsection into the other shoulder. The large shoulder diameters relative to the midsection cause the shear stresses there to be ~1/3 that at the constriction. Thus, the twin boundaries are constrained in the shoulders by low stresses there. This pinning effect would be expected to "soften" the twinning threshold and reduce the strain amplitude because with steeply inclined twin lamella the tensile stress for breakaway is very position dependent and may never be reached well up on the shoulders. Hence, a twin segment in the midsection that has reached the threshold stress would be restrained by adjacent segment still pinned.

Specimens 58 and 76 had moderately good orientations and showed twin boundary motion in both tension and compression but deformed only to ~0.7 of their predicted strain amplitudes. A possible explanation for the case of Specimen 58 is found in the shape of the compressive part of the

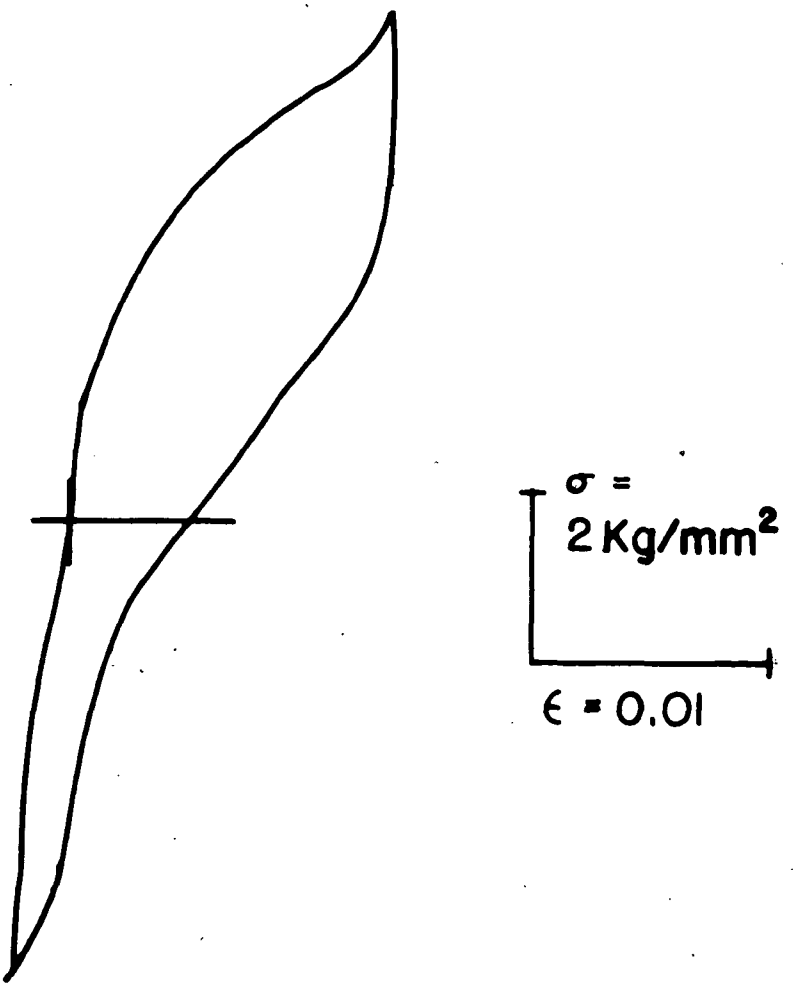

Figure 44. The hysteresis loop of Specimen 70 early in fatigue life (cycle 22) showing some lower modulus regions (indicative of twin boundary motion) in both tension and compression but no well defined threshold for twin boundary motion; see text.

hysteresis loop (Figure 17) which showed a much less abrupt transition to high modulus behavior accompanying the end of twin boundary motion than was observed in tension. Thus the more gradual transition in compression may indicate not an end to twin boundary motion, but rather an increase in the stress required to sustain this deformation mode. In favorably oriented specimens, the stress necessary for twin boundary motion does not change much as the boundaries move even though their movement is accompanied by a slight rotation.* In less favorable orientations, such as that of Specimen 58, however, the twin plane rotation moves the boundaries to sufficiently less favorable orientations so that additional stress is required for continued strain. Therefore, the failure to reach the anticipated strain in compression could be explained by the stress required for continued deformation rising above the programmed stress limit before total twin conversion is achieved.

B. The Effect of Cyclic Stresses on the Mechanical Properties

The initial cycles in specimens exhibiting twin boundary motion were characterized on increasing tension (or compression) by a "stress step", a high modulus region with an abrupt transition to low modulus behavior associated with the movement of twin boundaries (i.e., Figure 17). Although the high modulus segment suggests pinning of the twin boundaries, the absence of any yield drop indicating twin boundary breakaway militates against such a mechanism. The mechanical behavior can be understood, how-

---

* One of the consequences of the growth of one twin, as seen in Figure 11, is a small shear of the specimen which, due to gripping constraints, manifests itself as a rotation of the twin planes in the specimen mid-section in a manner analogous to slip plane rotation during slip.

ever, in terms of a time and temperature dependent restoring force and a Peierls-Nabarro stress.

β' AuCd has a lattice with a basis, and while the lattice twins instantly on the passage of a twin boundary,** some atoms in the structure are trapped in the "wrong" positions. In order for these atoms to become properly mirror positioned with respect to the displaced twin boundaries, time and temperature dependent shuffles must occur. If the stress which had moved the twin boundaries is removed before the shuffles can occur, the energy of the specimen can be reduced if the twin boundaries move back to their original positions thereby restoring atoms to their true mirror positions in the original twin. This is the origin of the twin boundary restoring force and the "rubberlike" behavior in β' AuCd according to Schmerling.[8] However, if the twin boundaries are held displaced for a temperature dependent time (~1 day at room temperature), the specimen's internal energy is reduced by the shuffling of these "wrong" atoms into their proper mirror positions with respect to the displaced twin boundaries; the restoring force to the original boundary positions will disappear, and the specimen will become "rubber-like" from the new twin configuration.

Since fatigue cycles are begun on well stabilized (rubber-like) specimens, it is proposed that part of the high modulus region and subsequent threshold is due to this volume restoring force since it is necessary

---

** A lattice twin is not a true crystallographic twin unless all the atoms are in their correct mirror related positions across the twin boundaries, and for this alloy, this is the case only in well stabilized specimens. The distinction is not made here in using the terms "twinning", "twin boundaries", etc..

to counteract this force in order to displace some atoms adjacent to a twin boundary into "wrong" positions (raising energy) and thus move the boundary into one twin. That the stress remains at, or slightly higher than, the threshold as boundary displacement increases away from its original position constitutes strong evidence that the restoring force on the boundary is associated with a volume stabilization process and not a pinning mechanism.

It is here proposed that the remainder of the initial high modulus region and all the high modulus segment on unloading (and thus the observed stress hysteresis) are due to a Peierls-Nabarro stress for twin boundary motion. Recently, Sumino[23] has proposed a theory of twin boundary motion in which the twin plane itself is considered to be a two dimensional dislocation that moves through the expansion of pillbox shaped kinks (Figure 45). The Burgers vector of the twinning dislocation is the twinning shear vector, and Sumino pointed out that since no bonds are broken in propagation of twinning dislocations, their energy of motion would be lower than that for slip dislocations. He applied Peierls-Nabarro calculations to his model and reported the calculated stress for twin boundary motion to be in reasonable agreement with that measured in several materials including β' AuCd.[24,25] This would account for high modulus segment on unloading and the stress hysteresis observed for all specimens.

All of the mechanical behavior of β' AuCd described here can now be accounted for by the effect of the time-temperature dependent volume restoring force (responsible for the rubber-like behavior) and the Peierls-Nabarro stress (producing the stress hysteresis) on the motion of twin boundaries: the shape of the stress-strain loops for well stabilized rubber-like

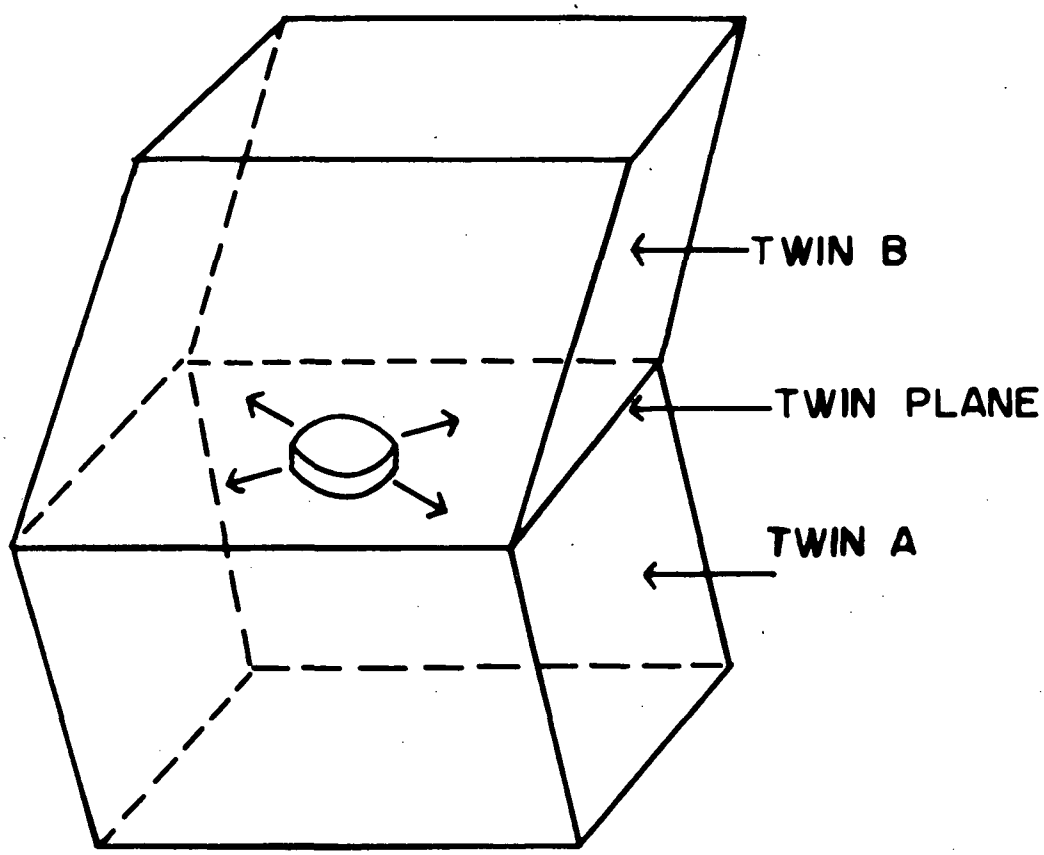

Figure 45. The movement of a twin plane by the expansion of a "pillbox" shaped kink. (From Sumino[23])

specimens (on which testing was begun), the transition to the stable loop as cycling proceeds, the development and disappearance of a stress step when cycling is suspended and then resumed, and the time and frequency dependence of the loop shape. While cyclic experiments were always begun on rubber-like specimens, it is more instructive to first consider a stable loop where the restoring force is nearly absent and the Peierls-Nabarro force is dominant. The reintroduction of rubber-like behavior can then be understood in terms of the stabilization process which occurs when cycling is stopped.

The near absence of the volume restoring force in specimens after many cycles can be explained by the continuous movement of a twin boundary back and forth past a given volume converting it from one twin orientation to the other. While the jumping process of shuffled "wrong" atoms to their proper positions is undoubtedly occurring, it does not contribute to the restoring force because the volume cannot be associated with a particular twin. This is especially true in the center of the twin boundary travel as shown in Figure 46 since a volume there spends half the time in each twin. It is less true near the limits of twin boundary motion where a volume is in one twin over most of the cycle thus allowing more stabilization (or properly positioned atoms) with respect to that twin than the other and hence a restoring force. Therefore, the stable loop shape is seen to be determined by the Peierls-Nabarro stress, σ_c, with an increasing restoring force component as the strain limits (and thus limits of twin boundary motion) are approached (Figure 47).

The observed temperature and frequency effects on the stable

Figure 46. Schematic representation of twin boundary motion showing twin boundary configurations at the midpoint of travel (top), at one extreme (middle) and at the other extreme (bottom). Note that position A is in twin 1 and position C is in twin 2 over most of the cycle while position B is equally shared by each twin.

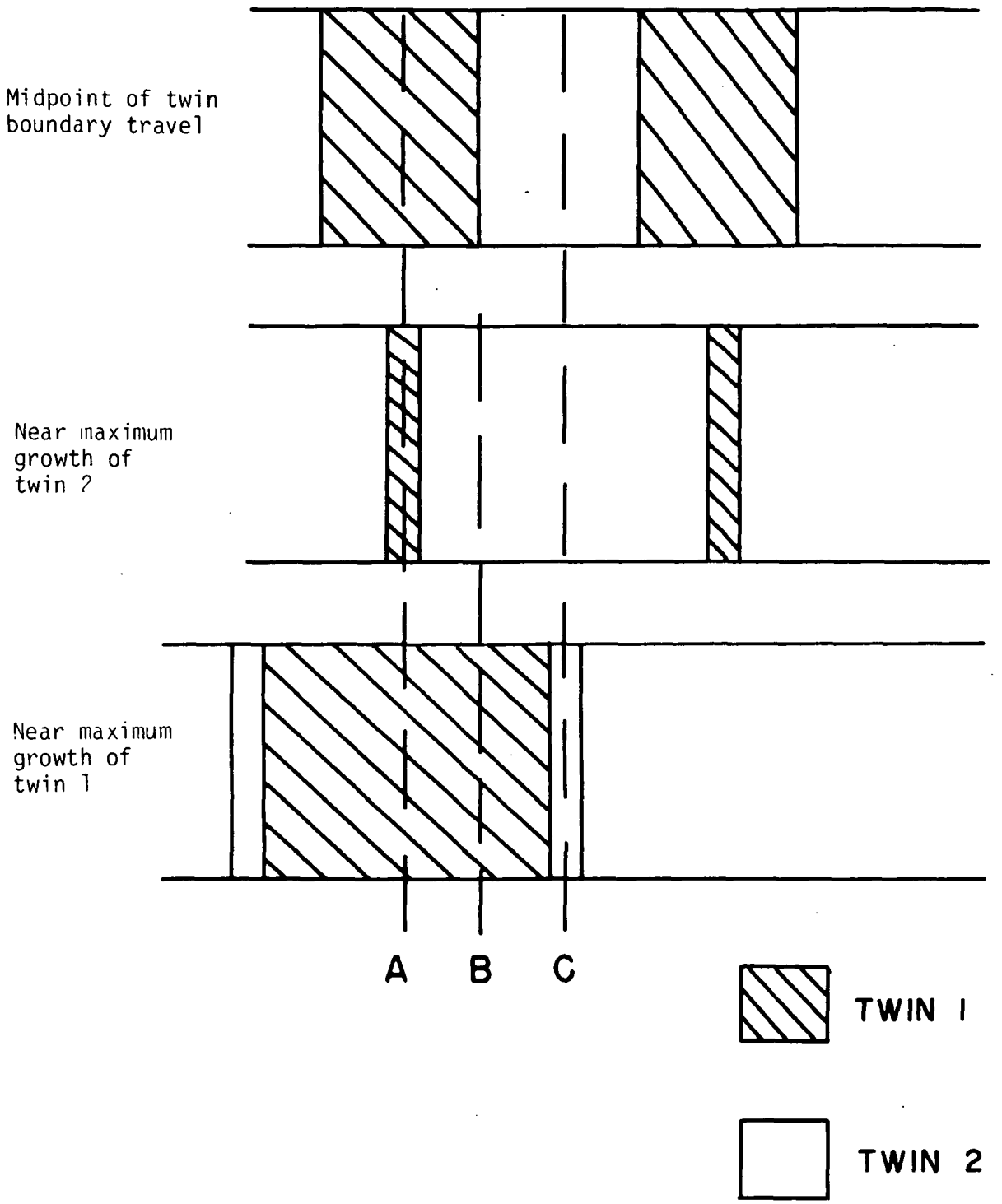
Midpoint of twin boundary travel
Near maximum growth of twin 2
Near maximum growth of twin 1
A
B
C
TWIN 1
TWIN 2

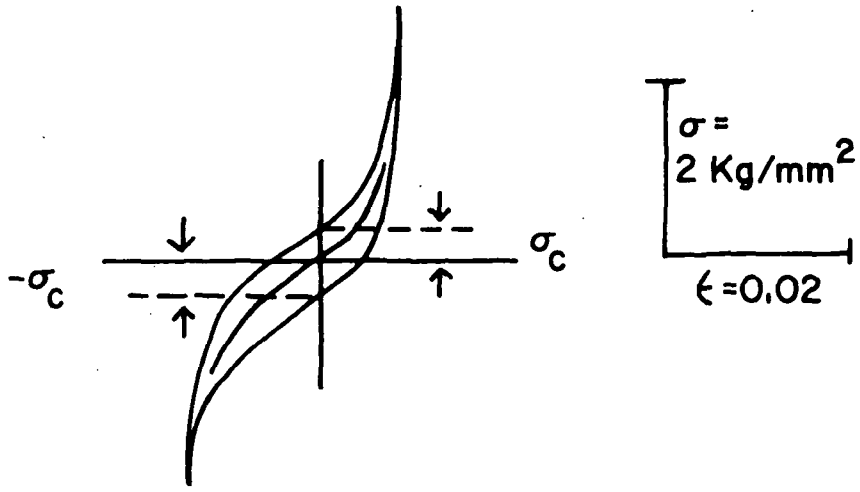

Figure 47. A stable loop of Specimen 76 showing the Peierls-Nabarro stresses at zero strain, $\pm\sigma_c$, responsible for the stress hysteresis and the stabilization restoring force drawn as a line in the center of the loop. Note that this force has no discontinuity in a stable loop.

loop shape (Figure 28) can now be understood in terms of continuing stabilization during cycling. If the frequency is sufficiently low and the temperature is sufficiently high, a given volume will have enough time to stabilize in one twin before the passage of the twin boundary. Thus this passage will be resisted by a restoring force in addition to the Peierls-Nabarro force always present, and the stress hysteresis will grow.

When cycling is interrupted and the twin boundaries are held stationary, every volume can henceforth be associated with a particular twin orientation, and the "wrong" atoms can shuffle to their correct positions unambiguously. Thus, there is a growing discontinuity in stabilization at the twin boundary positions with volumes on each side of the boundaries being stabilized in a different twin lattice. Hence, displacement of the boundaries into either twin causes an appropriately directed restoring force and thus a stress step because the restoring force is a volume force and does not vary linearly with displacement (Figure 48). A stress step can be put anywhere in a stable loop simply by stopping twin boundary motion (by stopping the machine) and thereby removing the ambiguity in stabilization caused by twin boundary motion. Ultimately the volumes in each twin will be completely stabilized, and, except for the large discontinuity at the holding point, the restoring force will remain constant as shown in Figure 48. The Peierls-Nabarro force will continue to give a stress hysteresis of $2\ \sigma_c$, and the stable loop will have been converted to a shape like that of a well stabilized specimen at the start of testing (Figure 17). When cycling is resumed, the ambiguity of twin orientation is reintroduced and the stable loop is recreated.

Figure 48. The synthesis of a stable loop (above) and a loop in a well stabilized specimen (below). (a) shows the loops expected from the restoring force alone. The monotonic restoring force in the stable loop is schematically represented as linear. (b) shows the addition of stress hysteresis due to the Peierls-Nabarro force, and (c) shows a stable loop (above) of Specimen 56 and a loop after a 400 minute room temperature hold at zero stress (below).

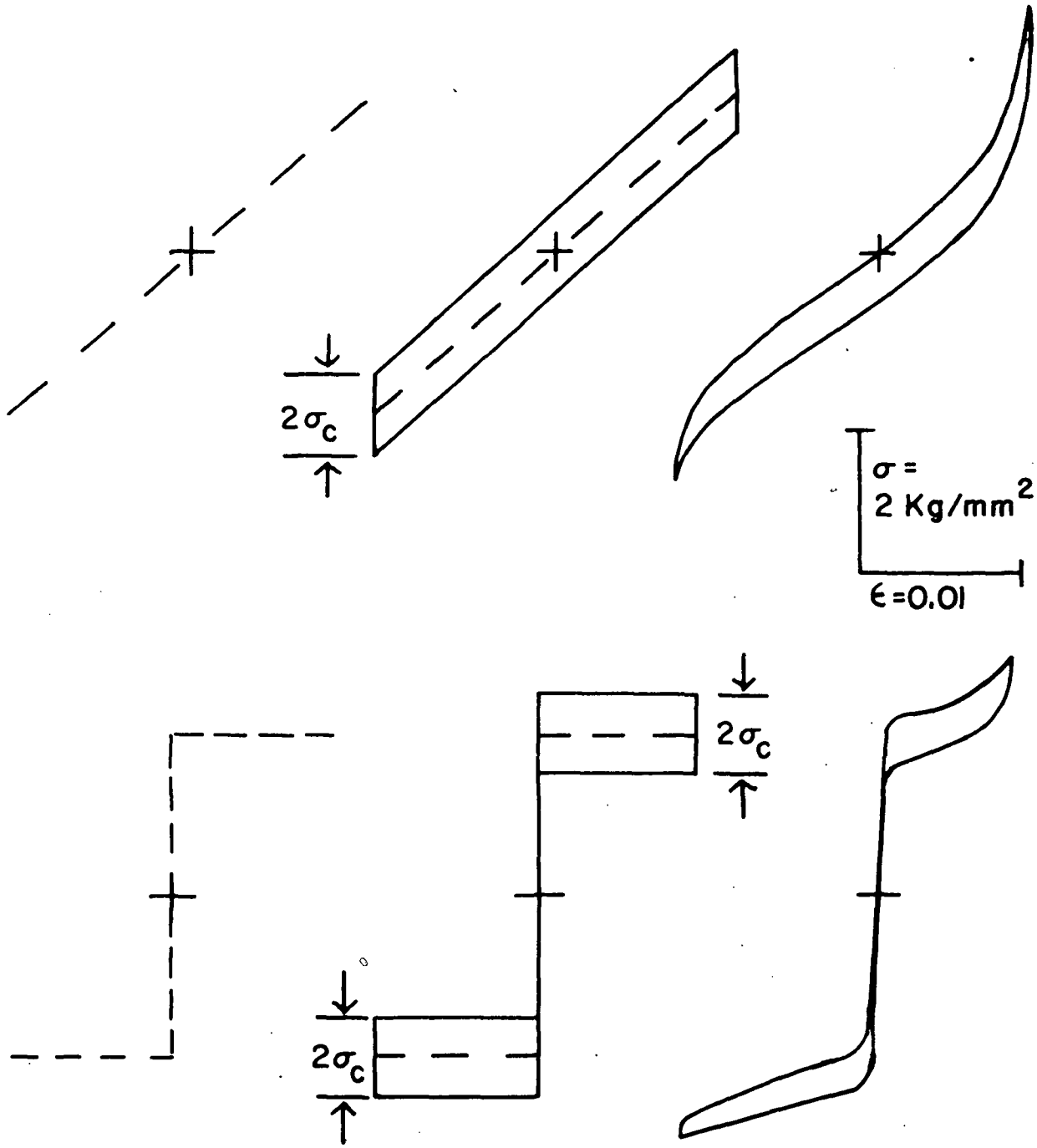

(a) RESTORING FORCE

(b) RESTORING FORCE AND PEIERLS-NABARRO STRESS

(c) SPECIMEN 56

C. Fatigue Properties

The log strain vs log cycles to failure data plotted in Figure 37 illustrate the very orientation dependent broad range of behavior exhibited by AuCd specimens. Thus Specimen 68 was tested 1,005,000 cycles at a strain amplitude of approximately 0.07 without failure while Specimen 61 failed in 32 cycles at a strain of approximately 0.05. The difference in strain amplitude for these two specimens was primarily a function of specimen orientation, but the spread of fatigue lives was principally influenced by the stress level required to achieve the strain in the particular specimen as illustrated, for example, by the stable hysteresis loop of Specimen 76 (Figure 47). In this case, the low modulus region representing twin boundary motion ends abruptly in both tension and compression. Hence, raising the load limits (in load control) would greatly raise the stresses without significantly raising the strain. Likewise, raising the strain limits (in strain control) would also cause greatly increased stresses. Since no more deformation by the motion of twin boundaries is possible in either mode of control, these increases can only raise the plastic component of the deformation and thus shorten fatigue life without significantly increasing the strain amplitude. Specimen 61 failed in 32 cycles because it was tested under $\pm$ 19.0 Kg/mm^2 longitudinal stress while Specimen 68 had not failed at over 1,005,000 cycles, not because it deformed approximately 0.07 by twin boundary motion, but because this large strain could be obtained with only $\pm$ 2.8 Kg/mm^2. Had Specimen 68 been tested at $\pm$ 19.0 Kg/mm^2 it would have shown negligible additional strain but a much shorter life.

The influence of stress on fatigue life is shown in Figure 38 as log stress vs log cycles to failure. These data appear to fit the linear relation proposed by Basquin[26] which corresponds to the equation

$$\sigma_a = \sigma_f' (2N_f)^b$$

where σ_a is the half life stress limit, σ_f' is the fatigue strength coefficient, $2N_f$ is the number of reversals to failure, and b is the fatigue strength exponent.[19] The best fit line through the fatigue data gives values for b of -0.1875 and σ_f' of 49 Kg/mm^2. It is interesting to note that σ_f' may be approximated by the true fracture strength which has been measured at 44 Kg/mm^2 and 38 Kg/mm^2 on two tensile specimens (Section II, C, 1). Figure 38 indicates that the stress fatigue resistance of AuCd is low compared with most metals.

The fatigue data indicate that, to a good approximation, fatigue lives are determined principally by the peak stresses regardless of the type of specimen (single region, multiple region or polycrystalline), orientation, or observed strain amplitude. This implies that while fatigue is essentially due to the relatively isotropic {100} <100> plastic deformation,[22] the observed strain amplitude is due (sometimes almost entirely) to the highly anisotropic deformation by twin boundary motion which apparently affects the actual fatigue life very little. Thus, the long fatigue lives at high strain amplitudes are possible because the large cyclic strains can be obtained at stress levels far below those which cause measurable fatigue damage by conventional means (even) in this material. In theory, the scatter in the strain fatigue data (Figure 36) could be reduced by subtracting the strain due to twin boundary motion. However, it is difficult to separate this strain from the plastic and elastic strain in the hysteresis loop because

the former is generally small and the latter is small and highly anisotropic.

The "hardening effect" (Section IV, C) may be qualitatively understood in terms of Sumino's model for twin boundary motion.[23] Since the pill-box shaped kinks by which the twin boundaries move always propagate outwards towards the specimen's surface, any fatigue generated lattice defects (indicated by the marked degeneration of Laue spots in x-ray photographs of tested specimens) would be swept towards the surface. Since twin lamella are thousands of times longer than they are wide,* it is likely that most defects would diffuse out of the paths of the kinks and into areas not swept by twin boundary motion long before they reach the surface. These defects, as they accumulate, would reduce the amplitude of the twin boundary motion and thus account for the slight reduction in strain amplitude often observed in load control testing. Furthermore, this would explain the hardening effect on suspension of testing since these defects could then diffuse into the twin lamellae and raise the stress for subsequent twin boundary motion. The absence of hardening in specimens stored at -190°C (Figure 39) is understood since diffusion is drastically reduced at low temperature.

---

* While the specimen is several mm wide, the twin lamellae are observed optically to be approximately 1 micron thick.

VI. SUMMARY AND CONCLUSIONS

β' AuCd is indeed a remarkable material deforming up to approximately 0.076 ferroanelastically by the reversible motion of twin boundaries (either present in the specimen or nucleated in response to stress) at load levels typically far below that for the measurable plastic deformations apparently necessary for fatigue in this alloy. Thus, exceptional strain fatigue behavior was frequently observed with fatigue lives from 10^5 to 10^6 cycles at strain amplitudes ($\Delta\varepsilon$) above 0.05 as compared with lives below 10^3 cycles in normal metals at these strains. However, the stress fatigue resistance was low compared with most metals. Ferroanelastic deformation was found to be highly anisotropic and prevented by grain boundaries thereby requiring test specimens to be grown as single crystals in the β parent phase. The mechanical properties and maximum ferroanelastic strain in all directions were predictable from a knowledge only of the orientation of the twin system in specimens with a single set of twins. The frequency and temperature dependence of the stress-strain hysteresis loop in cyclic deformation and the formation a "stress step" when cycling stopped were successfully accounted for by a synthesis of a volume stabilization process involving atoms displaced to metastable positions by twin boundary motion (proposed earlier to explain the "ferroelastic" or rubber-like effect in AuCd),[11] a Peierls-Nabarro model for twin boundary motion,[22] and new concepts of a stabilization discontinuity and fractional stabilization. Fatigue lives were shown to follow Basquin's stress relation regardless of orientation, type of specimen (single region, multiple region or polycrystalline), or principle deformation mode (transformation twin boundary motion, mechanical twinning or plastic deformation). This strongly suggests that relatively

isotropic plastic deformation (as compared to twin boundary motion) was mainly responsible for fatigue. Failure showed brittle characteristics typical of ordered alloys.[27]

It has been demonstrated that AuCd has exceptional high strain fatigue resistance and would be useful particularly in applications that exploit its high electrical conductivity such as pacemaker electrodes and relay armature connections. In addition, the examination of the cyclic mechanical properties of this alloy has proved to be a unique and fruitful approach to understanding ferroelastic phenomena and indicates the potential value of similar work in TiNi and the other "memory" alloys.

LIST OF REFERENCES

1. W. J. Beuhler and F. E. Wang, Ocean Eng., 1, 105 (1968).
2. W. A. Rachinger, J. Aust. Inst. of Metals, 5, 114 (1960).
3. N. W. Burkart and T. A. Read, Trans. AIME, 197, 1516 (1953).
4. Z. S. Basinski and J. W. Christain, ACTA Met, 2, 101 (1954).
5. C. M. Wayman, Scripta Met., 5, 489 (1971).
6. H. Pops, Met. Trans., 1, 251 (1970).
7. J. D. Eisenwasser and L. C. Brown, Met. Trans., 3, 1359 (1972).
8. M. S. Schmerling, Ph.D. Thesis, University of Illinois, Urbana, (1972).
9. D. S. Lieberman, Phase Transformations, ASM, p. 1, Metals Park, Ohio (1970).
10. D. S. Lieberman, M. S. Wechsler and T. A. Read, J. Appl. Phys., 26, 473 (1955).
11. D. S. Lieberman, T. A. Read and M. S. Wechsler, J. Appl. Phys., 28, 532 (1957).
12. H. K. Birnbaum and T. A. Read, Trans. AIME, 218, 662 (1960).
13. J. W. Semmel, Jr., M. S. Thesis, Columbia University (1952).
14. A. Bystrom and K. E. Almin, Acta Chem. Scand., 1, 76 (1947).
15. L. C. Chang and T. A. Read, Trans. AIME, 191, 47 (1951).
16. Handbook of Chemistry and Physics, 48th ed., R. C. Weast, ed., Cleveland, Chemical Rubber Company, p. D-143 (1967).
17. J. W. Christain, The Theory of Transformations in Metals and Alloys, Oxford, Permagon Press (1965).
18. C. E. Feltner and M. R. Mitchell, Manual on Low Cycle Fatigue Testing, ASTM Special Technical Publication No. 465, pp. 27-66 (1969).
19. D. T. Raske and J. Morrow, Manual on Low Cycle Fatigue Testing, ASTM Special Technical Publication No. 465, pp. 1-25 (1969).
20. H. K. Birnbaum and T. A. Read, Trans. AIME, 218, 381 (1960).
21. R. W. Landgraf, Cyclic Deformation and Fatigue Behavior of Hardened Steels, T.& A.M. Report No. 320, University of Illinois, Urbana, p. 73 (1968).

22. H. K. Birnbaum and W. Class, Acta Met., 6, 609 (1958).

23. K. Sumino, Acta Met., 14, 1607 (1966).

24. K. Sumino, Phys. Stat. Sol. 33, 327 (1969).

25. T. Aoyagi and K. Sumino, Phys. Stat. Sol. 33, 317 (1969).

26. O. H. Basquin, Proc., ASTM, ASTEA 10, 625 (1910).

27. Ordered Alloys, B. H. Kear, C. T. Sims, N. S. Stoloff and J. H. Westbrook, eds., Baton Rouge, Claitor's Publishing Division pp. 259-331 (1970).

APPENDIX A

WIRE FABRICATION

Wires 0.5 mm in diameter and over 40 cm long were cast using the following technique. The apparatus shown in Figure 49 was constructed from quartz tubing. An AuCd ingot was placed in the apparatus as shown, and was passed through the system thus purging the air. The system was sealed at the constriction (A) at 1 atmosphere argon, placed in a furnace (~700°C), and tilted to allow the molten ingot to flow up against the junction with the capillary tube. The argon pressure was increased approximately 10 psi thus forcing the ingot into the capillary tube. The pressure reservoir formed by sealing the constriction prevented passage of the molten ingot completely through the capillary tube. The apparatus was driven out of the furnace at approximately 10 inches per hour to achieve large grain size, and the apparatus was broken open to retrieve the cast wire.

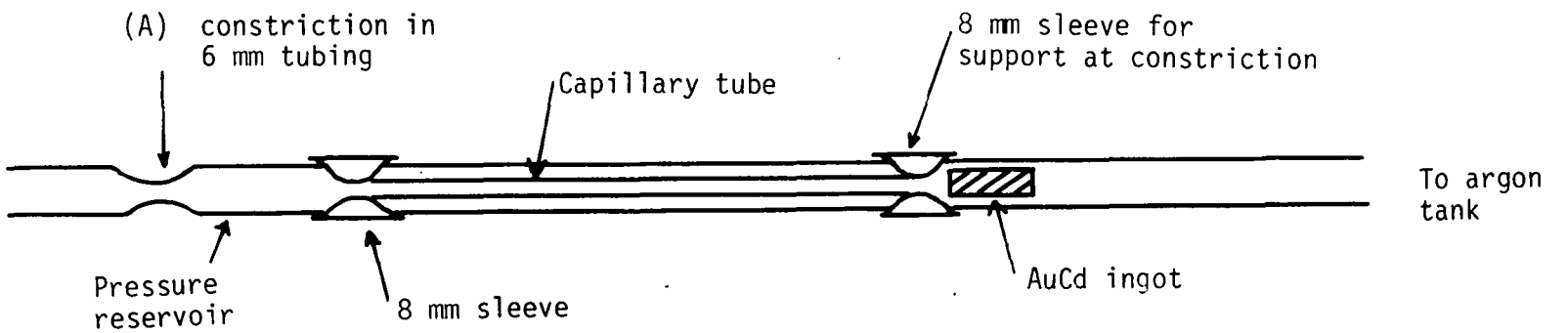

Figure 49. The wire casting apparatus made entirely of quartz tubing showing a capillary tube joined to a 6 mm tube. After flushing the system with argon, it is sealed at (A) at 1 atmosphere pressure. The apparatus is placed in a furnace so the molten ingot flows against the capillary tube junction, and the ingot is cast by raising the argon pressure.

APPENDIX B

DATA SUMMARY

1. Load Control Testing

Specimen #	Type[a]	Comp. % Cd[b]	Stress (Kg/mm^2)	Strain Half Life	Strain Max.	Strain Min.	Cycles to Failure
53	S	47.495	6.877	0.072	0.072	0.072	13,145
55	S	47.493	7.517	0.042	0.045	0.042	55,625
56	M	47.494	3.512	0.034	0.038	0.027	556,245
57	S	47.490	5.956	0.043	0.044	0.043	8,585
58	S	47.484	6.598	0.021	0.030	0.021	136,710
59	S	47.499	3.192	0.009	0.014	0.005[c]	15,000[d]
60	M	47.487	17.739	0.026	0.026	0.024	1,150
61	S	47.493	19.552	0.053	0.053	0.053	32
67	S	47.493	18.369	0.022	0.030	0.019	65,690
68	O	47.492	2.329	0.064	0.074	0.063	1,005,000[d]
69	M	47.496	5.935	0.036	0.036	0.036	128[d]
70	S	47.499	5.577	0.013	0.013	0.012	441,250
71	M	47.489	5.886	0.043	0.044	0.043	6,685
72	S	47.478	2.918	0.053	0.058	0.053	111,700
73	S	47.480	11.440	0.032	0.034	0.032	341
74	S	47.493	12.110	0.064	0.064	0.064	60[d]
75	S	47.389[f]	5.540	0.053	0.057	0.050	10,490
76	S	47.489	2.792	0.023	0.030	0.023	136,000
81	S	47.496	9.322	0.027	0.027	0.027	10,835

a) S is single region, M is multiple region and O is orthorhombic single crystal.
b) Assuming all weight loss is cadmium.
c) Testing interrupted and hardening effect observed.
d) No failure.
e) Stressed in tension only.
f) Some loss of ingot during homogenization.

2. Stroke Control Testing

Specimen #	Type	Comp. % Cd	Strain	Stress (Kg/mm^2) Half Life	Max.	Min.	Cycles to Failure
62	S	47.484	0.048	3.299	4.124	3.299	400,000
63	P[a]	47.485	0.013	13.689	13.689	13.689	2,205
64	P	47.480	0.024	12.369	12.369	12.369	1,240
65	P	47.487	0.008	8.550	8.550	7.988	40.070
66	P	47.481	0.038	20.828	20.828	20.828	70

a) Polycrystal

APPENDIX C

ESTIMATION OF TORSION STRAIN AMPLITUDE

The following is an approximation to true strain at the surface of torsion specimens. It assumes that a) Hooke's law is obeyed, b) the specimen is isotropic with respect to torsion stress* and c) plane sections normal to the specimen axis remain plane during deformation. The assumption of Hooke's law is justified by the torque vs total twist angle data (Figure 50) which, unlike most tension-compression data, are relatively linear owing to the isotropic nature of torsion strain.

If a cylinder of thickness x and radius R is strained in torsion (Figure 51), the shear stress, $\tau(r)$, at any radius $r > R$ may be expressed as

$$\tau(r) = G\gamma(r) \tag{1}$$

where

G = shear modulus

γ = shear strain

If the twist angle per unit length, $\frac{d\theta}{dx}$ in a cylindrical section does not vary with r, then

$$\gamma(r) = r \frac{d\theta}{dx}$$

and Eq. 1 becomes

$$\tau(r) = Gr \frac{d\theta}{dx} \tag{2}$$

---

* This is more true for torsion than for longitudinal stress and is necessary to simplify the calculation.

Figure 50. The torque data vs total twist for a typical torsion specimen showing approximate linearity (no stress steps or large changes in modulus) justifying the use of Hooke's law to estimate strain.

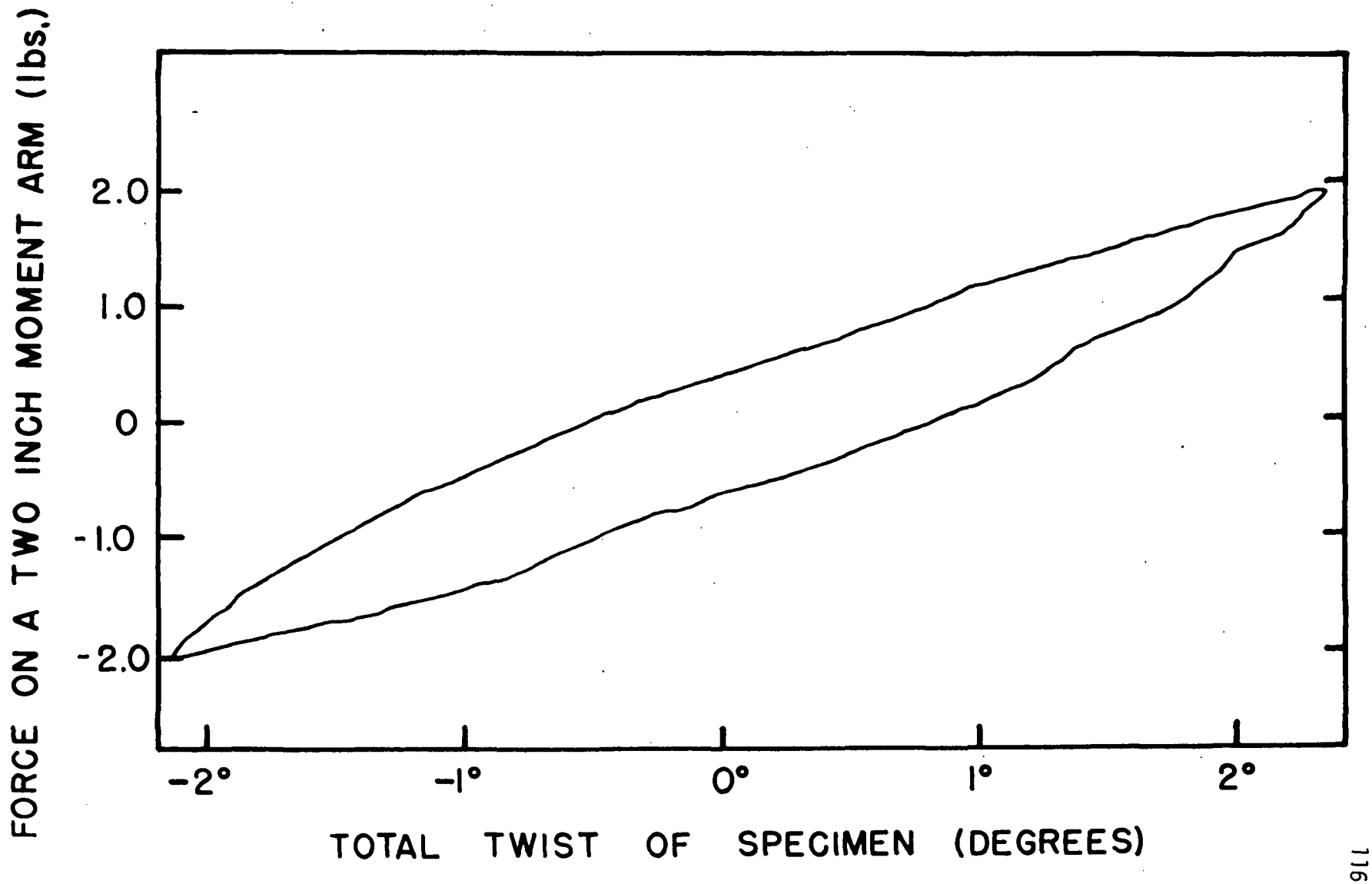
FORCE ON A TWO INCH MOMENT ARM (lbs.)
2.0
1.0
0
-1.0
-2.0
-2°
-1°
0°
1°
2°
TOTAL TWIST OF SPECIMEN (DEGREES)

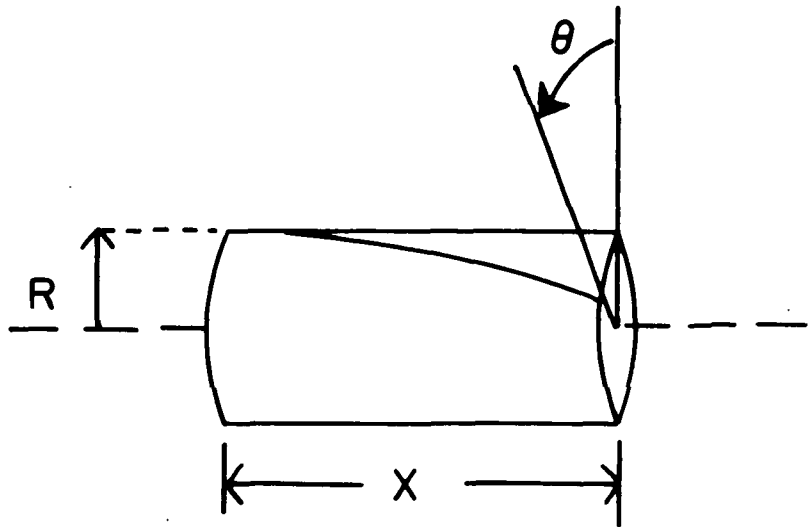

Figure 51. The twist of a cylinder of radius R and length x showing linear displacement of a fiducial mark with increasing x.

The torque on the cylinder, M, is

$$M = \int_0^R (2\pi r)(\tau(r))(r)\, dr$$

$$= \int_0^R (2\pi r)(Gr \frac{d\theta}{dx})\, r\, dr$$

$$M = \frac{\pi}{2} G \frac{d\theta}{dx} R^4 \qquad (3)$$

The torsion specimen (Figure 3b) can be considered to be composed of a number of short cylinders or discs of thickness dx whose radius R(x) can be described by the polynomial

$$R(x) = Ax^4 + Bx^2 + C \qquad (4)$$

whose coefficients are determined by the boundary conditions:

$R(0)$ = minimum specimen radius

$R(\pm 1/4")$ = shoulder radius

$\frac{dR(\pm 1/4")}{dx} = 0$

Therefore, Eq. 3 becomes

$$M = \frac{\pi}{2} G \frac{d\theta}{dx} [R(x)]^4 \qquad (5)$$

which may be rearranged by separating variables and integrating to obtain:

$$\frac{2M}{\pi G[(x)]^4}\, dx = d\theta$$

or

$$\frac{2M}{\pi G}\int_{-1/4"}^{+1/4"} \frac{dx}{[R(x)]^4} = \theta \tag{6}$$

where θ is the total twist angle of the specimen. The integral is approximately 1.1×10^4 for a typical specimen and was calculated by iteration on a Wang model 700A calculator. Since M and θ are easily measurable, Eq. 6 can be solved for G and substituted into Eq. 3 to obtain

$$M = \frac{\pi}{2}\,\frac{2M}{\pi\theta}\int_{-1/4"}^{1/4"} \frac{dx}{[R(x)]^4}\,\frac{d\theta}{dx}\,R^4 \tag{7}$$

solving Eq. 7 for $\frac{d\theta}{dx}$

$$\frac{d\theta}{dx} = \frac{\theta}{R^4\int_{-1/4"}^{1/4"} \frac{dx}{[R(x)]^4}}$$

Since $\gamma = R\,\frac{d\theta}{dx}$, the maximum shear strain at the specimen surface is found at a minimum radius, R_{min} where

$$\gamma_{max} = R_{min}\,\frac{d\theta}{dx} = \frac{\theta}{R_{min}^3\int_{-1/4"}^{1/4"} \frac{dx}{[R(x)]^4}} \tag{8}$$

APPENDIX D

THE STRAIN PREDICTION ALGORITHM

The strains caused by complete twin conversion in β' AuCd can be calculated in two essentially equivalent ways. The first involves the Bain strains during the β→β' transition,[8] and while the calculation is direct, its justification is somewhat cumbersome and it will not be considered here. The second parallels the treatment of Christain and Basinski[4,8] in which the twinning shear vector is added directly to a unit vector in the direction of the length change to be calculated. Figure 4 shows a conventional twinning diagram with the twinning shear direction $\hat{g}$, the twin plane normal vector $\hat{t}$ and a unit vector $\hat{V} = \cos\ \alpha\hat{i} + \cos\ \beta\hat{j} + \cos\ \gamma\hat{k}$ expressed in the orthorhombic system; the length change of $\hat{V}$ is to be calculated. The twinning operation displaces $\hat{V}$ by distance C in the shear direction $\hat{g}$ or

$$\vec{V}' = \hat{V} + C\hat{g} \tag{1}$$

where C is proportional to the distance of $\hat{V}$ above the twin plane $(\hat{V}\cdot\hat{t})$. Since C = 2 tan α at a unit distance above the twin plane, Eq. 1 becomes

$$\vec{V}' = \hat{V} + 2\ \tan\alpha(\hat{V}\cdot\hat{t})\ \hat{g} \tag{2}$$

Thus the length change of $\hat{V}$ may be calculated by subtracting 1 from $|\vec{V}'|$ or

$$\Delta L = [1 + 4\ \tan\alpha\ (\hat{V}\cdot\hat{t})\ (\hat{V}\cdot\hat{g}) + 4\ \tan^2\alpha(\hat{V}\cdot\hat{t})^2]^{1/2} - 1 \tag{3}$$

where V has been rotated $\phi = \frac{\hat{V} \cdot \vec{V}'}{|\vec{V}'|}$ which has a maximum value of 2α or 8.9 degrees.[11]

APPENDIX E

ESTIMATION OF LONGITUDINAL STRAIN WHEN THERE IS NO TWINNING DEFORMATION

The strain amplitude at the midsection in specimens which do not deform by twin boundary motion may be estimated by assuming Hooke's law is obeyed and considering the machine to be hard and the specimen to be composed of a number of discs or radius $R(x) = Ax^4 + Bx^3 + C$ as in Appendix C. For each disc

$$\sigma = \frac{\text{Force}}{\text{Area}} = \frac{F}{\pi[R(x)]^2} = E\,\varepsilon(x) \tag{1}$$

where

σ = tensile stress

E = the effective modulus

$\varepsilon(x)$ = tensile strain

Therefore

$$\varepsilon(x) = \frac{F}{\pi E[R(x)]^2} \tag{2}$$

The total elongation of a cylinder of thickness dx is $\varepsilon(x)\,dx$. Therefore the total length change of the specimen, the stroke, S, is

$$S = \int_{x=-1/4"}^{x=+1/4"} \varepsilon(x)\,dx = \frac{F}{\pi E}\int_{x=-1/4"}^{x=+1/4"} \frac{dx}{[R(x)]^2} \tag{3}$$

$$\therefore \quad E = \frac{F}{\pi S}\int_{x=-1/4"}^{x=+1/4"} \frac{dx}{[R(x)]^2} \tag{4}$$

Since the maximum strain is found at the minimum radius, using $R(x) = R_{min}$ in Eq. 2 and substituting Eq. 4 for E

$$\varepsilon_{max} = \frac{S}{(R_{min})^2} \left[\int_{x=-1/4"}^{x=+1/4"} \frac{dx}{[R(x)]^2} \right]^{-1} \tag{5}$$

Since $\int_{x=-1/4"}^{x=+1/4"} \frac{dx}{[R(x)]^2} \simeq 80$ for a typical specimen and $R_{min} \simeq .063$, Eq. 5

$$\varepsilon_{max} \simeq 3S \tag{6}$$

APPENDIX F

CALCULATION OF THE FRACTION OF THE APPLIED LONGITUDINAL STRESS RESOLVED FOR TWINNING

The geometric factor for cylindrical rods in resolving the applied stress as shear on the twin plane in the twinning direction is $\cos\theta\cos\phi$ where θ and ϕ are the angles the twin plane normal and twinning direction make with the cylinder axis. In considering the geometric factor for hourglass specimens, the ϕ dependence is unchanged since the component of the stress in the direction of twinning shear is unchanged. However, the θ dependence represents a reciprocal area factor which is significantly changed in the hourglass shape. The geometric factor here is

$$g_\theta = \frac{A_{min}}{A_\theta} \qquad (1)$$

where

A_{min} is the minimum cross sectional area at the specimen midsection

A_θ is the area of a plane through the midsection whose plane normal makes an angle θ with the specimen axis

To calculate A_θ, consider the specimen to be composed of discs of thickness dx. As with Appendices C and E, the radius of the discs can be expressed by the polynomial $R(x) = Ax^4 + Bx^2 + C$. Figure 52 shows the specimen and the plane A_θ which intersects each disc as a rectangle whose length, ℓ, is a chord of the disc and whose width is $\frac{dx}{\cos(90-\theta)} = \frac{dx}{\sin\theta}$. Thus

$$A_{disc} = \frac{dx}{\sin\theta}\,\ell \qquad (2)$$

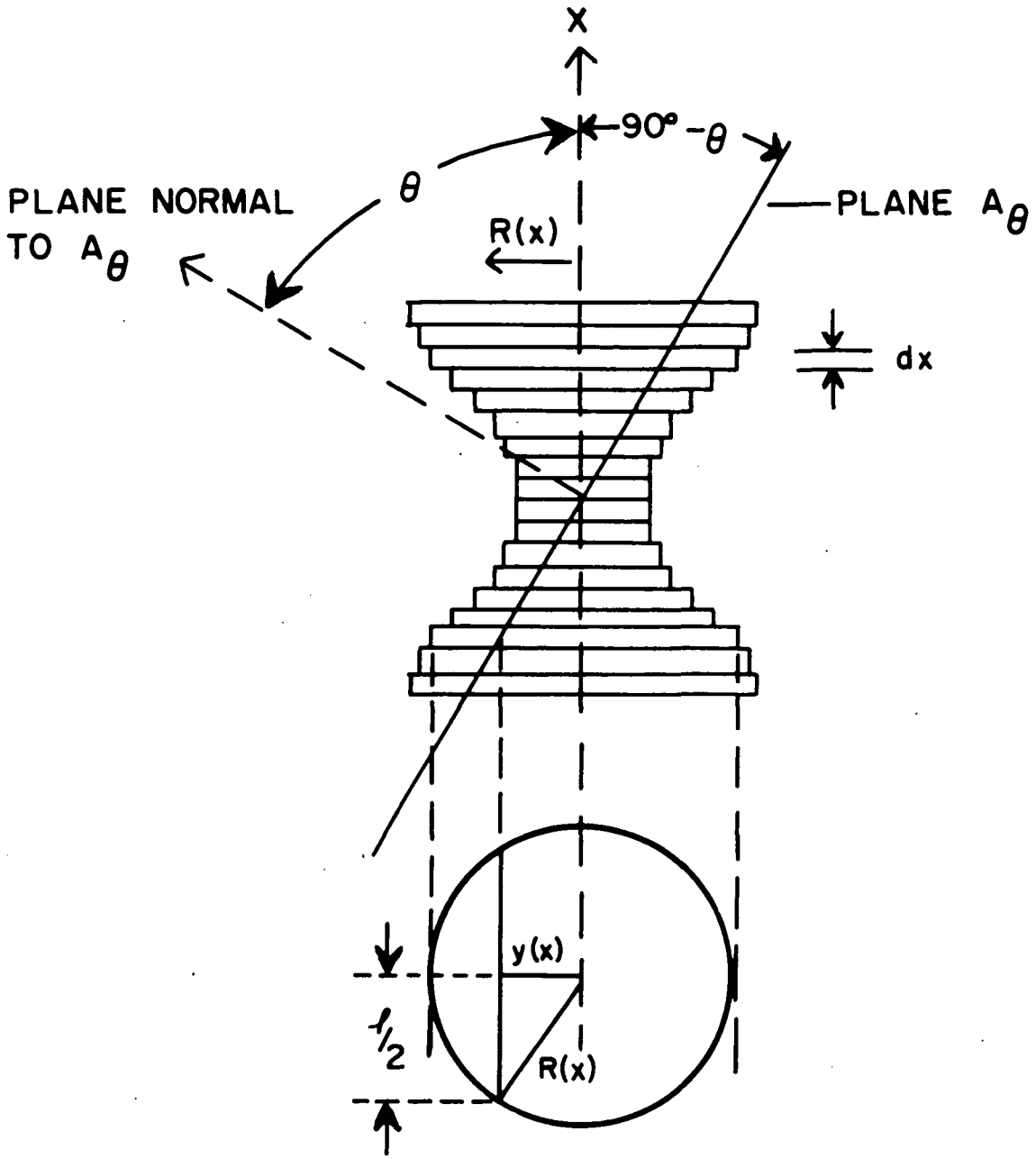

Figure 52. The determination of the area of plane A_θ. The specimen is divided into discs of thickness dx, and the area of the rectangle of intersection of the A_θ plane with each disc, $(dx/\sin\theta)(\ell)$, is summed.

From Figure 52

$$\ell = 2\left[[R(x)]^2 - [Y(x)]^2\right]^{1/2} \tag{3}$$

where

$$Y(x) = x \tan (90-\theta)$$
$$= x \cot \theta \tag{4}$$

Substituting Eqs. 3 and 4 in Eq. 2

$$A_{disc} = \frac{2dx}{\sin \theta}\left[[R(x)]^2 - [x \cot \theta]^2\right]^{1/2} \tag{5}$$

and the total area of the plane, A_θ, is obtained by integrating Eq. 5. This was done by iteration on a Wang 700A calculator, and Eq. 1 was used to compile a table of geometric factors at 1 degree intervals between $\theta = 0$ and $\theta = 90$ degrees.

VITA

Robert Stephen Karz was born [redacted]; in [redacted]. He completed his primary and secondary education in the suburban Brighton School District and was graduated from Brighton High School in June, 1963. He entered the Massachusetts Institute of Technology in September, 1963, and received his B.S. degree in Physics in June, 1967. He entered the Graduate College of the University of Illinois in June, 1967, and received his M.S. degree in June, 1968. He held the position of Research Assistant in the Department of Metallurgy and Mining Engineering from June, 1967 to August, 1967, and from June, 1968 to June, 1972.

He is a member of the American Society for Metals and the Metallurgical Society of AIME, and is an associate member of Sigma Xi.